Title
Photodissociation and Hypergolic Reaction Dynamics of Ionic Liquids

Author
Koh, Christine Jungmin

Publication Date
2012

Peer reviewed|Thesis/dissertation

Photodissociation and Hypergolic Reaction Dynamics of Ionic Liquids

By

Christine Jungmin Koh

A dissertation submitted in partial satisfaction of the

requirements for the degree of

Doctor of Philosophy

In

Chemistry

in the

Graduate Division

of the

University of California, Berkeley

Committee in charge:

Professor Stephen R. Leone, Chair

Professor Daniel M. Neumark

Professor David Attwood

Fall 2012

Photodissociation and Hypergolic Reaction Dynamics of Ionic Liquids

Christine Jungmin Koh

Abstract

Photodissociation and Hypergolic Reaction Dynamics of Ionic Liquids

By

Christine Jungmin Koh

Doctor of Philosophy in Chemistry

University of California, Berkeley

Professor Stephen R. Leone, Chair

Ionic liquids (ILs) are room temperature molten salts with unique properties and broad range of applications. The properties are tunable based on the cation−anion (C^+-A^-) combination. Studying the ion pairs provides understanding of the interaction between the isolated cation and anion, which primarily determines the electronic and nuclear structure.

New velocity map imaging experiments were initiated to study the dissociative pathways upon photoexcitation of isolated ion pairs. Dissociative ionization and ion pair dissociation pathways initiated by 54 nm light of an IL, 1-ethy-3-methylimidazolium ($[Emim]^+$) bis(trifluoromethyl-sulfonyl)imide ($[Tf_2N]^-$), are revealed. Furthermore, the ultrafast excited dynamics of an IL, $[Emim]^+[Br]^-$, has been studied using time-resolved photoion spectroscopy. Momentary depletion of the intact cation and rise of the alkyl-loss fragments are observed, suggesting a possibility for a short-lived electronically or internally excited state that promotes the formation of alkyl-loss fragments upon probe excitation.

The volatilization process of thermally stable and unstable ionic liquids is studied using tunable vacuum ultraviolet light (VUV). Heats of vaporization for imidazolium-based ionic liquids are measured and the ionization threshold for the neutral ion pair is directly measured for the first time. The thermal decomposition mechanism for $[Emim]^+[Br]^-$ is explored to understand the volatilization process better, showing that alkyl abstraction upon heating occurs via an S_N2 type mechanism.

Moreover, an IL hypergolic reaction mechanism is studied using an aerosol flow tube method combined with tunable VUV light to understand the reaction chemistry of a potentially less corrosive and toxic rocket fuel system. Isolated ion pairs are monitored from IL aerosols with the advantage of less photofragmentation. Observation of early stage reaction intermediates, cyanamide, N_2O, and CO_2 from a hypergolic IL reaction with nitric acid reveals the existence of a nitro-substituted intermediate.

Dedicated to my beloved family,

Father, Sun-ho Koh 고선호

Mother, Kyung-hee Moon 문경희

Brother, Brian Youngwook Koh 고영욱

And husband-to-be, Bogdan Negru 복단

Contents

Acknowledgements

It would not have been possible to finish graduate school with a fond memory if it was not the help and support from the people around me, to only some of whom it is possible to give particular mention here.

Above all, my deepest gratitude goes first to my advisor, Professor Steve Leone, who guided me through the tough graduate education and who shared the excitement of new results. The work presented in this doctoral thesis would not have been possible without the support, patience, and excellent mentorship of Steve. His expertise in chemical dynamics and abundant research experience not only improved my research skills, but also inspired me to follow in his footsteps. I feel very lucky and grateful to have him as my advisor as I learned how to be a good scientist and to prepare for future challenges. I thank my committee members, Professor Dan Neumark, and Professor David Attwood, for their advice and support during my graduate study as well. I will miss the two sisters, Lucky and Seven.

I have been fortunate to collaborate with Steve Chambreau and Gammy Vaghjiani for five+ years. I would like to thank them for the wonderful and fruitful collaboration. I am eternally thankful to Steve C. for all discussions and limitless helps during and after the experiments. It has been a great pleasure working with Steve C. and I am confident that he will bring continued success to the project. I am also thankful to Gammy for the guidance and suggestion that led us on the rewarding research path.

I would like to thank Professor Daniel Strasser for sharing the enthusiasm on science in general and teaching me all details of the project when I first joined the group. His positive influence has encouraged me to continue the project and want to learn more about the ultrafast dynamics studies. I also greatly appreciate the help from Ben Doughty throughout the early graduate school years including the lab move and project transition. Without the suggestions and comments from Ben, the new velocity map imaging experiments would not have been possible. It has been a pleasure working with Professor Kyungwon Kwak for two years who is a wonderful source of knowledge on femtosecond laser systems and theoretical calculations. I very much enjoyed the company of Mihai Vaida in the lab and the office with his Romanian humor and German stories. In addition, I want to acknowledge Nare Janvelyan who have worked with me this last year and brought fresh air into the lab.

I would like to express my gratitude to the staff at the Advanced Light Source (ALS) for providing a wonderful facility and technical support for this research. I really appreciate the help and support from Kevin Wilson as without his advices the hypergolic reaction studies would not have been possible. I thank all the people that were involved in this project and have provided

tremendous help at the ALS including Oleg Kostko, Amir Golan, Chris Harmon, Chen-Lin Liu, and Denisia Popolan. It has been a wonderful time working at the ALS thanks to their generosity even though the experimental schedule was always stressful.

I cannot thank enough the whole Leone group with the warm atmosphere and the unconditional support. Memories of the annual Leone group ski trips will be cherished forever. I would like to offer special thanks to Kathleen Fowler and Adam Bradford whose constant behind-the-scenes efforts make the Leone Laboratory a much brighter place to work. I am deeply thankful for the departmental help especially during the move by the wood shop (Mike, Jody, and Ryan), the electrical shop (Cliff and Mani), and the building management (Alexei and Inna).

Forever I am indebted to my family, whose value to me only grows with age. It is their unwavering love and encouragement that have always kept me on my path. Their cheers even from far away Korea allowed me to pursue my dreams. I am also very thankful for the warm welcoming and care from Mariana and Dorel, my soon to be in-laws. Of course, I cannot go without mentioning my fiancé, Bogdan Negru, who has provided me with love and support through our five+ years. I am profoundly grateful for the shelter he gave me, as it was an escape from work when needed and brought me to the finishing line here and now. His enthusiasm for science and life motivates me to be a better person. As our love blossomed among the toughest time (1st yr graduate school) of our life I am sure that we can get through any other hard times in the future together wherever we end up.

Berkeley has given me all I have ever dreamed of, including love and science. The memories from Berkeley will have a special place in my heart.

Chapter 1

Introduction to Dynamics of Ionic Liquids

The study of molecular dynamics allows us to understand the molecular level mechanisms of elementary chemical and physical processes. Dynamics that are initiated either by chemicals or photons can be monitored along the process and the mechanisms of chemical reaction or photodissociation can be understood completely by capturing the clearest pictures of their reaction steps or excited states. Dynamics of novel compounds, ionic liquids, have been studied, providing fundamental knowledge on these photon or chemically initiated reaction processes. The first section of this chapter gives an overview of the novel compound, ionic liquids, and the second section of this chapter shows how isolated molecules of ionic liquids are generated in the gas phase for dynamics studies. Furthermore, the soft x-ray and extreme ultraviolet probing that is used for monitoring molecular dynamics will be discussed in Chapter 2.

1.1 Overview of Room Temperature Ionic Liquids

Molten salts are the most common term for ionic compounds in the liquid state and this term used to include "ionic liquids" long before there was much known about low melting salts. Ionic liquids are room temperature molten salts with melting temperature below the boiling point of water.[1] Ionic liquids are usually composed of an asymmetric organic cation and a halogenated anion or an organic anion. One of the earliest room temperature ionic liquids, ethylammonium nitrate (m.p. 12 °C), was synthesized in 1914 by Paul Walden.[2] Ionic liquids based on alkyl-substituted imidazolium and pyridinium cations, with halide or tetrahalogenoaluminate anions, were developed for use in battery applications in the 1970s and 1980s.[3-4] The past decade has seen an explosion of research devoted to the study of ionic liquids (ILs) as a new and remarkable class of materials. Ionic liquids have fascinating and diverse properties such as negligible vapor pressure, excellent thermal stability, high conductivity, high energy density, and distinctive reactivity.[5-8] Because of their remarkable properties, ionic liquids are studied in fields of organic chemistry,[9-10] electrochemistry,[11-12] physical chemistry,[13] materials engineering,[14] and others. In addition to those unique properties, tunability of ILs allows broad applications including catalysts,[15] batteries,[16-18] and rocket propellants[19-20] and ILs have found industrial applications[21] in chemical industry and pharmaceuticals.

The synthesis of hypergolic ionic liquids (spontaneous ignition when combined with another reagent) has stimulated interest in novel ways to store chemical energy for propulsion in ionic liquids.[22] These low-volatility, safe and hypergolic materials are of substantial importance to the

Air Force and numerous groups are searching for a more efficient and environmentally friendly hypergolic materials.[19-20, 23-25] Military researchers in the U. S. have recently developed a less corrosive and toxic rocket fuel system using a hydrogen-rich ionic liquid that is hypergolic with hydrogen peroxide as the oxidizer.[19] Understanding hypergolic reaction mechanisms and the physicochemical properties of hypergolic ionic liquids will provide an insight into designing a green rocket propellant and facilitate the search for other materials for specific applications.

Tunability of ILs is possible because of the wide range of the cation−anion (C^+-A^-) combinations. Ions of many different chemical structures can be incorporated in ILs, and Plechkova and Seddon estimate that it may be possible to pair those cations and anions to create as many as 10^{18} different possible ionic liquids.[21] These various pairings of ions change the physicochemical properties dramatically and allow tuning the molecular properties to serve as "designer solvents". However, the vast number of possible combinations makes it almost impossible to test all available ILs for specific applications. It is therefore valuable to understand in greater depth the fundamental properties of the isolated ion-pairs and to extrapolate and predict the features of ILs.

1.2 Generation of Isolated Ion Pairs in the Gas Phase

Due to their ionic nature, it was initially thought that ILs have essentially no vapor pressure. Studies showed that ILs could be distilled in vacuum with little thermal degradation despite their negligible vapor pressure in 2006.[26] However, characterization of isolated "gas-phase" systems was only very recent. In order to characterize the gas phase system of ILs, photoelectron spectroscopy,[27] single photon ionization[28] mass spectrometry, and electron impact[29] mass spectrometry have been used.

The gas-phase valence binding energy spectrum of ionic liquid vapor was obtained by photoionization of an effusive beam by extreme ultraviolet light.[27] The valence electronic structures of the ionic liquid vapor were in good agreement with the density functional theory (DFT) calculations[30] of the electronic structure of isolated cation–anion complexes and with the liquid phase measurements obtained with a HeII light source.[31] This similarity in electronic structure of the vapor and liquid phases show that thermal vaporization does not significantly change the electronic structure by decomposition. Furthermore, the identity of the species in the IL vapor was studied by single photon[27] or electron impact ionization[29] mass spectrometry and the predominant peak in the mass spectrum is the intact cation. It is suggested that the intact cations are produced by dissociative ionization of neutral ion pairs resulting in intact cations (C^+) and the neutral fragment of the anion (A^-) plus an electron, as shown in equation (1.1).

$$C^+A^- \rightarrow C^+ + A^0 + e^- \qquad (1.1)$$

The possibility of ion-pairs in the vapor phase was also considered and classical atomistic molecular dynamics simulations were carried out to compute the vaporization energetics of isolated ion-pairs and clusters.[27] Enthalpies of vaporization for clusters are significantly higher than isolated ion-pairs indicating that at moderate temperature isolated ion-pairs are the predominant species in the vapor. Various experimental methods, such as soft ionization[27-28, 32]

mass spectrometry,[26-27, 31] line-of-sight mass spectrometry,[29, 33] UV spectroscopy,[34] and cryogenic neon matrix-isolation FTIR spectroscopy[35] have also provided direct evidence of isolated ion pairs in the vapor.

However, there was a lack of fundamental understanding of isolated ion-pairs because of the rather late discovery of their volatility and of the nature of the vapor phase. Investigation of isolated ion-pairs can provide understanding of the ionic interaction and furthermore the photophysical properties of the isolated system. Soft X-ray or extreme ultraviolet (EUV) light is a universal probe to monitor the photo-initiated or chemical-initiated dynamics and is used to study the isolated ion pairs prepared in the ionic liquid vapor as discussed in Chapter 2.

Isolated ion-pairs are prepared in the vapor phase by thermal vaporization. The IL vapor source is composed of an aluminum oven with a glass interior to reduce the thermal decomposition by a metal surface. The aluminum oven body is heated by four home-built resistive heating cartridges to 400-500 K. The temperature of the aluminum oven is monitored using a K-type thermocouple located near the glass interior where the IL sample is held. A schematic view of the ionic liquid vapor source at the interaction region is shown in Figure 1.1.

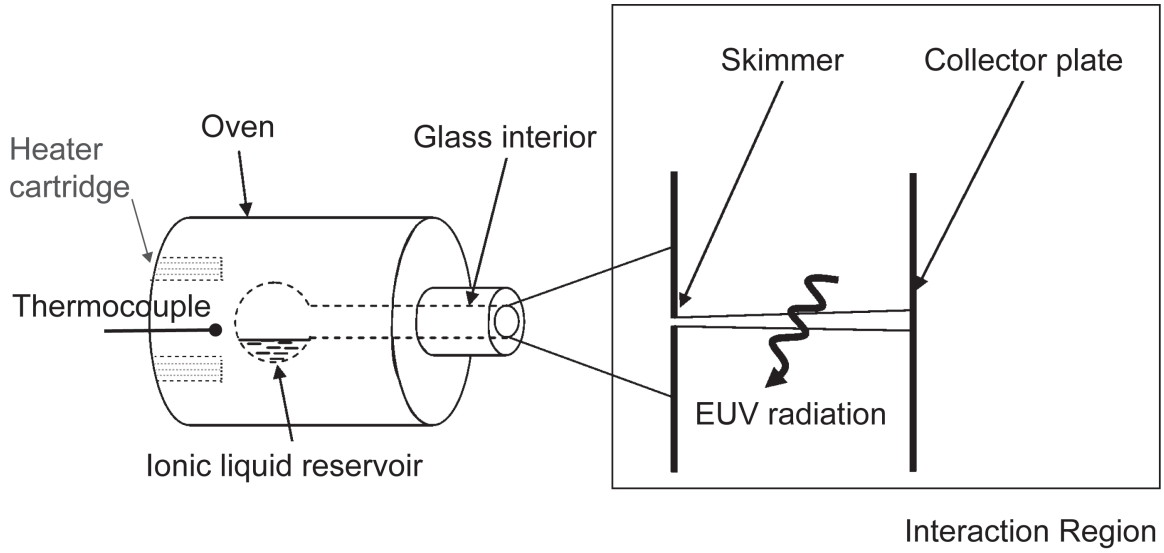

Figure 1.1. Schematic drawing of the effusive beam of ionic liquid vapor composed of isolated ion-pairs and the interaction region coupled to it. Effusive beams produced from various oven designs are probed by the extreme ultraviolet (EUV) light at the interaction region throughout the studies.

Chapter 2

Soft X-ray and Extreme Ultraviolet Probing of Molecular Dynamics

Extreme Ultraviolet light (EUV) and Soft X-ray radiation are located within the electromagnetic spectrum between the ultraviolet and harder X-rays. This spectral region is usually associated with sunburn and ionizing radiation and offers great opportunities for both science and technology. The extreme ultraviolet extends from photon energies of about 25 eV to about 250 eV, with corresponding wavelengths in vacuum extending from about 5 nm to 50 nm. The soft X-ray region extends from about 250 eV to several keV and matches well with the primary atomic resonances and absorption edges of most elements.[36] For ionic liquid studies, the extreme ultraviolet radiation is used for probing molecular dynamics either because their photon energies are near ionization threshold energies of most molecules or are sufficient for single photon ionization. This radiation above ionization serves as a universal probe and combined with photoelectron spectroscopy or time-of-flight mass spectrometry any molecules or intermediates can be monitored along the reaction coordinates. The extreme ultraviolet radiation that is used for ionic liquid studies, the tabletop source and the synchrotron source are discussed in the following sections.

2.1 Tabletop Extreme Ultraviolet Light

Recent developments in the generation of high-order harmonics with femtosecond laser pulses in rare gases offer excellent opportunities for the experimental investigation of dynamical processes in atoms and molecules. High harmonics are tunable tabletop sources of extreme ultraviolet light and soft X-ray radiation.[36] The harmonics result from a strongly non-linear interaction with the electric field of the femtosecond laser pulse and the noble gas atoms, either He, Ne, Ar, or Xe. High harmonic generation in atoms is well understood in terms of the three step model (ionization, acceleration, and recombination) by Corkum in 1993.[37-38] High harmonics are strongly dependent on the driving laser field and are laser-like, producing coherent, directional, ultrafast light pulses with photon energies from 5-200 eV. With this range of energies, both valence and core level spectroscopy are possible and the ultrafast nature of the high harmonic pulses allows time-resolved studies.

Typically a driving laser with a wavelength of 800 nm and duration of 20−100 fs is focused to an intensity of 10^{14} W/cm^2 to 10^{15} W/cm^2 in a noble gas medium. It generates a wide range of energies of very strong, well-defined odd harmonics as shown in Figure 2.1.[39] The experimental system used to generate high harmonics for ionic liquid studies is discussed in the following

section 2.1.1 in detail. In order to use a well-defined single photon energy pulse as an ionization probe, a single odd harmonic can be separated from the wide range of high-order harmonics using an EUV monochromator. The design of the EUV monochromator used for ionic liquid studies is shown in the next section 2.1.2.

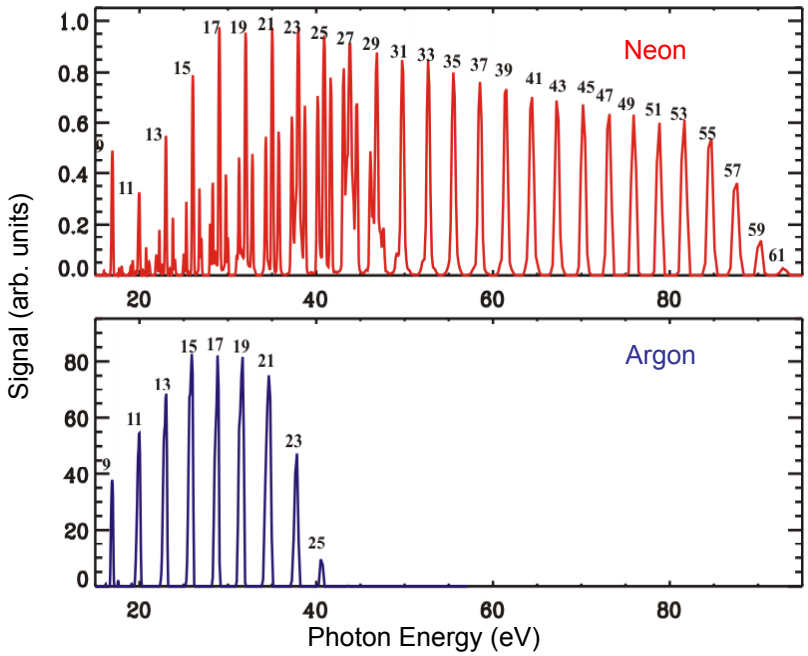

Figure 2.1. High harmonics generated in neon (upper) and argon (lower). It generates a wide range of energies of very strong, well-defined odd harmonics. Note the lower energy cutoff in argon, the higher intensity from argon and the overlapping orders of the grating in the neon spectrum. Figure is adapted from a previous study published in 2002.[39]

2.1.1 Laser System and High Harmonic Generation

An amplified femtosecond laser system is used for high-order harmonic generation. The amplified Titanium:sapphire laser system is composed of an oscillator, a pump laser, and an amplifier. The oscillator, Tsunami from Spectra Physics, is pumped by a frequency doubled 5W Nd:YVO_4 pump laser, Millenia VsJ from Spectra Physics, to produce a mode locked seed pulse with 400 mW power and 35 fs pulse duration at 82 MHz repetition rate. An Evolution 30 pump laser from Spectra Physics is used to pump the Titanium:sapphire amplifier system (Spitfire HPR or Spitfire, Spectra Physics) that is seeded with the output of the oscillator.

Two different laser systems were used for the ionic liquid studies, velocity map ion imaging (Chapter 3) and time-resolved mass spectrometry (Chapter 4). Using the same type of Tsunami oscillator and pump laser, two different amplifier systems, Spitfire HPR and Spitfire, were used to produce pulse durations of 45 fs and 80 fs pulses, respectively. Both systems produced about

2.2 mJ pulses at 1 kHz repetition rate with a center wavelength that is tunable between 790 nm and 810 nm.

High-order harmonics are generated by focusing the output of the Titanium sapphire amplified laser into a gas cell filled by argon gas. A gas cell with 200 μm input/output holes and 1.5 mm path length has replaced the pulsed jet that was used for high harmonic generation in the group for previous studies. The hole size of the gas cell was carefully chosen to maximize the harmonic yield with the smallest hole size. For example, a gas cell with 100 μm input/output holes yielded fewer harmonic photons. Argon gas pressure is optimized to maximize the number of photons for the 15^{th} or 17^{th} harmonic at 2.6×10^{-4} Torr measured background in the high harmonic generation chamber with a base pressure of 4×10^{-8} Torr. The harmonic yield is optimized before all experiments using argon and nitrogen gas as a reference.

2.1.2 Extreme Ultraviolet Light Monochromator

Two different extreme ultraviolet light monochromator are used for the ionic liquid studies, velocity map ion imaging (Chapter 3) and time-resolved mass spectrometry (Chapter 4). For the velocity map ion imaging studies in Chapter 3, the high-order harmonic of interest is selected and refocused by an EUV monochromator system that consists of a plane grating, cylindrical mirror, and a toroidal mirror. The rough schematic of this EUV monochrmator system is shown in Figure 2.2.

The gold coated plane grating (Zolo Tech) with uniform line separation of 600 lines/mm and a blaze angle of 3.4° is used at a distance of 25.4 cm from the high harmonic generation source.

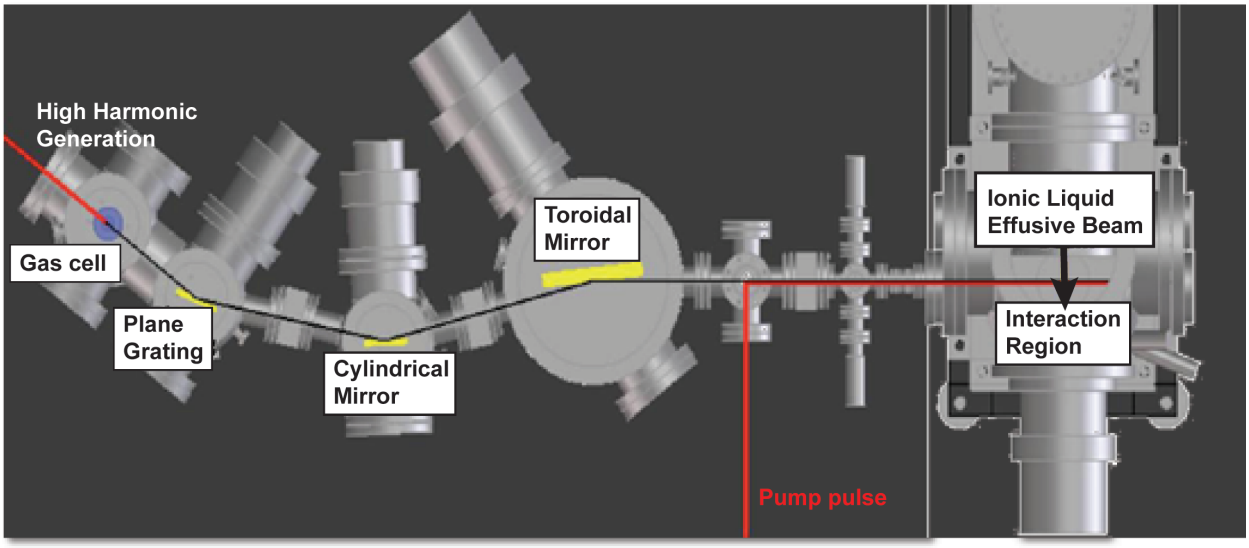

Figure 2.2. A schematic drawing of the extreme ultraviolet light monochromator used for velocity map ion imaging studies of ionic liquids. High-order harmonics generated at the gas cell are selected and refocused by the EUV monochromator that consists of a plane grating, cylindrical mirror, and a toroidal mirror. The harmonic of interest interacts with the ionic liquid vapor at the interaction region where the pump pulse is overlapped with the harmonic probe for time-resolved measurements.

The total angle of the grating is 155° and is operated at first order diffraction for all experiments. By rotating the grating relative to the incoming light, which changes the incidence angle, the high-order harmonic of interest is selected. The following cylindrical mirror and toroidal mirror are used to refocus the selected harmonic to a Gaussian profile at the interaction region. The distance between the plane grating and the cylindrical mirror is 44.7 cm and between the cylindrical mirror and the toroidal mirror is 50.0 cm. The angle of incidence for the cylindrical mirror (ARW Optics) is 77.5° and the radius of curvature of this mirror is 500 cm. The toroidal mirror (ZoloTech) with a 798 cm major radius of curvature and a 13.9 cm minor radius of curvature has an incidence angle of 83.0°. The interaction region is away from the toroidal mirror by 1094.7 cm and the two beams, harmonic and pump pulses, are overlapped at a 1-2° angle.

Each harmonic is identified by kinetic energy measurements of photoelectrons. Using velocity map imaging, the ion optics were set for electron detection (negative mode) and argon gas was used as a target gas to distinguish the 13^{th}, 15^{th} and 17^{th} harmonics as their ejected photoelectrons have different kinetic energies of 4.3, 7.4, and 10.4 eV, respectively. Using a time-of-flight photoelectron spectrometer, the harmonics are found similarly as using the velocity map imaging only by measuring the time-of-flight of photoelectrons instead of taking images.

To find the overlap of the two beams, harmonic and pump pulses, a BBO crystal is used at the interaction region. The zero-order from the high-order harmonic generation is used to find the time zero with the 800 nm pump pulse. When two pulses are overlapped spatially and temporally a blue spot is observed after the BBO crystal. After finding the overlap with the zero order and a pump light, it is much easier to find an overlap with the high-order harmonics and pump pules. For time-resolved measurements using the 15^{th} harmonic as a probe, the overlap of pump (800 or 400 nm) and probe (54 nm) is found using helium gas as a target gas. Atomic helium gets excited to the 1s3p or 1s4p resonance by the 15^{th} harmonic (54 nm) and can be probed by a sequential ionization using an 800 or 400 nm pulse. The instrumental response of the system is determined from this resonant two photon ionization of atomic helium. The convolution of the two pulses with a step function is measured in time by scanning the delay between the pump and probe pulse. A representative time-resolved spectrum of helium ion obtained by velocity map ion imaging, which is illustrated in Chapter 3, is shown in Figure 2.3. The instrumental response function is obtained by fitting the data to the following function (equation (2.1)).

$$S(t) = A\left[1 + erf\left(\frac{(t-t_0}{\sqrt{2}\sigma}\right)\right] + d \qquad (2.1)$$

The instrumental cross correlation (σ) is found from the fit where *S(t)* is the transient signal, *A* is a free fit amplitude, t_0 is the delay time offset of the temporal overlap, and the *d* is an offset. Typically the instrumental response was found to be in the range of 80-150 fs in the experiments.

For the time-resolved mass spectrometry studies in Chapter 4, the high-order harmonic of interest is selected and refocused by an EUV monochromator system that consists of a spherical grating and a toroidal mirror. The rough schematic of this EUV monochrmator system is shown in Figure 2.4. Details and characterization of the system are discussed in a previous study.[39]

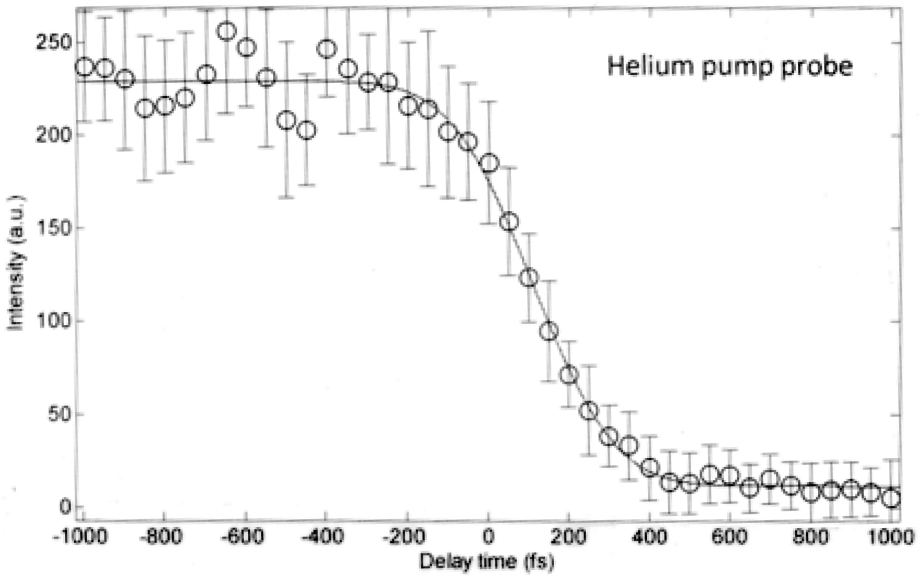

Figure 2.3. Time-resolved spectrum of helium ion (4 amu/q) obtained by integrating over a 5-bin energy region (zero kinetic energy region). Positive time is where the 800 nm pulse arrives before the 15th HH pulse, while negative time corresponds to a delay where a delayed 800 nm pulse ionizes the atomic helium that is excited by the 15th HH pulse.

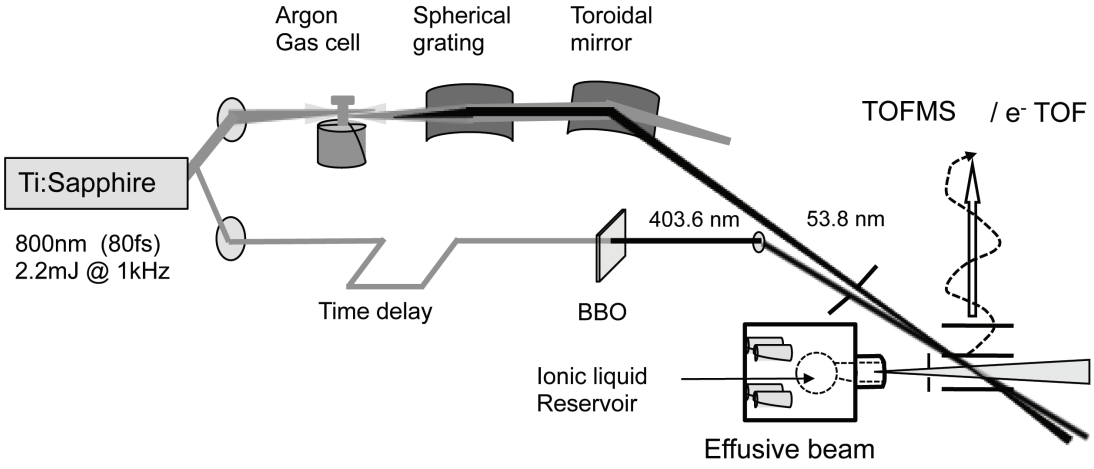

Figure 2.4. A schematic drawing of the extreme ultraviolet light monochromator used for time resolved mass spectrometry studies of ionic liquids. High-order harmonics generated at the gas cell are selected and refocused by the EUV monochromator that consists of a spherical grating and a toroidal mirror.[39] The harmonic of interest interacts with the ionic liquid vapor at the interaction region where the pump pulse is overlapped with the harmonic probe for time-resolved measurements.

2.2 Synchrotron Radiation

Extreme ultraviolet and soft x-ray radiation can also be obtained from a synchrotron source. It is well known that an electron accelerated in a magnetic field will emit radiation.[36] In a synchrotron, electron bunches travel nearly the speed of light, forced into a circular path by magnets, and then emit bright ultraviolet and x-ray light in modulators or bend magnets that is directed down beamlines to experiment endstations. With the close proximity of the Advanced Light Source (ALS) to the femtosecond high harmonic laboratory at UC Berkeley, ionic liquids were studied using the synchrotron radiation from the Chemical Dynamics Beamline T3 (9.0.2.3) and T1 (9.0.2.1) in the past several years. Together with Air Force Research Laboratory scientists Steven Chambreau and Ghanshyam Vaghjiani, new experiments have been performed to study the thermodynamic properties and the hypergolic reaction dynamics of ionic liquids.

The Chemical Dynamics Beamline studies the fundamental chemical processes using tunable EUV light between 7.4 eV and 30 eV that is generated by an undulator at the ALS. The tunability of the ALS provides an advantage compared to the tabletop source of EUV radation in one aspect despite of its long pulse duration. With a continuously tunable light source, threshold photoionization energies can be determined. As molecules usually have inherent characteristic ionization potentials, it is possible to distinguish molecules even with same masses such as isomers using this tunable EUV radiation. In other words, photoionization efficiency (PIE) measurements allow identification of molecules. In order to identify the unknown reaction intermediates upon thermal decomposition or hypergolic reaction, PIE measurements were performed at the Chemical Dynamics Beamline T3 and T1.

Both end stations, T3 and T1, use time-of-flight mass spectrometry to detect the molecules in the gas phase using tunable EUV light. However, the T1 end station is optimized for aerosol particle studies whereas the T3 end station is more suitable for effusive or supersonic beam studies. The following sections will discuss the details of each end station.

2.2.1 Beamline 9.0.2.3 for Effusive Beam Studies

The T3 beamline of the Chemical Dynamics Beamline is typically used for "effusive or molecular beam" studies of various molecules of interest. The experiments are performed on a "molecular beam" apparatus coupled to the Chemical Dynamics Beamline at the ALS.[40-41] An effusive beam or supersonically expanded beam is used to introduce the molecules into the gas phase. The molecules introduced into the gas phase are ionized using tunable photon energies between 7.4 eV and 15 eV are detected using a reflectron mass spectrometer. The T3 end station provides medium resolution of monochromatized light with a bandwidth of about 10-50 meV and a photon flux of about 10^{13} photons/s.

In the ionization region the ionic liquid effusive beam is interrogated using a commercial reflectron mass spectrometer (R. M. Jordan) by the tunable undulator EUV radiation. The ion optics for the mass spectrometer are pulsed since the synchrotron radiation is quasicontinuous (500 MHz). The repeller plates are turned on (1800 V) versus off (1600 V) when the TOF ion

packet arrives, with a gating rise time of 100 ns and dwell time of 5 μs. Accelerated ions are reflected in the electrostatic field of the ion mirror and are detected by a 25mm diameter microchannel plate (MCP). The time-of-flight signal from the MCP is amplified by a fast preamplifier (Ortec, VT120A) and collected by a multichannel-scalar card (FAST-Comtec, P7886). Time-of-flight spectra are recorded as a function of photon energy between 7.4 eV and 15.0 eV with a Labview program on a PC computer. The synchrotron EUV photon flux is measured by a Si photodiode (IRD, SXUV-100) and all mass spectra are normalized by the photon flux. Since the ALS updated the system to the "top-off" mode of operation in 2009,[42] the beam has 500 mA of average storage-ring current instead of the beam decaying between fills from 400 mA to 200 mA. During the "top-off" mode of operation, photon flux measurement was not necessary when measuring a mass spectrum at fixed photon energy. The photon flux was still measured during the PIE curve measurements at the "top-off" mode.

Ionic liquid effusive beams were generated to study the vaporization process including isolated ion pair generation and thermal decomposition processes. Initially the single stage ionic liquid vapor source shown in Figure 1.1 was used. Because the ionic liquids can decompose even during their vaporization process, we constructed a two-stage oven based on the principle of an arsenic cracker cell that has two independently heated regions, one to set the vapor pressure of the ionic liquid reservoir and the other to heat the vapor to cause thermal decomposition in a lower pressure regime as the vapor exits the oven (Figure 2.4). This eliminates bimolecular collisions as a source of fragments from reactive chemistry. This oven was constructed in the shops prior to the second series of runs at the Advanced Light Source. Hypergolicity must produce a rapid heat release, by reaction, in a small volume. The understanding of thermal decomposition processes is therefore important in understanding ignition also.

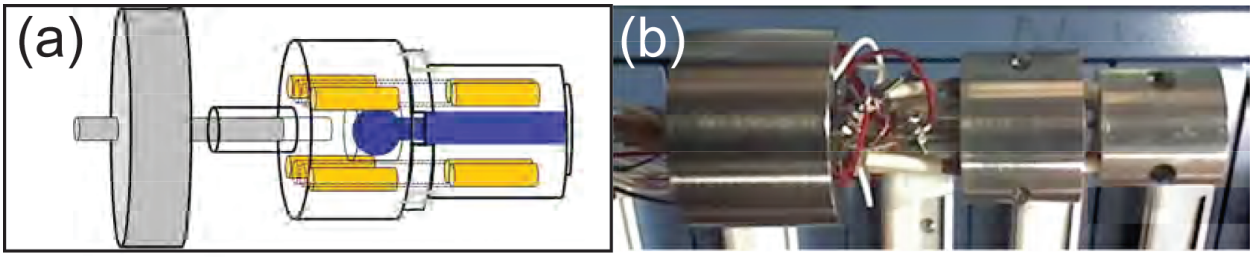

Figure 2.4. Two-stage oven used for ionic liquid thermal decomposition studies at the Advanced Light Source. (a) Schematic drawing of the two-stage oven where the heater cartridges are shown in yellow and the glass sample vial is shown in blue. (b) The final aluminum oven used for the experiments.

2.2.2 Beamline 9.0.2.1 for Aerosol Source Studies

The T1 beamline of the Chemical Dynamics Beamline is typically used for "Aerosol particle" studies of various molecules and reactions of interest. The experiments are performed on this "Aerosol Mass Spectrometer (AMS)" apparatus, shown in Figure 2.5, coupled to the Chemical Dynamics Beamline at the ALS.[43] An aerosol particle source is used to introduce the molecules

into the gas phase. The molecules vaporized from the aerosol particles are ionized using tunable photon energies between 7.4 eV and 15 eV and detected using the aerosol mass spectrometer. The T1 end station provides low resolution of monochromatized light with a bandwidth of about 100-300 meV and a photon flux of about 10^{15} photons/s.

Aerosol particles are used to study reaction kinetics of biomolecules, atmospheric particles, and ionic liquids in this case. They provide great advantage in monitoring the intact molecules by resulting in less photofragmentation upon ionization. The aerosol method is further discussed in Chapter 6. For time-of-flight (TOF) analysis of molecules in the gas phase, the aerosol particles are introduced into an aerosol mass spectrometer (AMS), shown in Figure 2.5, which was designed and constructed at the Chemical Dynamics Beamline.[43] The aerosol particles are directed through a 200 μm diameter flow-limiting orifice (0.3 SLM) and then into an aerodynamic lens, which consists of five apertures. Aerosol particles with diameter of 70 nm to 1000 nm are focused to the interaction region using the aerodynamics lens, shown in Figure 2.5A. Before the interaction region the aerosol beam passes through a 2 mm conical skimmer and a 4 mm aperture (Figure 2.5B). At the interaction chamber, the aerosol particles are thermally vaporized on a heated copper block located between the ion optics.

The cone shaped plume of vapor generated from the aerosol particles is subsequently ionized with the tunable EUV. The synchrotron radiation is passed through an argon gas filter and two MgF_2 windows to remove high harmonics produced by the undulator. When using the photon energy above 11 eV the MgF_2 windows were not used. The synchrotron beam size is around 200 μm in the interaction region where the vaporized molecules are ionized. The ions are interrogated by the AMS apparatus, obtaining time-of-flight (TOF) spectra. All TOF spectra are recorded using a MCP detector and then a multichannel scaler card on a PC computer. Mass spectra are collected either as a function of photon energy to obtain PIE curves or as a function of reactant concentration at a fixed photon energy to measure the reaction kinetics.

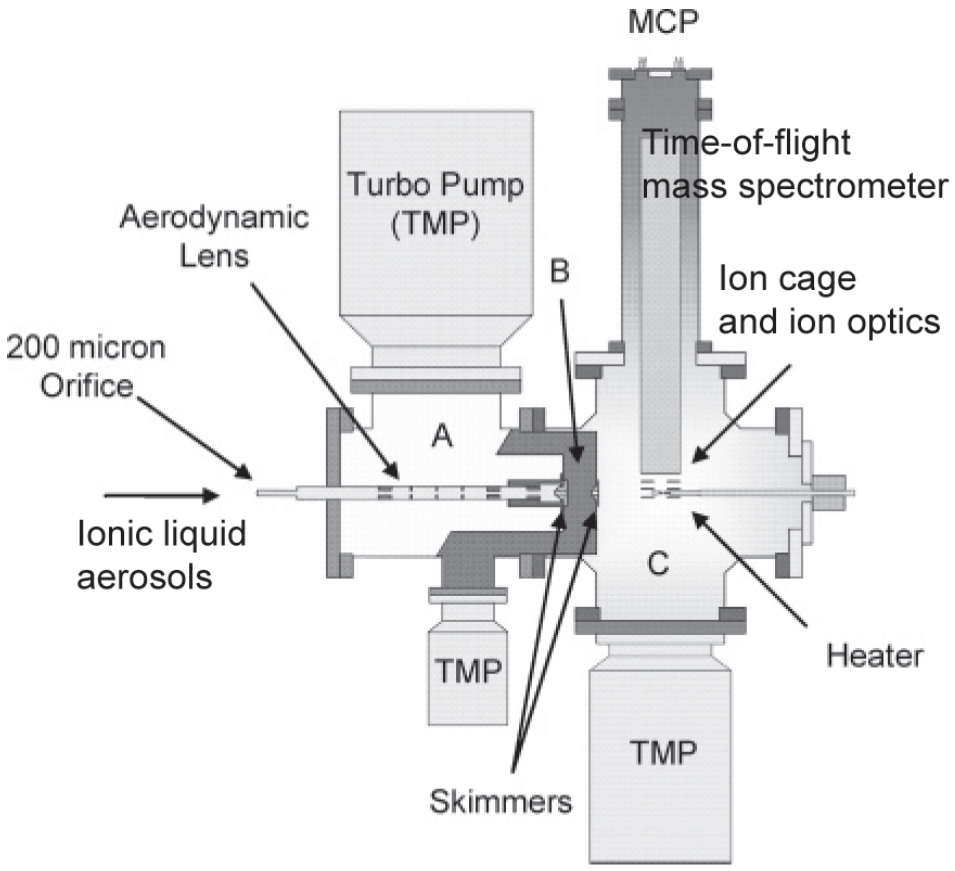

Figure 2.5. Schematic view of the Aerosol Mass Spectrometer (AMS)[43] used at the Chemical Dynamics Beamline 9.0.2.1. Aerosol particles are introduced through the aerodynamics lens (A) and pass through skimmers (B). These particles are vaporized on the heated copper block and the vaporized molecules are ionized by the tunable EUV at the interaction region (C).

Chapter 3

Simultaneous Ion Pair dissociation and Dissociative Ionization of an Ionic Liquid: Velocity Map Imaging of Vacuum-ultra-violet-excited 1-ethyl-3-methy-imidazolium bis(trifluoromethylsulfonyl)imide

*The content and figures of this chapter are reprinted or adapted with permission from Koh, C. J.; Leone, S. R., "Simultaneous Ion Pair dissociation and Dissociative Ionization of an Ionic Liquid: Velocity Map Imaging of Vacuum-ultraviolet-excited 1-ethyl-3-methy-imidazolium bis(trifluoromethylsulfonyl)imide," Mol. Phys., **2012**, 110, 1705-1712. Copyright 2012 Taylor & Francis.*

Isolated gas-phase ionic liquid (IL) molecules, 1-ethyl-3-methylimidazolium bis(trifluoromethyl-sulfonyl)imide ($[Emim]^+[Tf_2N]^-$), are excited by laser-produced high-harmonic extreme ultraviolet light in the 17−26 eV range and the ions are probed by velocity map imaging. The velocities of the intact cation, $Emim^+$, and intact anion, Tf_2N^-, are recorded in separate velocity map images. The kinetic energy distribution of the intact cation has both slow ions arising from previously reported dissociative ionization and fast ions from ion-pair dissociation of the neutral isolated ionic liquid (positive and negative ion pairs) where the branching ratio is approximately 0.18 ± 0.02:0.82 ± 0.02. The intact anion is also detected with a momentum that complements the higher velocity intact cation fragment, indicating that the process arises from two-body dissociation of the neutral ion-pair. Similar angular distributions for the anion and the higher velocity cation indicate that the electronic transition, which is above the ionization threshold and leads to ion-pair dissociation of the neutral, has a dipole moment perpendicular to the dissociating ion-pair bond. Observation of the ion-pair dissociation upon photoexcitation of the IL vapor not only reveals a previously unobserved photodissociation pathway for the ionic liquid, but it also provides direct evidence for the existence of the ion pairs in the isolated gas phase molecules.

3.1 Introduction

Room temperature ionic liquids (RTILs) are ambient temperature molten salts[1] usually consisting of an asymmetric organic cation and a halogenated anion or an organic anion.

Coulombic forces between the ions are the dominant interaction in ionic liquids (ILs), which contribute to their unique properties such as low volatility, high thermal stability, electrical conductivity, and solvation ability.[6, 17-18, 44-50] Because of their distinctive properties, ILs are studied in many fields and for many applications including catalysts,[15] batteries,[16-18] and rocket propellants.[20, 23-24, 51] For their task-specific usage, physicochemical properties of ILs can be tuned based on the cation−anion (C^+-A^-) combinations with a vast number (10^{18}) of possible pairings.[21] The interaction between the isolated cation and anion, which primarily determines the electronic and nuclear structure, is therefore important to understand in detail. The electronically excited states of the IL ion-pairs is a subject for which little is known.

Isolated ion-pairs can be prepared in the gas phase by thermal vaporization despite the extremely low vapor pressures of ILs.[8, 27-29, 34-35, 52-58] Vaporization of ILs was shown in 2006[26] and has led to a wealth of studies including the topics of heats of vaporization,[29, 53, 59] interactions at the liquid-vapor interface,[60-61] and the spectroscopic nature of the gaseous phase ILs.[32, 35, 62] Both experimental[27, 29, 35, 54] and theoretical[55, 59, 63-64] studies showed that the ionic liquid vapors are composed of neutral ion-pairs under moderately high temperature and low pressure. The existence of the vaporized neutral ion-pairs is observed directly by field ionization[54] and indirectly by soft ionization mass spectrometry,[27-28, 53] line-of-sight mass spectrometry,[29, 56] fourier transform ion cyclotron resonance mass spectrometry,[35] and UV spectroscopy.[34] As one evidence for isolated ion-pairs in the gas phase, specifically cation−anion 1:1 pairs (C^+A^-), the intact cation (C^+) is observed upon photoionization of the IL vapor, having been produced by dissociative ionization.

Recent works[27-28] have reported isolated ion-pairs of 1-alkyl-3-methyl-imidazolium-based ionic liquids combined with the bis(trifluoromethylsulfonyl)imide [Tf_2N] anion in the gas phase, and ionization of the ion-pairs result in a predominant product, the intact cations, 1-alkyl-3-methylimidazolium, observed by soft ionization mass spectrometry. Photoelectron spectra and photoionization efficiency curves in the near threshold ionization region of those isolated ion pairs have shown convincing evidence[27-28] that the predominant ionization mechanism is dissociative photoionization. However, the ionization and dissociation mechanisms have not been studied in greater depth, even for the predominant dissociative ionization channel.

Velocity map imaging (VMI) is employed to investigate the ionization and dissociation mechanisms of isolated ion pairs in depth. VMI is an experimental technique capable of determining the complete product velocity distribution, including the energy and angular distributions of photoions or photoelectrons. A two-dimensional detector is used to collect the accelerated electrons or ions by the electrostatic ion optics with 100% collection efficiency. All particles with the same initial velocity vector arrive at the same spot on the detector. Centroiding, which determines the center of the distribution of each spot, allows identification of each ion or electron hit, increasing the velocity resolution. In this study, velocity map ion imaging is used to study the photodissociation pathways by recording the velocity of photoions. Ion images of the specific photoions can be obtained selectively by combining the time slicing technique with the velocity map ion imaging method. The slicing technique is used to collect an ion image at a small window of time-of-flight by turning on the detector at the time-of-flight of the photoion of interest.

In the present work, dissociative ionization and photodissociation of an isolated ion-pair of an ionic liquid are investigated using mass-selected, time-sliced velocity map ion imaging[65-66] initiated by laser-produced high-harmonic extreme ultraviolet excitation. Velocity map ion imaging[67-68] provides the velocity and angular distributions of the photoionization products, and a desired photofragment can be mass-selected by a narrow-time detector gate that slices a part of the time-of-flight. Using this time-sliced velocity map ion imaging method,[65-66] velocity and angular distributions of the photofragments of interest are obtained selectively, and the photodissociation dynamics involving the fragments can be understood in greater depth. In this study, we focus on the intact cation and the intact anion fragments to reveal that the photodissociation dynamics consist of both ion-pair dissociation of the neutral ($C^+A^- + h\nu \rightarrow C^+ + A^-$) as well as dissociative ionization (equation (1.1) in Chapter 1) channels that produce these intact ions.

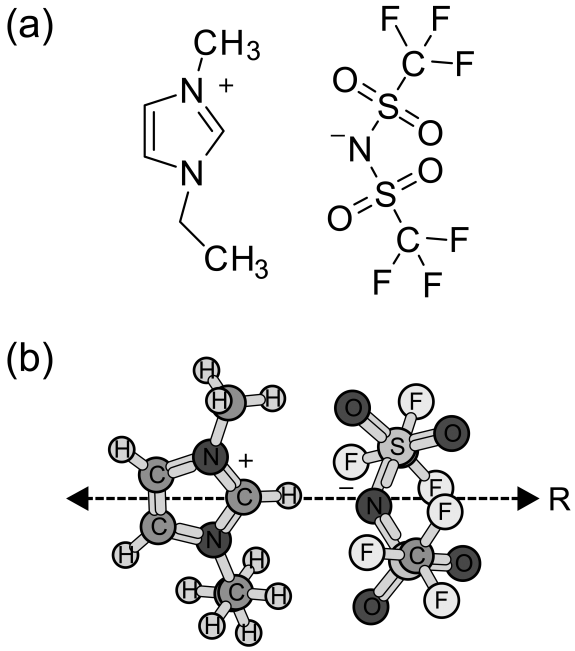

Figure 3.1. Schematic molecular structure drawing of ionic liquid, (a) 1-ethyl-3-methyl-imidazolium ([Emim$^+$]) bis(trifluoromethylsulfonyl)imide ([Tf_2N^-]), [Emim]$^+$[Tf_2N]$_-$, and (b) its optimized structure with one of the possible dissociation axis (R).

3.2 Experimental Methods

Isolated ion-pairs of the ionic liquid, 1-ethyl-3-methylimidazolium bis(trifluoromethyl-sulfonyl)imide, molecular structure shown in Figure 3.1, are prepared in the gas phase and are excited with extreme ultraviolet (EUV) light in the 17 − 26 eV range. Photoions, both cations and anions, generated upon dissociative photoionization and direct dissociation of the electronically excited ion-pair neutral molecules are focused to the microchannel plate detector, which has diameter of 75 mm and is gated at the time-of-flight of interest. The distance between the ionization region to the detector is 46.5 cm. For the intact cation mass (110.5-112.5 amu), the

gating window is 6.4-6.8 μs, meaning the detector is on only during a 6.4-6.8 μs delay time at the 2.9 kV(repeller)/2.1 kV(extractor) focusing. For the intact anion mass (279-281amu), the gating window is 9.5-10.0 μs, and the voltages are modified for negative ion detection. The gating time is calibrated by measuring the TOF of helium, argon, and xenon. The typical gating times (μs) for corresponding masses (amu/q) are shown in Figure 3.2 for three different focusing conditions of ion optics. Each velocity map image of the intact cation and the intact anion is obtained and the kinetic energy distribution of the ion is extracted by radial integration where each pixel is weighted with the usual ρsinθ (ρ electric field/ion's initial kinetic energy, θ: angle between the velocity vector and the laser polarization direction).[65] The laser polarization is parallel to the detector face and to the direction of the effusive beam. Each set of experiments is repeated 5 times for the intact cation measurements and 3 times for the intact anion measurements. Uncertainties of the center of each kinetic energy distribution are found from Gaussian fitting with an R^2 value of 0.9985.

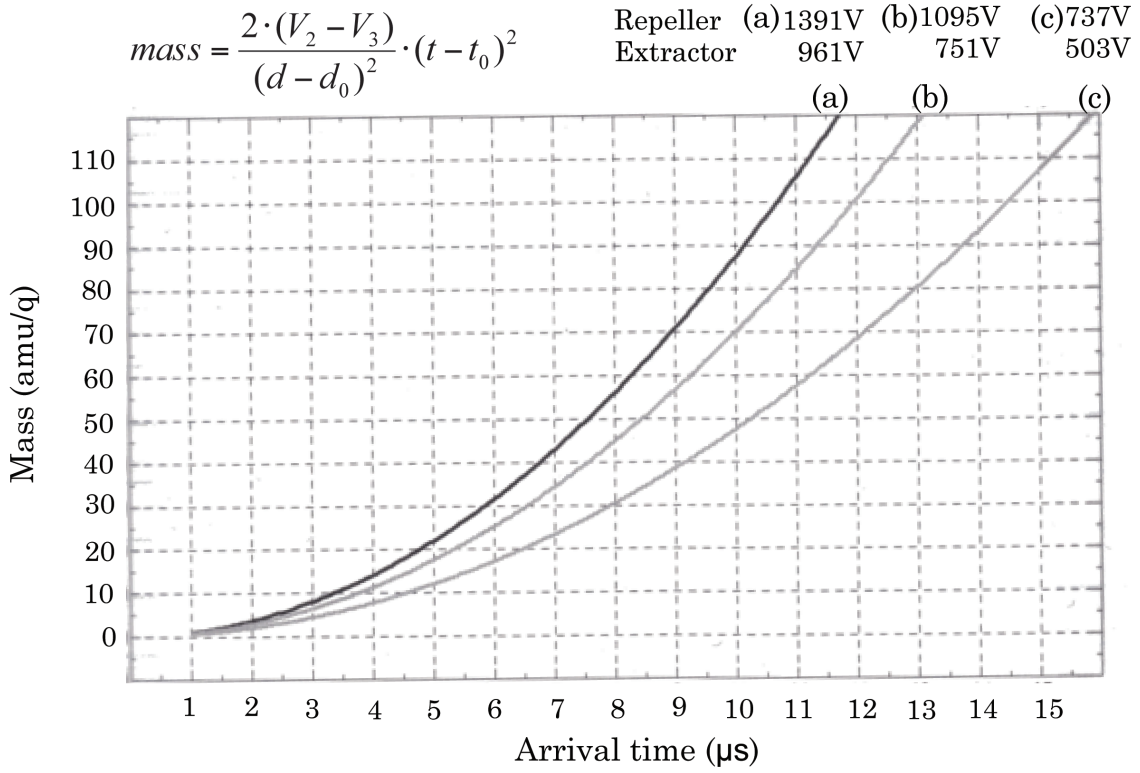

Figure 3.2. The mass (amu/q) of photoions as a function of typical gating time (μs), which is the arrival time (μs) of photoions at three different focusing conditions (a) 1391/961 V, (b) 1095/751 V, and (c) 737/503 V of ion optics, repeller/extractor.

Ionic liquid vapor is generated from a glass vial reservoir inside an aluminum oven body, heated by heating cartridges, as in previous studies. Ionic liquid sample, $[Emim]^+[Tf_2N]^-$ (Sigma, ≥97% purity), was heated at 323 K overnight under vacuum (~10^{-8} Torr) to remove impurities in the sample. The effusive beam was produced at 453 K, a temperature that is well under the thermal decomposition temperature of the IL (T_d, 675 K[1]), and the beam is skimmed by a 0.5 mm skimmer before the molecules are excited by the extreme ultraviolet (EUV) light.

High-order harmonic generation, a table-top laser setup, provides the EUV light in the 17 − 26 eV range, photon energies that are well suited for soft ionization and excitation mass spectrometry. The experimental high-order harmonic generation setup, previously described in detail,[69-73] consists of a 795 nm wavelength, 1.9 mJ, 45 fs, 1 kHz repetition rate Ti:sapphire pulsed laser that is focused into an argon gas harmonic cell. In this study for single photon ionization and photofragmentation, the 11th, 13th, 15th, and 17th harmonics are selected and refocused to the interaction region by a homebuilt EUV monochromator composed of a plane grating, spherical mirror, and a toroidal mirror.

The resulting photoions are projected by an electrostatic lens to a two-dimensional position sensitive detector in a velocity map imaging (VMI) setup. The lens voltages and the signs of the potentials are chosen such that the desired velocity map focusing is obtained for cations or anions. The ion imaging apparatus was used without significant modification from previous studies. The repeller was kept at 2928 kV and 1394 V, and the extractor was at 2053 V and 969 V, for high voltage (875 V) and low voltage (425 V) focusing conditions, used to detect high and low kinetic energy ions, respectively. As noted, the detector is gated for selective velocity map ion mass images by turning on the MCP detector back plate (1650 V) at a time-of-flight of the ions of interest and by turning it off (1200 V) at all other times. The images of ion hits on the phosphor screen are recorded by a charge-coupled device (CCD) camera at 60 Hz rate interfaced with a computer.

Ab initio calculations to obtain energetics are carried out at the HF/6-31+G(d,p) level of theory using Gaussian03.[74] The HF level of calculation is used despite its shortcomings, which are mainly the influence of dispersion interaction, compared to higher levels of theory, in order to estimate the energetics. The geometry of the molecule is optimized to a minimum and is shown in Figure 3.1(b). The asymptotic energy of the neutral ion-pair dissociation of 3.1 ± 0.2 eV is calculated by separating the cation and anion on an axis of the point charges, labeled (R) in Figure 3.1(b), keeping the geometry and charge of the ions the same. Calculations were performed at 298 K and the energies are corrected for the zero point energies. The asymptotic potential of the dissociative ionization state of 9.2 ± 0.2 eV, which is slightly higher than the experimental asymptotic energy of 8.9 ± 0.2 eV,[28] is calculated by removing an electron from the optimized geometry and taking the ions apart along the possible dissociation axis (R). The two channels, dissociative ionization and ion-pair dissociation, are presented in the schematic potential energy diagram using the calculated energies in Figure 3.3.

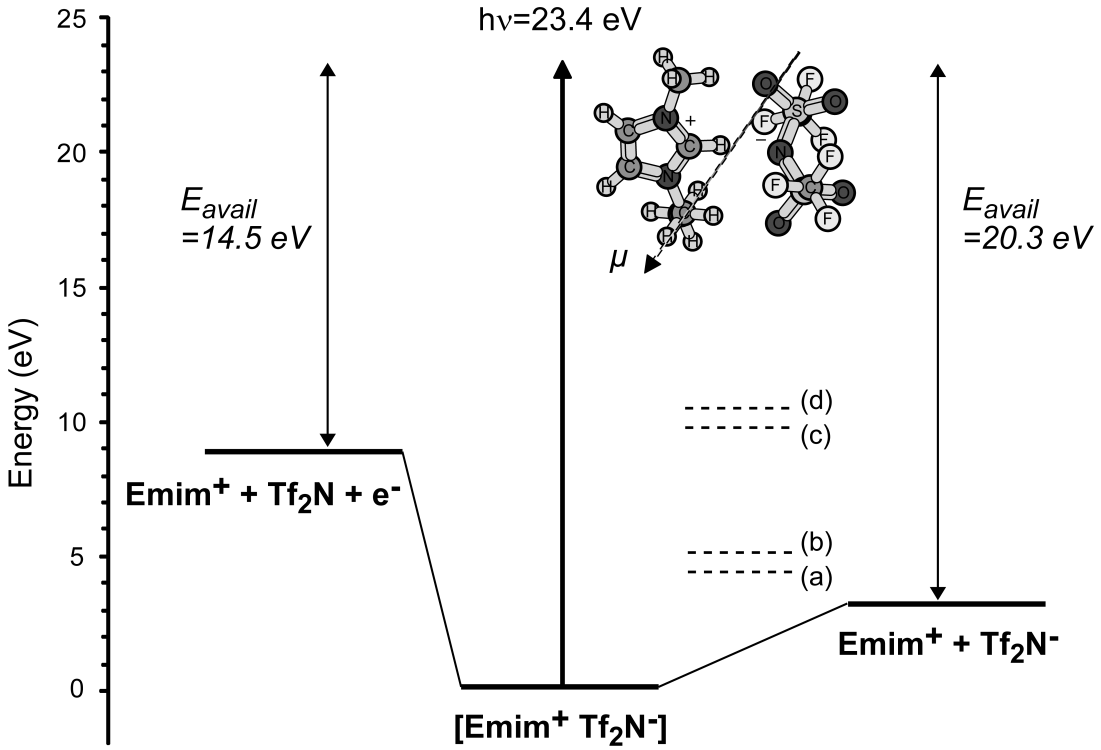

Figure 3.3. Schematic potential energy diagram of ionic liquid, $[Emim^+][Tf_2N^-]$. Ion-pair dissociation ($Emim^+ + Tf_2N^-$) with calculated asymptotic energy of 3.1 eV and dissociative ionization ($Emim^+ + Tf_2N + e^-$) with experimental asymptotic energy of 8.9 eV [28] is shown and their available energy of 20.3 eV and 14.5 eV, respectively, is presented at photon energy of 23.4 eV. Some of the possible photodissociation states (a)−(d) that could have curve crossings with the ion-pair dissociation channel, producing experimentally observed[27] 1-ethylimidazolium (Eim^+) or 1-methylimidazolium (Mim^+) upon photo-excitation at 23.4 eV, with estimated asymptotic energies based on previous photoionization studies[74] are shown in dotted lines (---) as an example ((a) $Eim^+ + CH_3 + Tf_2N^-$, (b) $Mim^+ + CH_2CH_3 + Tf_2N^-$, (c) $Eim^+ + CH_3 + Tf_2N + e^-$, (d) $Mim^+ + CH_2CH_3 + Tf_2N + e^-$).

3.3 Results and Discussion

The intact cation, $Emim^+$, that is produced by extreme ultraviolet excitation at 23.4 eV (15th harmonic) of the thermal beam of ionic liquid, $[Emim]^+[Tf_2N]^-$, is measured for low kinetic energies by velocity map ion imaging in Figure 3.4(a). The intact cation image collected with low voltage focusing ion optics (425 V) exhibits slow ions with nearly zero kinetic energy. The kinetic energy distribution is found from the radial integration and plotted in Figure 3.4(b). Kinetic energy of the intact cation is compared to the kinetic energy distribution formed by ionizing thermal argon gas to produce argon ions that have essentially zero kinetic energy. The Gaussian fitted functions of the intact cation and the argon ion are shown with full width half maximum of 0.19 eV and 0.09 eV, respectively. It is anticipated that the slow intact cation corresponds to the intact cation from dissociative ionization (equation (1.1) in Chapter 1) that is known from previous studies.[27-28, 53] The available energy (14.5 ± 0.2 eV), schematic shown in

Figure 3.3, which is the difference between the photon energy (23.4 eV) and dissociative ionization energy of 8.9 ± 0.2 eV that is obtained by previous investigation[28] is primarily distributed to the kinetic energy of the light electron, 14.5 ± 0.2 eV, which was measured by photoelectron spectroscopy in previous investigations.[27-28] The cation and neutral anion that result from the dissociative ionization have little or no kinetic energy, with a broader distribution than Ar ions, which is in good agreement with previous studies.[27-28] The maximum translational energy observed for this slow intact cation is about 0.4 eV. The angular distribution of the slow intact cation has an isotropic distribution that is indicative of an intact cation arising from a slow post-ionization fragmentation of a larger rotating cation, i.e. the ion-pair cation, $([Emim]^+[Tf_2N]^-)^+$.

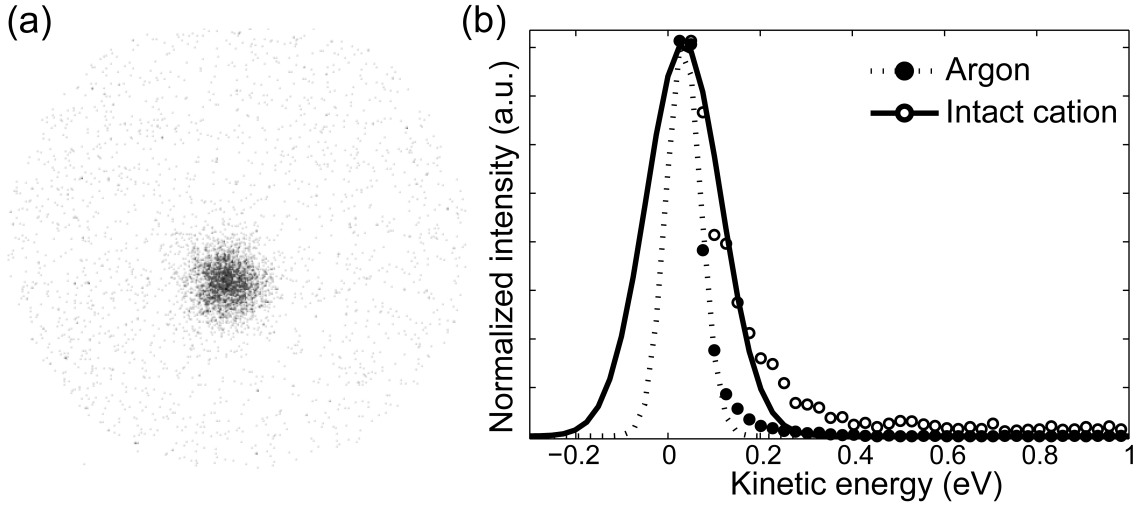

Figure 3.4. Photoionization of ionic liquid, $[Emim]^+[Tf_2N]^-$, at photon energy of 23.4 eV and (a) its velocity map ion image of intact cation, $Emim^+$, showing isotropic angular distribution at low focusing (424 V) condition and (b) the kinetic energy distribution of the intact cation (○) with its fitted Gaussian function of the intact cation (—) compared to the distribution of argon ion (●) with its fitted Gaussian function (---). Maximum translational energy of intact cation is about 0.4 eV.

To further explore the intact cation at higher kinetic energies, the ions were collected with high voltage focusing ion optics (875 V). The velocity map image of the intact cation produced by photoexcitation with the 15th harmonic (23.4 eV), shown in Figure 3.5(a), exhibits not only the slow ion that is from dissociative ionization in the center of the image, but also a fast ion at the outer ring of the image. The kinetic energy distribution is plotted in Figure 3.5(b) with a Gaussian fitted function in the solid line showing both the slow ion centered at 0 ± 0.2 eV and the fast ion above 10 eV. Note that the peak of the fast ion feature may not be observed in Figure 3.4, since the focusing conditions do not permit kinetic energies higher than 13 eV to be detected. This is important when analyzing the anion kinetic energies, to verify momentum complementarity. The slow ion is from dissociative ionization, as measured with low voltage focusing ion optics, whereas the fast ion is from photodissociation that has no photoelectron ejection. The fast intact cation with kinetic energy of more than 10 eV cannot result from an ion-pair fragmentation that yields F^- or CF_3^- ions or photoionization of neutral [Emim] molecule because in these cases most of the available energy will be distributed to the lighter fragment or the electron instead of the intact cation. The photofragment correlating with the fast intact cation

should be at least significantly heavier than the cation considering the total available energy. There is a possibility that this fast intact cation could be resulting from a cluster, but there is no indication of clusters in the effusive source at 453 K as previous studies.[27] In order for the cation to separate with such a large kinetic energy from either a neutral or anionic Tf_2N, nearly all of the excess energy needs to be deposited into the dissociative coordinate of the molecule by the photoexcited state. Although it cannot be entirely ruled out initially that the cation dissociates from a neutral Tf_2N species, it seems unlikely that electron ejection is occurring simultaneously with the high kinetic energy of the cation observed here, since the electron would normally take away a large amount of the excess energy. The only fragment that would fit momentum conservation and the large observed energy of the cation is, thus, the anion fragment. Hence in the experiments below, we seek a momentum correlation with the anion fragment.

Anions are investigated to find the counter fragment of the intact cation, and the intact anion is directly observed. There is no anion fragment other than the intact anion observed. The velocity map image of the intact anion is shown in Figure 3.6(a) with its kinetic energy distribution in Figure 3.6(b) at a photon energy of 23.4 eV. The kinetic energy is centered at 5.9 ± 0.5 eV with energy spread of 8 eV, full width half maximum of a Gaussian fitted function. This intact anion is from photodissociation of the neutral molecule and it is reasonable that it is the counter fragment of the intact cation. As the final momentum of the photodissociation products (cation + anion) should correlate with each other, an intact anion with a kinetic energy of 5.9 eV should correspond to an intact cation with a central kinetic energy of ca. 14.9 eV. However, data for the cation is only available up to 13 eV, and, in the initial assessment of its energy, the peak value of its kinetic energy was not available. Instead, if we assume that the intact cation has the same energy spread of ~ 8 eV as the anion, with a Gaussian function, and that the fast intact cation is not observed to higher kinetic energies due to the limited focusing, the data can be fit well by a fast intact cation that has a kinetic energy centered at 14.6 ± 0.7 eV, which is within the error of the momentum matched expected value of 14.9 eV. Therefore, the kinetic energy of the two ions suggests that the intact cation and the intact anion are a result of ion-pair dissociation, $Emim^+$ + Tf_2N^-, of the isolated neutral ion-pair.

A kinetic energy distribution of the intact anion centered at 6.1 ± 0.5 eV at photon energy of 20.3 eV is also shown in Figure 3.6(c) and it indicates little or no photon energy dependence in the kinetic energy of the intact anion. The velocity map images of the intact anion are also collected at a photon energy of 17.2 eV and 26.5 eV, data not shown here, and no kinetic energy shift upon photon energy change is observed. The distribution has a structureless broad spread of 8 eV in the kinetic energy and the shift due to photon energy change is not measurable. The results could be due to several steep repulsive (dissociative) potential energy curves above the ionization threshold that lead to the ion fragments. The excess kinetic energy can also lead to fragmentation of the intact cation imparting kinetic and internal energy to the fragments. Fragments of the intact cation, 1-ethylimidazolium and 1-methylimidazolium, have been observed (not shown here),[27] and their kinetic energy dependence on photon energy will be further investigated in the future giving more insight into the photodissociation mechanism. Also, given the large number of internal degrees of freedom, it may be possible that additional internal excitation is deposited into the fragments at higher photon energies. Until more specific dissociative potential surfaces are known, as well as the internal excitation, the broad kinetic energy distribution and the apparent lack of dependence on photon energy remain under investigation.

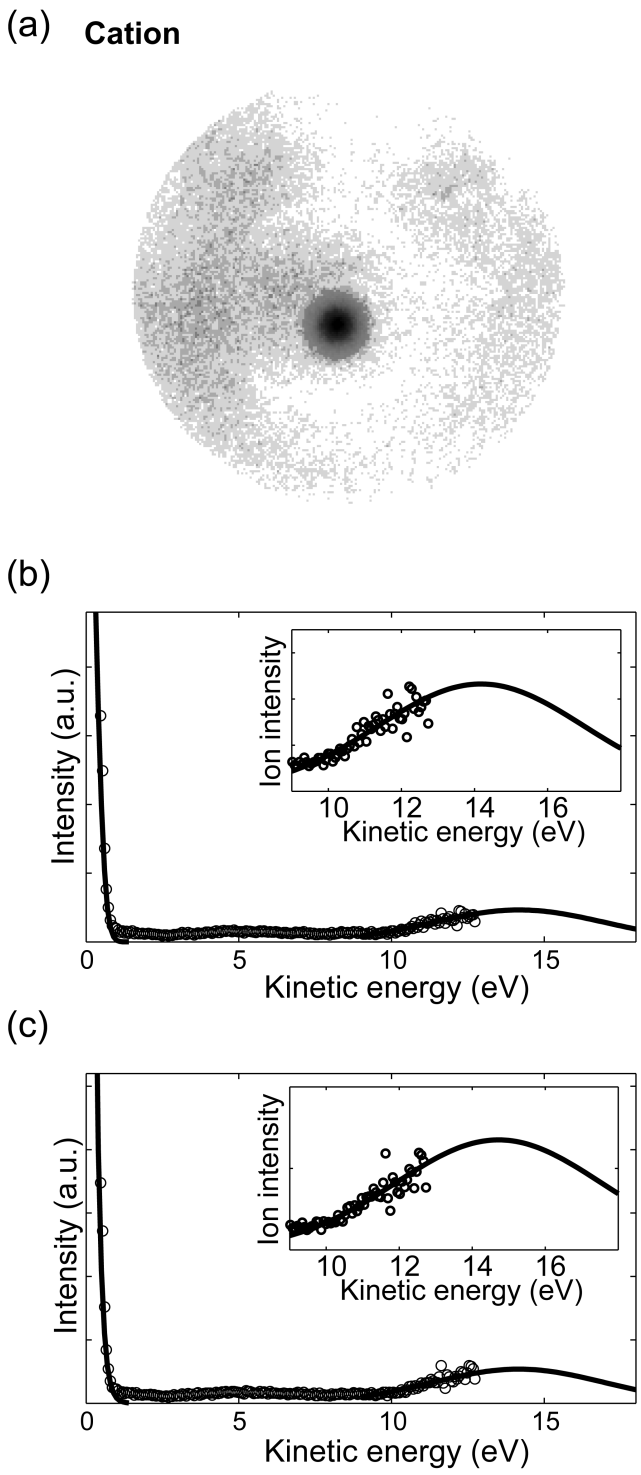

Figure 3.5. Photoionization of ionic liquid, $[Emim]^+[Tf_2N]^-$, at photon energy of 23.4 eV and (a) its velocity map ion image of intact cation, Emim+, at high focusing (875 V) condition. It shows an angular distribution with anisotropy parameter, $\beta = -0.55 \pm 0.07$, fitted in the energy range of 10 − 13 eV. Kinetic energy distribution of the intact cation at photon energy of (b) 23.4 eV and (c) 20.3 eV is shown and the higher kinetic energy in the range of 9 – 18 eV is shown in the inset of (b) and (c).

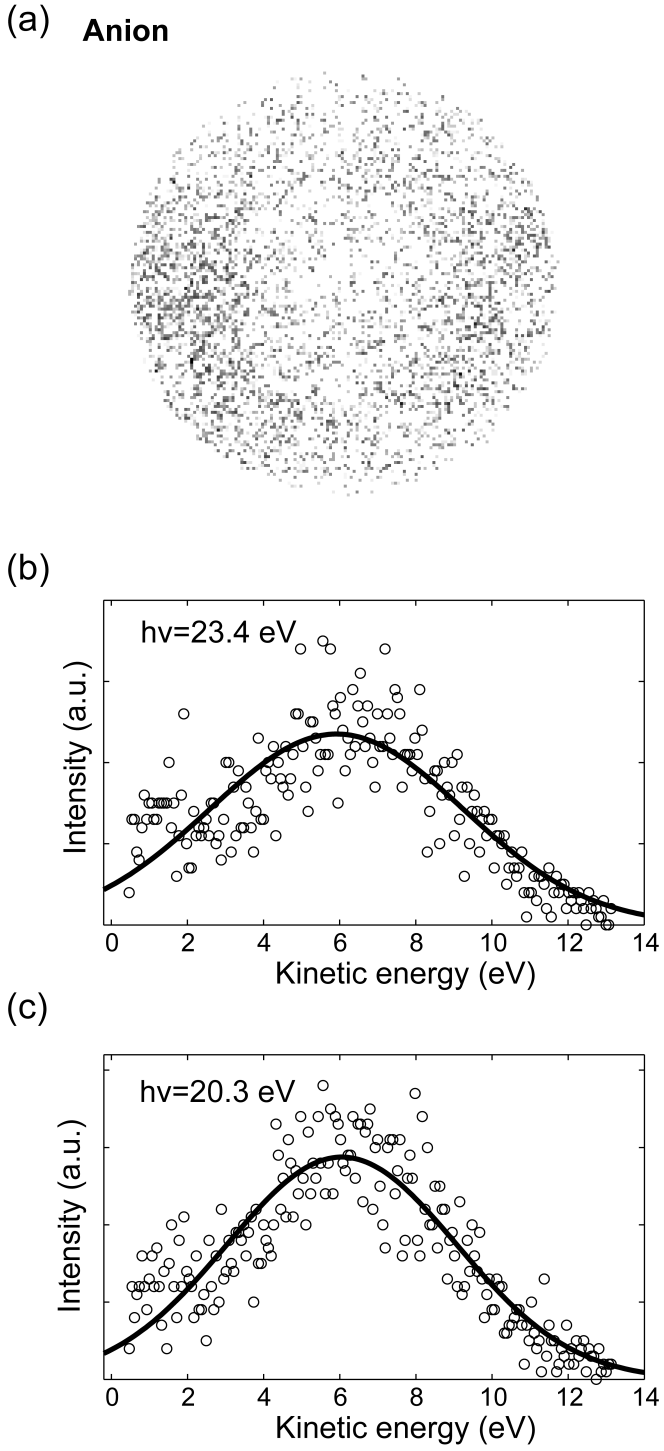

Figure 3.6. Photoionization of ionic liquid, $[Emim]^+[Tf_2N]^-$, at photon energy of 23.4 eV and (a) its velocity map ion image of intact anion, Tf_2N^-, at high focusing (−875 V) condition. It shows an angular distribution with anisotropy parameter, $\beta = -0.48 \pm 0.13$, fitted in the energy range of 3 − 6 eV. Kinetic energy distribution of the intact anion at photon energy of (b) 23.4 eV and (c) 20.3 eV is shown.

The photon energy dependence of the intact cation is also investigated in the photon energy range of 17 – 26 eV. The kinetic energy distribution of the intact cation measured with a photon energy of 20.3 eV is shown in Figure 3.5(c), and it has the same features, slow and fast ions, as in the measurement with a photon energy of 23.4 eV in Figure 3.5(b). The slow intact cation has zero kinetic energy (0 ± 0.1 eV) regardless of the photon energy, as the available energy is distributed to the photoelectron. There is no obvious kinetic energy shift in the fast ions at this photon energy, nor at other photon energies of 17.2 eV (11th harmonic) and 26.5 eV (17th harmonic), data not shown here, although such a shift could probably not have been detected due to the limited detection of high kinetic energy and broad kinetic energy distribution.

The angular distributions for both the intact cation and intact anion, found from Figures 3.5(a) and 3.6(a), have anisotropy parameters of $\beta = -0.55 \pm 0.07$ and $\beta = -0.48 \pm 0.13$, respectively. The anisotropy parameters are fitted in the energy range of 10 − 13 eV for the intact cation and 3 − 6 eV for the intact anion. This nonlinear ionic liquid molecule does not exhibit a dipole moment strictly parallel or perpendicular to the breaking ionic bond. However, it shows moderate perpendicular contribution in the angular distributions versus the polarization direction of the EUV light, regardless of excitation energy. The similar anisotropy parameter, within the errors, for the two intact ions further suggests that the ions are produced from a two-body photodissociation channel, ion-pair dissociation. The result additionally indicates that transitions leading to this ion-pair dissociation have a dipole moment that is somewhat perpendicular to the cation−anion ionic bond, as suggested in Figure 3.3.

The branching ratio of the two competing dissociative ionization and ion-pair dissociation channels at a photon energy of 23.4 eV is 0.18 ± 0.02:0.82 ± 0.02 found from the ratio of the slow intact cation peak to the intact anion peak. Having fitted the fast intact cation with a Gaussian function as in Figure 3.5(b), the branching ratio between dissociative ionization and ion-pair dissociation is also determined from the ratio of the slow intact cation peak to the fitted fast intact cation peak, resulting in a ratio of 0.18 ± 0.03:0.82 ± 0.03 that is in excellent agreement with the one found using the intact anion peak. Branching ratios of dissociative ionization channel to ion-pair dissociation channel at other photon energies of 17.2, 20.3, 23.4, and 26.5 eV are 0.20 ± 0.02, 0.21 ± 0.02, 0.21 ± 0.02, and 0.25 ± 0.03 calculated using the intact anion peak, and 0.17 ± 0.03, 0.24 ± 0.03, 0.21 ± 0.03, and 0.27 ± 0.04 calculated using the fitted fast intact cation peak, respectively. The relative branching of the two channels, dissociative ionization/ion-pair dissociation, as a function of photon energy above the ionization threshold appears to increase as the photon energy increases. However, further investigation is necessary to confirm the branching ratio change of the two competing channels upon the photon energy change.

An ion image of the intact cation, $Emim^+$, from an ionic liquid, 1-ethyl-3-methylimidazolium tetrafluoroborate ($[Emim^+][BF_4^-]$), is collected at 23.4 eV. The kinetic energy distribution of the intact cation from $[Emim^+][BF_4^-]$ is shown in blue in Figure 3.7 and is compared to the one from $[Emim^+][Tf_2N^-]$. It reveals that a fast intact cation is not produced from the ion pair dissociation upon photoexcitation, but only a slow intact cation is produced from dissociative ionization in $[Emim^+][BF_4^-]$, unlike in $[Emim^+][Tf_2N^-]$ where both fast and slow intact cations are observed. The anion plays a role in the branching ratio of the two competing channels, ion pair dissociation and dissociative ionization.

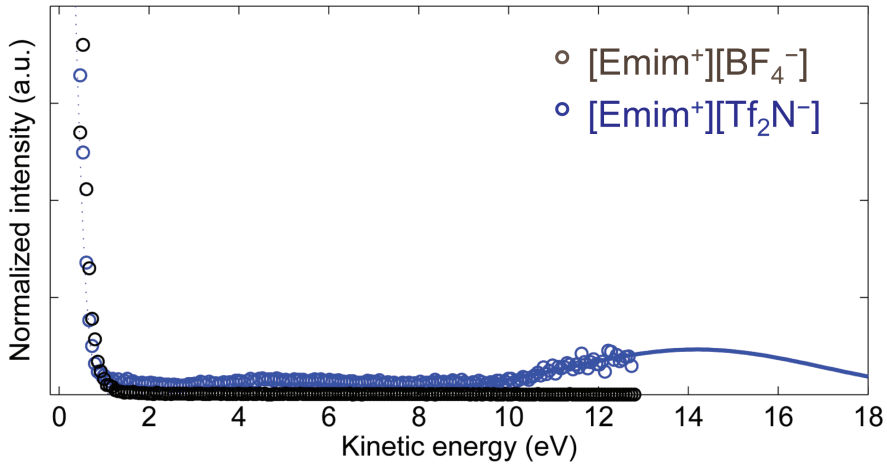

Figure 3.7. Photoionization of ionic liquids, $[Emim]^+[BF_4]^-$ and $[Emim]^+[Tf_2N]^-$, at photon energy of 23.4 eV. The kinetic energy distribution of intact cation, $Emim^+$, at high focusing (+875 V) condition is shown for $[Emim]^+[BF_4]^-$ in blue and for $[Emim]^+[Tf_2N]^-$ in black.

3.4 Conclusions

Photoexcitation of an ionic liquid vapor composed of ion-pairs, $[Emim]^+[Tf_2N]^-$, using extreme ultraviolet light in the range of 17 − 26 eV is probed with velocity map ion imaging for the first time. It is shown that photoexcitation of the ion-pair leads to dissociative ionization producing the intact cation with zero kinetic energy, which is in good agreement with previous studies, as well as to photodissociation producing a fast intact cation and a fast intact anion. The intact anion with kinetic energy of ca. 6 eV is observed with a complementary momentum that correlates with the intact cation with a kinetic energy above ca. 10 eV, indicating that the intact ions are produced from two-body dissociation of the neutral ion-pair. Observation of this ion-pair dissociation provides direct evidence for isolated ion-pairs in the effusive beam, specifically neutral cation−anion 1:1 pairs. However, a photon energy dependence is not observed in the kinetic energies, possibly due to the broad energy spread resulting from the large number of internal degrees of freedom or multiple steep potential energy surfaces. We report branching ratios for the dissociative ionization and ion-pair dissociation channels to be 0.18:0.82 with anisotropy parameters of $\beta = -0.55$ (cation) and $\beta = -0.48$ (anion) for the ion-pair dissociation channel. The similar angular distribution of the intact anion and cation suggests that the transition leading to ion-pair dissociation has a dipole moment more perpendicular than parallel to the dissociating cation−anion bond. Given the detection of isolated ion-pairs in the gas phase and the identification of the photodissociation pathways in the 17 – 26 eV range, photodissociation of an ionic liquid can be further studied in greater depth and future studies are planned to study the photodissociation dynamics of intact ions from ion-pair dissociation in the femtosecond time domain.

▪ Acknowledgement

The authors are thankful to Dudley Herschbach; his inspiration and creativity gave us all the tools necessary to map new dynamics. The authors gratefully acknowledge funding from the US Air Force Office of Scientific Research for supporting CJK, and SRL (Grant No. FA9550-10-1- 0163). Certain equipment and support for SRL is provided by the Director, Office of Energy Research, Office of Basic Energy Sciences, Chemical Sciences Division of the U.S. Department of Energy under Contract No. DE-AC02- 05CH11231.

Chapter 4

Ultrafast Excited State Dynamics of an Imidazolium Based Ionic Liquid

Ultrafast excited state dynamics of isolated ion pairs of an ionic liquid (IL) vapor, 1-ethyl-3-methylimidazolium bromide ($[Emim]^+[Br]^-$), is studied using time-resolved photoion spectroscopy. An excited state prepared by two or three photon absorption of a pump pulse (403.6 nm) is probe using ultrafast extreme ultraviolet (EUV, 53.8 nm) light produced by high-order harmonic generation. The first time-resolved results of an ionic liquid that are probed along ultrafast timescales using these EUV photons are illustrated. The intact cation and some of the other alkyl-loss fragments are monitored after single photon ionization. The simultaneous depletion of the intact cation that represents the isolated ion pairs and appearance of alkyl-loss fragments suggests several possibilities, involvement of the π^* excited state or reaction dynamics induced by the vibrationally excited molecules.

4.1 Introduction

Ionic liquids (ILs) are ambient temperature molten salts consisting of an asymmetric organic cation and a halogenated anion or an organic anion.[1] Coulombic forces between the ions are the dominant interaction in ILs, which contribute to their unique properties such as low volatility, high thermal stability, electrical conductivity, and solvation ability.[6, 75] There has been a substantial number of studies of ionic liquids in many fields and for uses as electrolytes,[16, 18, 76] fuel cells,[77-79] and rocket propellants[20, 23-24, 51, 80] because of their distinctive properties. For their specific usage in various applications, the properties of ILs can be tuned by designing them accordingly based on cation−anion (C^+-A^-) pairs with a vast number (10^{18}) of possible combinations.[21] The low electric potential between the cation and the anion, resulting from bulky and freely rotating alkyl groups in the cation,[75] which effectively prevents the close approach of the neighboring ions, may primarily determine the electronic and nuclear structure. It is valuable to understand the fundamental characteristics, such as basic photophysics of isolated ion-pairs, in order to facilitate designing IL molecules.

Recent works[29, 34-35, 52-54, 56-58, 81] show that isolated ion-pairs can be prepared in the gas phase from bulk ionic liquid even with their extremely low vapor pressure. In 2006, it was demonstrated by Earle et al., that many ionic liquids can be vaporized and even distilled in vacuum without decomposition.[26] More recent studies also show that ILs form neutral ion pairs upon evaporation, using various methods such as electron ionization,[29] single photon ionization,[27-28, 81] and field ionization,[54] etc. Upon ionization of ILs, although the cation (C^+) is

usually observed due to dissociative ionization, a molecular ion (CA^+) has been observed with field ionization[54] and soft photoionization,[81] which gives direct evidence for the isolated ion pair in the gas phase. While thermodynamic properties of these ion pairs are being extensively studied, the electronic and structural information remains more limited, although such information should be valuable for various fields, such as photo-induced chemistry and for organic fuel applications. Previous work has been conducted in our group on the valence electronic structure,[27] the photoexcitation,[82] and the photoionization[28] of imidazolium-based ILs. Here we initiate a first investigation of an ultrafast spectroscopic study on photodissociation dynamics of an ionic liquid, 1-ethyl-3-methylimidazolium bromide ($[Emim]^+[Br]^-$); the molecular structure is shown in Figure 4.1.

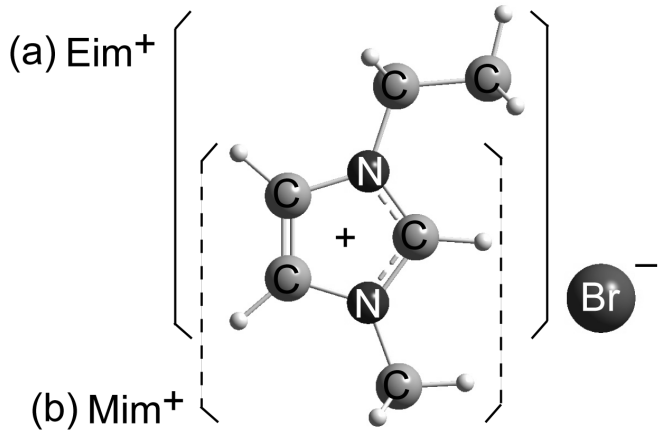

Figure 4.1. Molecular structure of 1-ethyl-3-methylimidazolium ($[Emim]^+$) bromide (Br^-), $[Emim]^+[Br]^-$ and its alkyl-loss-cation fragments, (a) 1-ethylimidazoium (Eim^+) in the solid parentheses and (b) 1-methylimidazolium (Mim^+) in dotted parentheses.

Time-resolved photoion mass spectrometry (TR−MS) utilizing pump probe techniques has proven to be powerful tool for probing excited state and photodissociation dynamics of molecules and clusters. Especially, a high-order harmonic probe, i.e. ultrafast extreme ultraviolet (EUV) light pulses with photon energies generally above 20 eV, allow us to universally monitor pump-induced excited state dynamics by single photon ionization or to acquire photoelectron spectra. In the present work, we focus on illustrating the excited state dynamics of isolated ion pairs initiated by visible light multiphoton absorption based on a first attempt with ultrafast measurements to obtain the major photofragments. We describe the phenomenological time dependencies of several dissociative products, specifically the intact cation and its alkyl-loss fragments, observed in the time-resolved photoion measurements of the excited $[Emim]^+[Br]^-$, and suggest possible excited state pathways.

4.2 Experimental Methods

Excited state dynamics of ILs are studied using a pump probe technique by exciting the isolated ion-pair with two or three photons of a 400 nm pulse, which initiates the dynamics, followed by a high harmonic probe pulse, which ionizes and dissociatively ionizes the excited state and any fragments. The photoions produced from single photon ionization by the EUV probe pulse are monitored on femtosecond time scales by changing the delay time of the pump and probe pulses.

The experimental setup, previously described in detail,[27, 39] consists of a 2.2 mJ, 80 fs Ti:sapphire-pulsed laser system operating at 1 kHz repetition rate to generate high-order harmonics of the 805 nm fundamental radiation by focusing 70% of the beam into an argon gas cell. For the experiments here, the 15th harmonic (53.8 nm, 23.04 eV) is selected as a probe pulse and refocused by grazing incidence optics; a spherical grating in zeroth order and a toroidal mirror in first order direct the beam to the interaction region. The remaining 30% of the laser light is frequency doubled in a beta barium borate (BBO) crystal to produce up to 160 μJ pulses at 403.6 nm, and these pump pulses are subsequently focused and overlapped with the harmonic beam at a 1.5° angle in the interaction region. At the interaction region, an effusive beam of ionic liquid vapor intersects the laser beams at a right angle.

The ionic liquid vapor source, previously described,[27] uses a pyrex reservoir inside an aluminum oven heated by four home-built resistive heating cartridges. Thermal decomposition is minimized by using a pyrex interior for the vapor source and by reducing the distance to the exit of the oven, which minimizes molecular collisions. The IL sample, $[Emim]^+[Br]^-$ (≥97% purity), was purchased from Fluka and kept under high vacuum (~2 x 10^{-8} Torr; 2.7 x 10^{-6} Pa) at 323 K temperature before experiments for more than 12 h to remove volatile impurities such as water. The IL vapor is emitted as an effusive beam at an oven temperature of 448 K, and the beam is skimmed by a ϕ1 mm skimmer before it intersects the laser beams that dissociate and ionize the molecule to produce photoions. Positive ions produced by photoionization of the IL vapor are analyzed using a ~1.3 m long Wiley-McLaren type time-of-flight (TOF) mass spectrometer with 1 amu/q mass over charge resolution (at mass ~130 amu/q). For the electron binding energy measurement, the energy of the emitted photoelectrons is measured using a magnetic-bottle TOF spectrometer with typical photoelectron energy resolution of ~4% that is used in place of the mass spectrometer. In order to improve the TOF electron spectral resolution, the electrons are decelerated by 3.15 V at the entrance of the flight tube. The TOF measurement is calibrated using the mass spectra of air and xenon isotopes ionized by the 15th harmonic or using the photoelectron spectra of neon ionized by the 15th harmonic. Mass spectra are recorded as a function of the delay time between the 53.8 nm EUV probe pulse and the 403.6 nm pump pulse, which is controlled by a variable delay stage. For experiments here, because of signal limitations, only 8 time steps with 100 fs intervals are recorded for mass spectra with 160 x 10^6 laser pulses/step. The background spectrum, due to ionization of the ionic liquid molecules by the 53.8 nm probe pulse alone, is subtracted on a pulse-to-pulse basis by blocking every other pump pulse with a chopper that is synchronized to the laser repetition rate. The actively subtracted pump-probe spectrum (ΔMS) is accumulated on a multichannel scaler and simultaneously a total TOF spectrum is recorded on a different multichannel scaler.

For the calculated photoelectron spectrum of $[Emim]^+[Br]^-$, the ab initio calculation was performed using the Gaussian 03W program package. The geometry was first preoptimized at the HF level of theory. Final optimization and energy calculations were performed at the B3LYP 6-31+G(d,p) level of theory. The energy minimum is found with a residual root mean square (RMS) force of 0.00008 eV/Å. The density of state (DOS) is calculated using the Gaussian 03W program package and plotted using the GaussSum. Assuming uniform cross sections per eigenstate and a Gaussian broadening of 0.8 eV, calculated eigenstates are convoluted to a DOS comparable to the experimental spectra.

4.3 Results and Discussion

The photoelectron binding energy spectrum obtained for $[Emim]^+[Br]^-$ vapor with the 15th high harmonic (23.1 eV) is shown by the solid line with circles in Figure 4.2. The measured spectrum is in good agreement with the calculated density of state spectrum of the $[Emim]^+[Br]^-$ cation-anion complex shown by the solid line in Figure 4.2. The calculated spectrum is shifted by +0.91 eV with respect to the experimental results to match the highest occupied molecular orbital (HOMO) peak in the spectrum. Both the relative peak positions and intensities of the measured and calculated spectra are in good agreement. The photoelectron binding energy of gas phase $[Emim]^+[Br]^-$ is assessed to be 9.3 ± 0.1 eV. This ionization potential corresponds to the removal of an electron from the valence orbital of the anion, bromide, corresponding to the previously suggested[27-28, 82] dissociative ionization mechanism. The observed photoion mass spectrum (Figure 4.3(a)) has a small contribution of intact cation, which also suggests that we have an isolated ion pair of $[Emim]^+[Br]^-$ in the gas phase and upon 53.8 nm irradiation the overall neutral vapor species undergoes dissociative ionization resulting in alkyl-loss fragments such as 1-ethylimidazolium (Eim^+), and 1-methylimidazolium (Mim^+), shown in solid and dotted parantheses in Figure 4.1, respectively.

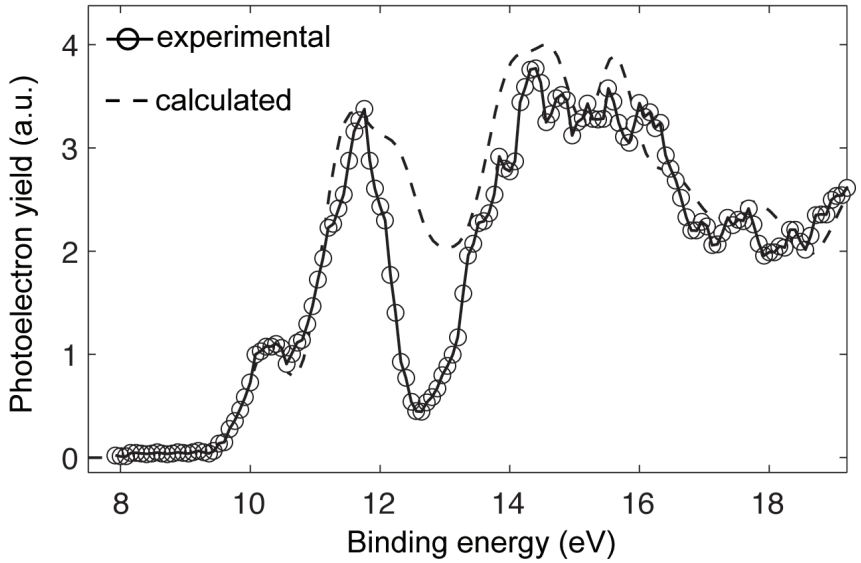

Figure 4.2. Photoelectron spectra of $[Emim]^+[Br]^-$ vapor (circles with solid black line) compared to density of states calculation (dotted black line)

(a)

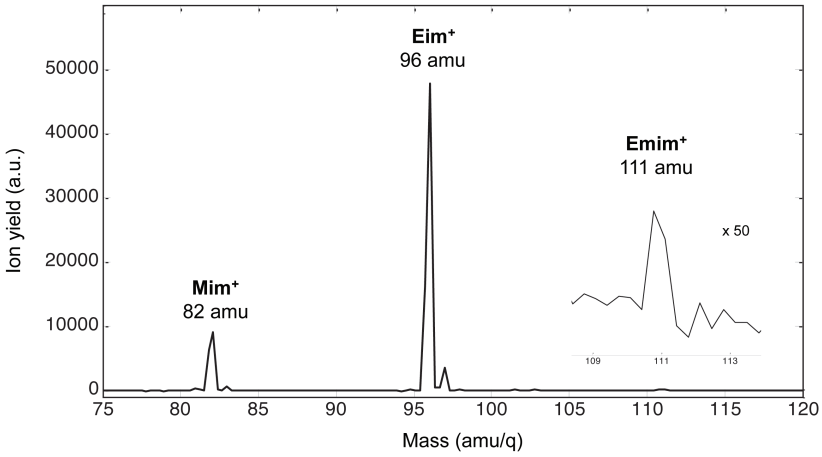

(b)

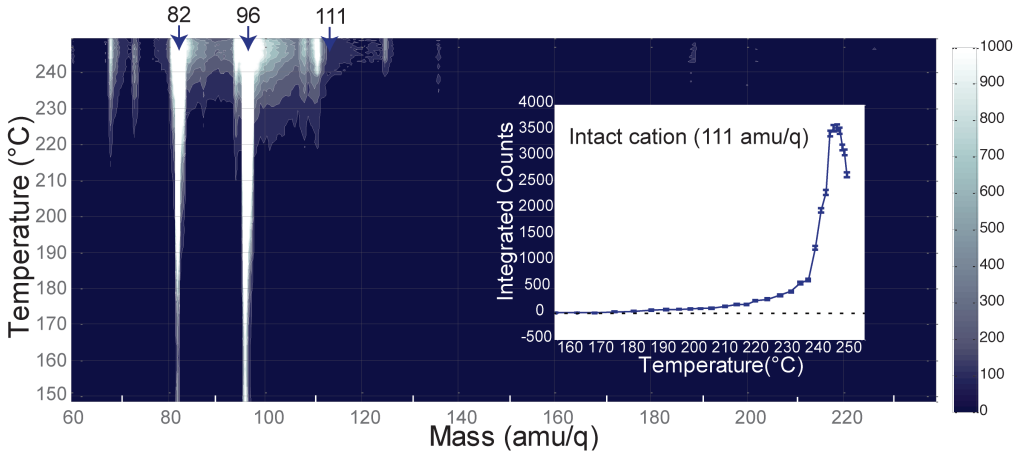

Figure 4.3. Mass spectrum of $[Emim]^+[Br]^-$ at 53.8 nm obtained at (a) 443 K (175 °C) showing the small contribution of the intact cation ($Emim^+$, 111 amu/q) and mostly the alkyl-loss fragments, Eim^+ and Mim^+, and obtained (b) as a function of temperature, indicating thermal decomposition. Temperature dependence of the intact cation is shown in the inset as it is not easily visible in the 2D plot due to the low signal.

However, these cation fragments, Eim^+ and Mim^+, are not only dissociative ionization fragments of "cold" $[Emim]^+[Br]^-$ at 53.8 nm but also are enhanced with temperature and suggested to be thermal decomposition products presumably through alkyl abstraction via an S_N2 type mechanism.[74] The thermal decomposition products, neutral Eim and Mim, are produced in the vapor and are probed by single photon ionization at 53.8 nm. In $[Emim]^+[Br]^-$, thermal vaporization competes with thermal decomposition upon heating and it is shown that decomposition can dominate in some experimental conditions.[74] A temperature dependence of the fragments is shown in Figure 4.3(b). When the temperature is increased more fragments including methyl bromide (94 amu and 96 amu) and ethyl bromide (108 amu and 110 amu) are

observed, an indication of thermal decomposition, in good agreement with the previous study.[74] At low temperature, the intact cation that represents the isolated ion pair is detected here while the previous experiments were lacking evidence of the intact cation. In order to reduce thermal decomposition in this study, the region of the effusive beam where the ionic liquid is in contact with the walls was completely constructed with a pyrex interior and short travel distance to the exit of the oven. The temperature dependence of the intact cation, shown in Figure 4.3(b) inset, indicates thermal vaporization at low temperature and thermal decomposition competing as temperature increases. The fragments, Eim^+ (96 amu) and Mim^+ (82 amu), appear in the spectrum with same temperature dependence as the intact cation, which suggests that the fragments are mostly produced by dissociative ionization and not only by thermal decomposition followed by ionization of fragments at least nearby the vaporization onset temperature. Therefore, it is assumed that near the onset of the vaporization temperature isolated ion pairs are produced in the gas phase with some amount of thermal decomposition.

Even though there is evidence of isolated ion-pairs, which are the intact cation signal, as well as the electronic structure, the possibility of neutral fragments produced upon thermal decomposition cannot be neglected. In the time-resolved measurements, therefore, the temperature of the source is held constant keeping the amount of neutral fragments, Eim^0 and Mim^0, vaporized upon thermal decomposition constant during the measurements. The transient spectra are derived by subtraction of the signal of pump+probe minus the probe only, thus eliminating the process due to the probe alone. As the baseline of the produced Eim^+ and Mim^+ is fixed, the observed time-resolved signal should be due to the electronic excitation or the internal excitation. The time-resolved signal of Eim^+ and Mim^+ should have little or no delay time dependence unless the dynamics are inititated by the 400 nm excitation of either $[Emim]^+[Br]^-$ or neutral Eim^0 and Mim^0 fragments. It is assumed in this study that the thermal decomposition is minimal and that the dynamics of the neutral fragments are negligible, therefore the time resolved Eim^+ and Mim^+ signal is due to the dynamics of $[Emim]^+[Br]^-$. The time resolved $Emim^+$ signal is most likely from the isolated ion pair since there is no evidence of $Emim^+$ as a decomposition product.[74]

More spectroscopic information on photodissociation of the vaporized ion-pair is obtained using time-resolved mass spectrometry. Mainly, time resolved signals of $Emim^+$ (111 amu/q), Eim^+ (96 amu/q), and Mim^+ (82 amu/q) are measured as shown in Figure 4.4. In the transient spectra negative amplitude peaks correspond to depletion features and the positive signals correspond to the production of fragments. In Figure 4.4(a), depletion of the intact cation ($Emim^+$) is observed with a fast recovery that is within 200 fs. Also appearance of the (b) Eim^+ and (c) Mim^+ fragment is observed at delay times of 50 ± 50 fs and 150 ± 50 fs, respectively. Both of these signals increase near time zero and decrease at longer delay times. The results have a total signal to noise ratio of ca. 5 for both the Eim^+ and Mim^+ measurements.

The general conclusion from these observations is that the isolated ion pair is electronically or highly vibrationally excited resulting in depletion of the intact cation, and the excited ion pair, subjected to the probe ionization, promotes the production of alkyl-loss fragments, Eim^+ and Mim^+. There are several possible ways that could lead to the results and two possibilities (electronic excitation and high vibrational internal excitation) are discussed in the following paragraphs.

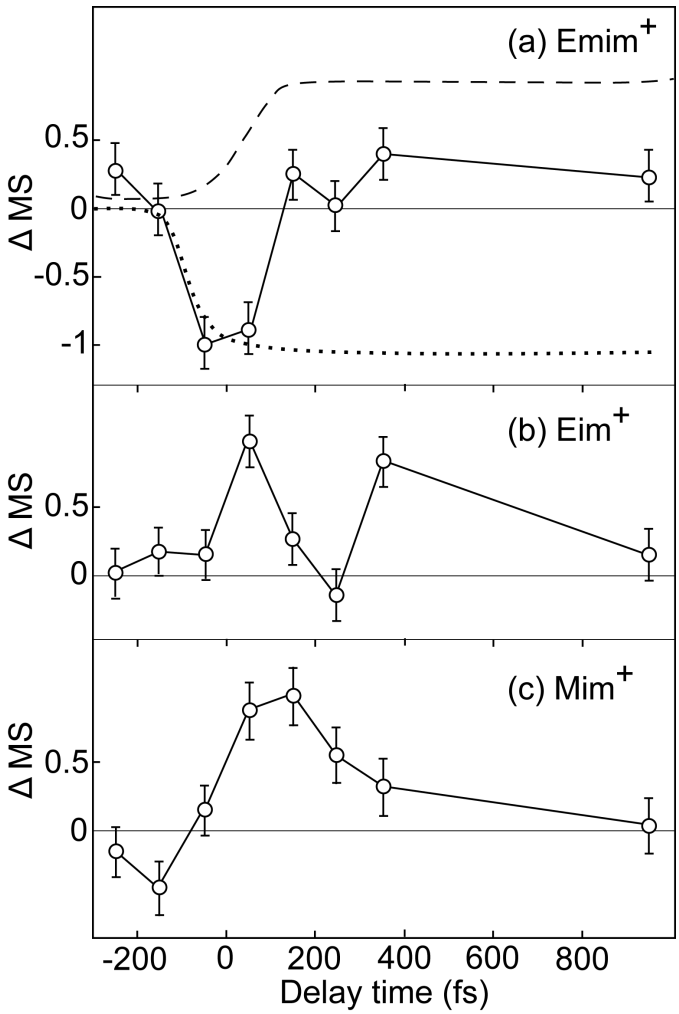

Figure 4.4. Time dependence of dissociative products observed by photoion (ΔMS) measurements along the femtosecond timescale. (a) Momentary depletion of intact cation, $[Emim]^+$ at 111 amu/q, is observed. Schematic of one possible scenario leading to this momentary depletion is drawn on top of the raw data in the dotted line indicating ground state depletion and in the dashed line indicating rise of additional intact cations, where sum of the depletion and rise will result in the momentary depletion as observed. Rise of the alkyl-loss fragments, (b) Eim^+ at 96 amu/q and (c) Mim^+ at 82 amu/q, are shown with appearances at 50 ± 50 fs and 150 ± 50 fs, respectively. A recurrence of Eim^+ at a delay time of 350 ± 50 fs is observed suggesting possible wave packet dynamics.

First of all, the ionic liquid, $[Emim]^+[Br]^-$, can be electronically excited by multiple photons of the second harmonic pump pulse. An excited state with a short lifetime will result in a temporary depletion of intact cation and a transient appearance of alkyl-loss fragments if probing of the excited ion-pair increases dissociative ionization. A possible electronically excited state is the π* excited state, which is accessible by two photons of second harmonic pump pulse. However, the imidazolium based ionic liquid, $[Emim][Tf_2N]$, has fluorescence lifetime components of 350–500 ps (60%), 2.5–2.8 ns (25 %), and 9.4–9.6 ns (15 %),[83] which are all long compared to the observed timescale of 200 fs. The π* excited state of imidazole derivatives in solution are known

to have a long lifetime (>1 ns) as well.[84] It could be that the π* excited state has a short lifetime in the gas phase or especially in the bromide ionic liquid system, but this seems unlikely.

An excited state with a long lifetime will result in a long lasting depletion feature as schematically shown in the dotted line in Figure 4.4(a). If ionization of the excited ion-pair increases dissociative ionization or an other pathway to produce the intact cation, a 50 fs delay in the appearance of the additional intact cation (dashed line in Figure 4.4(a)) on top of the long lasting depletion might result in a temporary depletion. It might look like the depletion completely recovers because the amplitude of the additional intact cation is roughly the same as the amplitude of the depletion. The cause of such a delay is uncertain, but could involve a transient short-lived state or configuration. Alkyl-loss fragments should have a similar or long lasting depletion feature as they are dissociative ionization products of the isolated ion-pair as well, but the signal of Eim^+ and Mim^+ is temporally positive instead of negative indicating that the amplitude of additional alkyl-loss fragments is larger than the depletion near time zero. This means that alkyl-loss fragments are produced more when probing the π* excited state near time zero. If the cross sections of the photodissociation channels are increased at the inner turning point on the π* excited state, but decreased at the outer turning point, a wave packet dynamics could be observed and might explain the increased signal near time zero. The recurrence of Eim^+ at a delay time of 350 ± 50 fs might indicate this wave packet dynamics, but the evidence is too little to confirm such a hypothesis.

Another possibility to explain the general conclusion is that the ionic liquid, $[Emim]^+[Br]^-$, can be internally excited to high vibrational states by multiphoton absorption. A short-lived internally excited state, upon 53.8 nm ionization, can yield more alkyl-loss fragments of Eim^+ and Mim^+. In general, the higher internal energy acts like raising the temperature, so greater fragmentation occurs. As shown in Figure 4.3(b), there is more fragmentation as temperature increases upon ionization. A short-lived internally "hot" ion pair will fragment more when ionized as the temperature increases. This could result in temporary depletion of the intact cation and a rise of the Eim^+ and Mim^+ due to probing of a presumably short-lived internally excited state.

Not only the internally "hot" ion pair can fragment more by dissociative ionization to produce Eim^+ and Mim^+, but also there can be more neutral Eim^0 and Mim^0 fragments produced by decomposition of $[Emim]^+[Br]^-$. The bending mode of 1-N−ethyl or 2-N−methyl can be active for highly vibrationally excited states and this will enhance the reactivity of bromide to form ethyl bromide or methyl bromide by an S_N2 mechanism producing neutral Mim^0 or Eim^0 fragments. In this case, the temporal rise of Mim^+ and Eim^+ can be from neutral Mim^0 or Eim^0 fragments followed by 53.8 nm ionization. As the isolated ion pair is decomposed to these neutral fragments upon vibrationally assisted reaction, the intact cation signal can be momentarily negative at the same time as alkyl-loss fragments are temporally produced.

Additional experiments are required to determine whether the electronically excited state is initiated alone or internal conversion to high vibrational state has occurred at a short time. A simpler picture of the ultrafast dynamics can be obtained by using a single photon excitation to initiate the excited state dynamics instead of a multiphoton excitation. Future investigations on the dynamics of an ionic liquid, such as $[Emim]^+[BF_4]^-$, which has less thermal decomposition

but with a strong local cation−anion interaction that is only slightly weaker than $[Emim]^+[Br]^-$ could show affirmative proof of whether the dynamics is from the isolated ion pairs or decomposition products, by comparing the dynamics of $[Emim]^+[Br]^-$ and $[Emim]^+[BF_4]^-$.

4.4 Conclusions

Excited state of ionic liquid, $[Emim]^+[Br]^-$, initiated with two or three photons of 403.6 nm light, is probed with ultrafast extreme ultraviolet (53.8 nm) single photon ionization. Time resolved photoion spectra show simultaneously the depletion of intact cation, $Emim^+$, which is related to the depletion of the ground state ion pair, as well as the appearances of dissociative products, Eim^+ and Mim^+. We suggest among several possibilities that the π^* excited state or a highly vibrationally excited state is prepared by multiphoton 403.6 nm excitation and that the ionization of the excited state results in more of the alkyl-loss fragments. Given the potential dynamics upon multiphoton absorption of the visible light, future studies are planned to investigate the dynamics with single photon absorption, to obtain a more clear interpretation, and to investigate other ionic liquids for comparison.

- **Acknowledgement**

The authors gratefully acknowledge funding from the US Air Force Office of Scientific Research for supporting CJK, and SRL (Grant No. FA9550-10-1- 0163). Certain equipment and support for SRL is provided by the Director, Office of Energy Research, Office of Basic Energy Sciences, Chemical Sciences Division of the U.S. Department of Energy under Contract No. DE-AC02- 05CH11231.

Chapter 5

Thermal Properties of Ionic Liquids

Thermally stable ionic liquids were first investigated with the synchrotron in collaboration with Steven Chambreau and Ghanshyam (Gammy) Vaghjiani of Edwards Air Force Research Laboratory to learn about their vaporization process and their tunable-wavelength dissociative ionization thresholds. Threshold measurements[28] of isolated ion pairs that are not discussed in this chapter reveal shifts in ionization energies as changes are made to the cation and anion pairings. Increased electronegativity of the anion shifts the ionization threshold higher, whereas bulkier cations shift the binding energy lower. Here, measurements of heats of vaporization (5.1) and observation of direct isolated ion-pairs upon vaporization (5.2) using ionization threshold measurements are discussed. New experiments were also initiated to study the thermal decomposition of hypergolic ionic liquids. The goal of these experiments was to learn about the initial stages of decomposition to elucidate the mechanisms involved in the properties of hypergolicity. The two-stage oven shown in Figure 2.4 was used to generate ionic liquid vapor in the first stage and induce thermal decomposition in the second stage. The thermal decomposition mechanism of an ionic liquid is discussed in the third section (5.3).

5.1 Heats of vaporization of room temperature ionic liquids by tunable vacuum ultraviolet photoionization

The heats of vaporization of the room temperature ionic liquids (RTILs) *N*-butyl-*N*-methylpyrrolidinium bistrifluorosulfonylimide, *N*-butyl-*N*-methylpyrrolidinium dicyanamide, and 1-butyl-3-methylimidazolium dicyanamide are determined using a heated effusive vapor source in conjunction with single photon ionization by a tunable vacuum ultraviolet synchrotron source. The relative gas phase ionic liquid vapor densities in the effusive beam are monitored by clearly distinguished dissociative photoionization processes via a time-of-flight mass spectrometer at a tunable vacuum ultraviolet beamline 9.0.2.3 (Chemical Dynamics Beamline) at the Advanced Light Source synchrotron facility. Resulting in relatively few assumptions, through the analysis of both parent cations and fragment cations, the heat of vaporization of *N*-butyl-*N*-methylpyrrolidinium bistrifluorosulfonylimide is determined to be $\Delta H_{vap}(298.15\ K) = 195 \pm 19\ kJ\ mol^{-1}$. The observed heats of vaporization of 1-butyl-3-methylimidazolium dicyanamide ($\Delta H_{vap}(298.15\ K) = 174 \pm 12\ kJ\ mol^{-1}$) and *N*-butyl-*N*-methylpyrrolidinium

dicyanamide (ΔH_{vap}(298.15 K) = 171 ± 12 kJ mol^{-1}) are consistent with reported experimental values using electron impact ionization. The tunable vacuum ultraviolet source has enabled accurate measurement of photoion appearance energies. These appearance energies are in good agreement with MP2 calculations for dissociative photoionization of the ion pair. These experimental heats of vaporization, photoion appearance energies, and *ab initio* calculations corroborate vaporization of these RTILs as intact cation-anion pairs.

5.1.1 Introduction

Ionic liquids are classified as ionic salts that have melting points at and below T = 100 °C. Room temperature ionic liquids (RTILs) are liquids under ambient conditions. RTILs represent a new class of "green" solvents that potentially can replace highly volatile organic solvents. Of specific interest to the aerospace community is the potential to replace hydrazine-based hypergolic fuels with RTIL-based propellants.[20, 23, 80] RTILs typically have large, multi-atom cations such as ammonium, pyrrolidinium, imidazolium, triazolium, and tetrazolium ions that have diffuse positive charge distributions and non-polar alkyl functional groups (Figure 5.1). The diffuse nature of the ionic charges, combined with the large effective cation-anion distance in RTILs results in relatively low lattice energies. By contrast, a typical ionic salt, NaCl (melting point T = 801 °C), has very localized charge distributions on each ion, and the separation between cation and anion is small, therefore a strong Coulombic attraction exists between sodium and chloride ions in the condensed phase. As a result, the lattice energy of NaCl is much higher than for RTILs, and the phase transition from ionic solid to liquid occurs at a much higher temperature in NaCl than for RTILs.

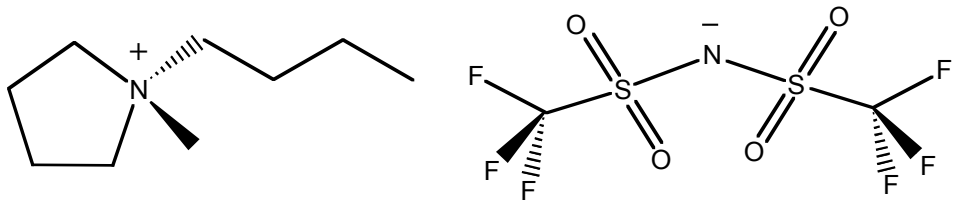

Figure 5.1. *N*-butyl-*N*-methylpyrrolidinium bistrifluorosulfonylimide $[pyrr_{14}]^+[NTf_2]^-$, a room temperature ionic liquid.

Due to their ionic nature, RTILs were originally thought to have essentially no vapor pressure. Recent studies of RTILs in vacuum have demonstrated that some RTILs can be distilled in vacuum with little thermal degradation,[26, 35, 85-86] as noted in more detail below. Transpiration and Knudsen methods[87] have also been applied to vaporize and recover RTIL condensates.[88-91] To evaluate the thermal stability of a compound, studies such as differential scanning calorimetry (DSC) and thermal gravimetric analysis (TGA) are typically carried out at atmospheric pressure.[89-90, 92-94] Recent TGA studies have shown that significant mass loss of RTILs can occur at temperatures well below the onset decomposition temperatures reported in DSC studies.[94] Such loss in mass could represent depletion through vaporization of intact RTILs.

The ionic nature of RTILs may lead to dramatically different vaporization mechanisms than for molecular liquids. For protic RTILs (having an H bound to a nitrogen in the cation ring),

typically a proton is transferred to the anion during vaporization and neutral species are formed:[35]

$$[AH]^+[B]^- \rightarrow A + BH \quad (5.1)$$

These neutrals can be volatilized, and upon condensation, the RTIL can be reformed by proton exchange to the weaker acid (the reverse of Reaction 5.1 above). The groundbreaking study by Earle et al.[26] demonstrated that when aprotic RTILs (having only alkyl groups bound to the cation ring nitrogens) are heated in a vacuum, recovery of the vapor produced the same RTIL with little or no degradation for several families of RTILs. Vaporization of mixtures of RTILs showed that one component was successfully enriched upon fractional distillation due to the differences in vapor pressure of one RTIL versus another.[35] The thermal stability of certain families of RTILs was attributed to the weak nucleophilicity (tendency to react with carbon) of the anion. Initially, the vaporization mechanism was proposed to be via cluster formation in the gas phase.[26] More recent studies using photoionization,[27] line of sight mass spectrometry,[29, 95] Fourier transform ion cyclotron resonance,[35, 85] and field desorption/ionization[54] mass spectrometric techniques suggest that vaporization of these thermally stable species is via neutral ion pair formation in the gas phase. However, aprotic RTILs with strongly nucleophilic anions can react when heated, and the recovery of pure RTIL by vacuum distillation may not be feasible.

Theoretical modeling of RTILs[96] has been of great interest in order to predict such important properties as heats of formation, heats of vaporization,[89, 97] melting and boiling points, viscosity, and thermal decomposition mechanisms.[98] Dynamics calculations have indicated that vaporization to produce an intact ion pair is energetically favored over ion cluster formation (multiple cation-anion ion pairs), where larger clusters have higher heats of vaporization.[55] The ionic nature of these liquids has made predicting these properties difficult and very few experimental data exist to confirm theoretical heats of formation and heats of vaporization values, quantities that are essential for evaluating RTIL performance as propellants.

The implication that RTILs evaporate as intact ion pairs is based on detection of the intact cation by mass spectrometry using photoionization or electron-impact ionization, as well as photoelectron spectroscopy and calculation. It is accepted that photoionization or electron impact ionization of the neutral ion pair, followed by dissociation, leads to a cation and a neutral and the cation is then detected by the mass spectrometer:

$$[A^+B]^- + h\nu \rightarrow [A^+B] + e^- \rightarrow A^+ + B + e^- \quad (5.2)$$

Direct detection of the ion pair has been elusive, most likely because of the use of relatively high energies of the ionizing photons (23.2 eV) or electrons (10-100 eV) versus the energy required to dissociate the ion pair:

$$[BMIM]^+[dca]^- \rightarrow BMIM^+ + dca^- \qquad \Delta H = 3.59 \text{ eV at } 298 \text{ K (G3MP2)}^{88} \quad (5.3)$$

where $[BMIM]^+[dca]^-$ is the RTIL 1-butyl-3-methylimidazolium dicyanamide. However, recent progress has been made towards direct detection of ion pairs.[99]

In this study, a first report is provided for determinations of the heats of vaporization of room temperature ionic liquids by tunable synchrotron photoionization detection. Several ionic liquids, N-butyl-N-methylpyrrolidinium bistrifluorosulfonylimide, $[pyrr_{14}]^+[NTf_2]^-$, N-butyl-N-methylpyrrolidinium dicyanamide, $[pyrr_{14}]^+[dca]^-$, and 1-butyl-3-methylimidazolium dicyanamide, $[BMIM]^+[dca]^-$, are studied by means of an effusive vapor source coupled to a vacuum ultraviolet photoionization time of flight mass spectrometer (PI-TOFMS). An analysis of the strengths of the photoionization method is made, which include the ability to study the heats of vaporization of the ionic liquid molecules at the tunable thresholds for dissociative photoionization, good comparisons between the ΔH_{vap} results from several fragment masses, and an ability to assess the temperature dependence of the photoionization cross sections. Furthermore, the comparison of experimental photoion appearance energies with theory supports a dissociative photoionization mechanism. To our knowledge, this study is the first reported measurement of the heat of vaporization of $[pyrr_{14}]^+[NTf_2]^-$. The heats of vaporization of $[BMIM]^+[dca]^-$ and $[pyrr_{14}]^+[dca]^-$ obtained here are in reasonable agreement with previously reported experimental measurements.

5.1.2 Experimental Methods

The experiments were performed on the Chemical Dynamics Beamline, a tunable VUV beamline 9.0.2.3 at the Advanced Light Source in Berkeley, California. Product masses are detected as a function of vaporization temperature of the ionic liquid and tunable photoionization wavelength. The PI-TOFMS repeller was pulsed at 10 kHz and typically data was accumulated for 200,000 pulses per mass spectrum. For $[pyrr_{14}]^+[dca]^-$, 200,000 pulses were accumulated at 12.0 eV photon energy at 473 K, 483 K, and 493 K. For $[pyrr_{14}]^+[NTf_2]^-$ and $[BMIM]^+[dca]^-$, photoionization efficiency (PIE) data were acquired as the VUV photon energy was scanned from 8.0 to 15.0 eV in 0.2 eV steps (photon energy resolution was 0.025 eV). In this first study, PIE data were taken over a limited temperature range, at 468 K and 483 K for $[BMIM]^+[dca]^-$, and at 583 K and 613 K for $[pyrr_{14}]^+[NTf_2]^-$. In addition, data for $[pyrr_{14}]^+[NTf_2]^-$ were also accumulated at 12.6 eV and at 15.0 eV for longer signal averaging of 9 million pulses per spectrum at both 583 K and 613 K.

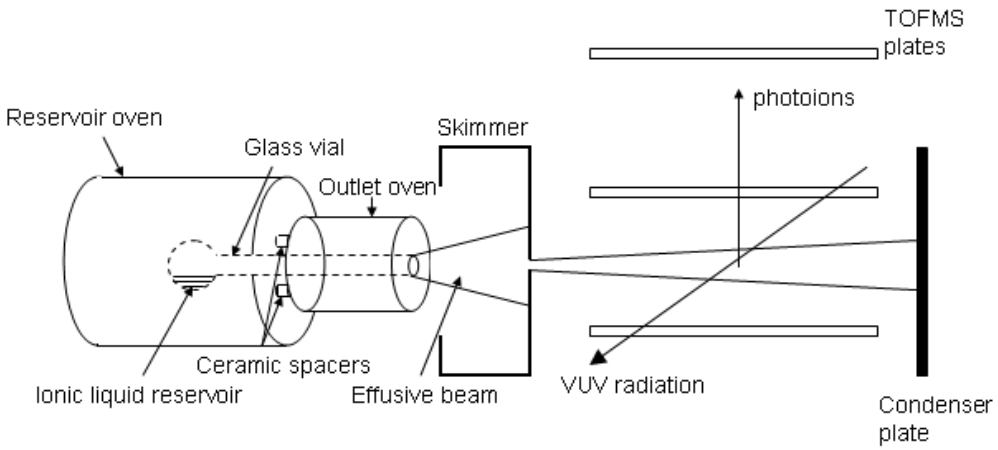

Figure 5.2. Ionic liquid effusive source.

The RTIL source is a modified version of a source described previously.[27] Briefly, the source uses a Pyrex reservoir that has a narrow outlet tube (Figure 5.2). Each region is surrounded by a machined aluminum block. Each block is heated separately by 4 cartridge heaters embedded evenly around the cell axis. The heaters in each region are controlled by separate power supplies (0-40 W per region), and thermal equilibrium within the source was reached before PIE curves were measured. The temperatures in each region are measured using previously calibrated type K thermocouples and, from the uniformity of the heated regions and thermocouple readings, the temperature values reported here are assessed to have an error of ±3 K. Although the temperatures of the reservoir and outlet regions can be controlled separately, for heat of vaporization determinations the temperature of the reservoir region was set to be equal to the outlet region. In order to examine pyrolysis of ion pairs in the gas phase, the temperature of the outlet region can be set at a higher temperature than the reservoir region, and pyrolysis experiments will be described in a future publication. The experimental temperatures were selected by performing differential scanning calorimetry (DSC) on the ionic liquids prior to the photoionization experiments. The temperatures were selected to be well below the decomposition temperatures of the ionic liquids to avoid pyrolysis.

The raw mass spectra were corrected for fluctuations in the power of the light source by monitoring the power at a VUV photodiode whose wavelength response curve had previously been characterized. The synchrotron was operating in top off mode and the ring current was kept constant at 500 mA. Low source temperature spectra were scaled and subtracted from the high temperature data to remove any background signals not due to the RTIL. Figure 5.3 shows a typical corrected mass spectrum. PIE curves were determined by integrating the peak areas of a given mass in each photon energy mass spectrum.

1-butyl-3-methylimidazolium dicyanamide (>98%) and N-butyl-N-methylpyrrolidinium dicyanamide (>99%) were purchased from EMD. N-butyl-N-methylpyrrolidinium bis-trifluorosulfonylimide (>98%) was purchased from Aldrich. In order to remove volatile impurities present in the sample, the RTIL samples were heated in high vacuum (base pressure ~10^{-6} Pascals) for 12 hours prior to the experiments as follows: $[pyrr_{14}]^+[NTf_2]^-$ at 453K, $[pyrr_{14}]^+[dca]^-$ at 378 K, and $[BMIM]^+[dca]^-$ at 358 K.

Ab initio calculations were performed using Gaussian 03W[100] at the HF 6-31+G(d,p) or B3LYP 6-31+G(d,p) level of theory to preoptimize geometries. Final optimization and energy calculations were performed at the MP2 6-31+G(d,p) level of theory using GAMESS.[101-102] Resulting MP2 energies at 0 K were corrected for unscaled zero-point vibrational energies. Based on previous calculations of RTIL ionization processes using HF 6-31+G(d,p), B3LYP 6-31+G(d,p), and MP2 6-31+G(d,p) levels of theory, MP2 6-31+G(d,p) was selected as the preferred method due to good agreement with experimental ionization potentials and ionization trends. The MP2 6-31+G(d,p) level of theory was assigned an uncertainty of ±0.1 eV based on our previous calculations.

5.1.3 Results and Discussion

A mass spectrum of $[pyrr_{14}]^+[NTf_2]^-$ taken at 613 K and 15.0 eV photon energy can be seen in Figure 5.3, and the PIE curves for mass 142 at 583 K and 613 K and mass 84 at 613 K are shown in Figure 5.4. Mass 142 represents the $[pyrr_{14}]^+$ parent cation of the ionic liquid ion pair in the gas phase (equation 5.2). The appearance of mass 84 is due to fragmentation of the internally hot $[pyrr_{14}]^+$ cation, which can be attributed to C_4H_{10} loss. From these curves, the appearance energies of the resulting intact cation and fragment cations can be determined, allowing insight into the energetics of ionization of the ion pair and possible ion fragmentation pathways. The observed appearance energies for masses 142 and 84 are 9.4 ± 0.2 and 10.0 ± 0.2 eV, respectively, which are in excellent agreement with their corresponding MP2 appearance energies of 9.2 ± 0.1 and 10.1 ± 0.1 eV. The thermal contribution due to the small temperature differences in these experiments (≤ 30 K) should only amount to a few millielectron volts at the temperatures involved, causing a shift to lower appearance energy due to hot bands that is smaller than the resolution of our experiment.

By comparing the intensities of mass 142 peaks, which are proportional to the number densities of the ion pair in the RTIL vapor,[95] at two known source temperatures T_1 and T_2 and applying the Clausius-Clapeyron equation, the heat of vaporization in this temperature range can be directly determined:

$$\Delta H_{vap} = -R\ln(I_2/I_1)[(T_1T_2)/(T_2-T_1)] \quad (5.4)$$

where I is the measured mass 142 peak intensity, and R is the gas constant. Over the temperature range of this experiment, the photoionization cross section at a given photon energy is considered to be constant. The branching fractions from the ionized ion pair to intact cation or cation fragments are considered to be constant as well.

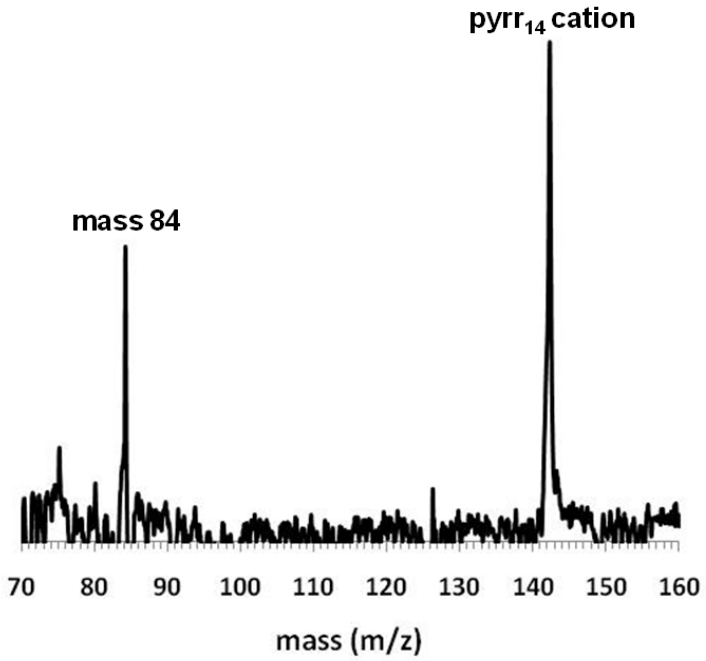

Figure 5.3. Mass spectrum of $[pyrr_{14}]^+[NTf_2]^-$ at 15.0 eV photon energy and source temperature of 613 K.

The heat of vaporization of $[pyrr_{14}]^+[NTf_2]^-$ was determined using equation 5.4 and the data in the following ways: (1) using the sum of the intensities of all the points along the mass 142 tunable wavelength PIE curve (36 points with 7.2 million pulses total per curve) at T_1 and T_2 , (2) by individually comparing the intensities at T_1 and T_2 of mass 142 at one specific photon energy, 12.6 eV, and (3) by analyzing the results at 15.0 eV. A longer signal averaging condition of 9 million pulses was used for the last two cases. T_1 and T_2 were 583 and 613 K, respectively. A similar analysis was performed for mass 84 also. Table 5.1 summarizes the experimental ΔH_{vap} values obtained. The experimental ΔH_{vap} values have been corrected to 298.15 K using a ΔC_p value of -105.4 $J \cdot K^{-1} \cdot mol^{-1}$ for $[BMIM]^+[dca]^-$ and $[pyrr_{14}]^+[dca]^-$,[95] and a value of -94 $J \cdot K^{-1} \cdot mol^{-1}$ for $[pyrr_{14}]^+[NTf_2]^-$.[88]

$$\Delta H_{vap}(298.15\ K) = \Delta H_{vap}(T) + \Delta C_p \Delta T \quad (5.5)$$

The uncertainties in Table 5.1 represent twice the standard deviation of the measurements. The larger uncertainties in these measurements are the result of having fewer data points across similar temperature ranges for determining the heat of vaporization versus the more extensive maps versus temperature in the referenced works.

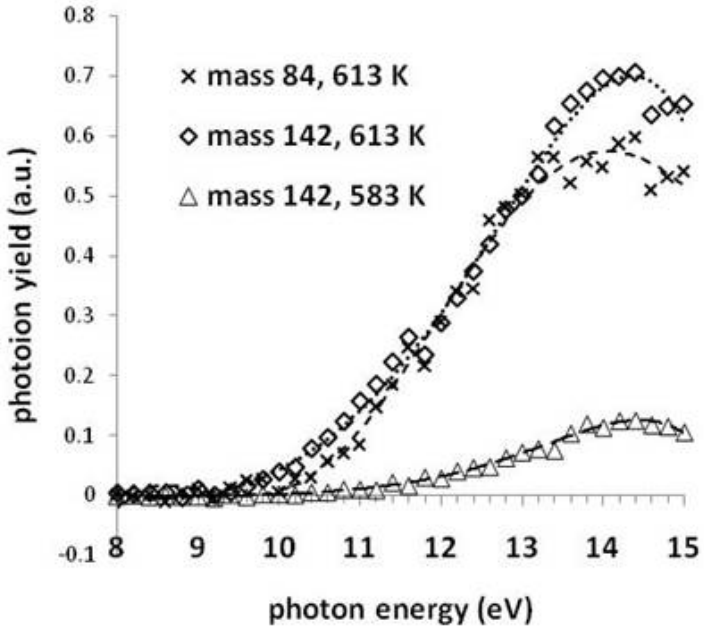

Figure 5.4. Photoionization efficiency (PIE) curves of $[pyrr_{14}]^+[NTf_2]^-$ for mass 142 at 583 and 613 K and mass 84 at 613 K.

Good agreement for ΔH_{vap} calculated using masses 142 and 84 (170.5 vs. 162.9 kJ/mol, Table 5.1) indicates the possibility of calculating ΔH_{vap} from mass fragments of the cation, and mass 84 was used successfully to determine the ΔH_{vap} of $[pyrr_{14}]^+[dca]^-$. One possibility why mass 84 is usable for determining the heat of vaporization for the $[pyrr_{14}]^+$-containing RTILs may be due to

its increased stability from possible resonance structures of the cation.[95] This stability also could explain the significant fragmentation of the intact cation to mass 84 under such soft ionization conditions. Mass 84 analysis for the heat of vaporization of $[pyrr_{14}]^+[dca]^-$ agrees reasonably well with the reported literature value (Table 5.2). For $[BMIM]^+[dca]^-$, masses 82, 97, 124 and 137 were used to calculate the heat of vaporization, and the reported heat of vaporization value is slightly higher than the literature value (Table 5.1). The successful determination of ΔH_{vap} from fragment masses is important because for some RTILs the intact cation may not be detected. In fact, only a very weak parent cation ion peak at mass 142 was detected for $[pyrr_{14}]^+[dca]^-$ and no parent peak at mass 139 was detected for $[BMIM]^+[dca]^-$. The present ΔH_{vap} of $[pyrr_{14}]^+[NTf_2]^-$ is consistent with heats of vaporization determined for other NTf_2^- based RTILs.[90-91, 97, 103-105] The temperatures used in these experiments are well below the reported onset decomposition temperatures (non-zero DSC slope) for these species (Table 5.2).

Table 5.1. Heats of vaporization data. All values are in kJ/mol. Uncertainties in the present work are twice the standard deviation.

$[pyrr_{14}]^+[NTf_2]^-$	ΔH_{vap}(PIE)	ΔH_{vap} (12.6 eV)	ΔH_{vap} (15.0 eV)	ΔH_{vap} (avg)	
mass 142	180.3	156.6	174.6	170.5	
mass 84	167.9	155.3	165.4	162.9	
			Average of six values =	166.7	
			correction to 298.15 K =	28.2	
			ΔH_{vap}(298.15) =	**195±19**	
$[pyrr_{14}]^+[dca]^-$	ΔH_{vap} (483/473 K)	ΔH_{vap} (493/483 K)	ΔH_{vap} (493/473 K)	ΔH_{vap} (avg)	ΔH_{vap} (slope)[1]
mass 84, 12.0 eV	145.2	157.1	151.1	151.1	151.0
			correction to 298.15 K =	9.5	
			ΔH_{vap}(298.15) =	**171±12**	
$[BMIM]^+[dca]^-$	ΔH_{vap} (mass 82)	ΔH_{vap} (mass 97)	ΔH_{vap} (mass 124)	ΔH_{vap} (mass 137)	ΔH_{vap} (avg)
PIE 483/468 K	148.4	157.4	162.4	154.8	155.8
			correction to 298.15 K =	18.7	
			ΔH_{vap}(298.15) =	**174±12**	

[1] ΔH_{vap}(slope) was determined via the slope of plotting lnI versus 1/T at 473, 483, and 493 K, where ΔH_{vap} = -slope*R.

Table 5.2. Experimental and literature values for heats of vaporization and temperatures of decomposition.

RTIL	T(K) range	this work ΔH_{vap} (kJ mol^{-1}) (average)	$\Delta C_p \Delta T$ (kJ mol^{-1})	this work ΔH_{vap} (kJ mol^{-1}) (298.15 K)	literature ΔH_{vap} (kJ mol^{-1}) (298.15 K)	$T(K)_{decomposition}$
$[BMIM]^+[dca]^-$	468-483	156±12	18.7	174±12	157.2 ± 1.1[a]	513[c]
$[pyrr_{14}]^+[dca]^-$	473-493	151±18	19.5	171±12	161.0 ± 2.0[b]	535[d]
$[pyrr_{14}]^+[NTf_2]^-$	583-613	167±19	28.2	195±19		672[d]

[a]reference [88], [b]reference [95], [c]reference [106], [d]references [94, 106].

To assess the temperature dependence of the photoionization cross section, the relative shapes of the PIE curves obtained at the experimental reservoir temperatures were compared. Figure 5.5(a) shows the comparison of the $[pyrr_{14}]^+[NTf_2]^-$ mass 142 PIE curves at 583 K and 613 K. In order to try to force the curve shapes to match, rather than simply scaling the PIE curve at 583 K to the PIE curve at 613 K so that the highest points match, the PIE curve at 583 K (I_{583}) was scaled iteratively to fit to the 613 K data (I_{613}) by a least squares fit where the sum of the squares of the difference between two points at a fixed photon energy was minimized:

$$(d/dS)\Sigma\,(S\times I_{583} - I_{613})^2 = 0 \qquad (5.6)$$

By this method, if the scaled PIE curves are identical, then $\Sigma(S\times I_{583} - I_{613})^2$ would necessarily equal zero, where S ($=I_{613}/I_{583}$) is the scaling factor. However, if the curves do not match exactly, then $\Sigma\,(S\times I_{583} - I_{613})^2 > 0$. In Figures 5.5(a)-(b), for $[pyrr_{14}]^+[NTf_2]^-$ the high temperature PIE curves for both mass 142 and mass 84 appear to have shifted slightly to higher intensities between 10 and 13.6 eV ($S\times I_{583} < I_{613}$), and to lower intensities above 13.6 eV ($S\times I_{583} > I_{613}$) relative to the low temperature PIE curves. Due to this slight shift in the PIE shape at higher temperature, in the region where the PIE intensity increases with temperature: $S\times I_{583} < I_{613}$ (10-13.6 eV), the Clausius-Clapeyron approach systematically overestimates the heat of vaporization. In the region where the PIE intensity decreases with temperature above 13.6 eV where $S\times I_{583} > I_{613}$, the Clausius-Clapeyron calculation will underestimate the heat of vaporization. Because there are more points in the PIE summed calculation where $S\times I_{583} < I_{613}$ (8-13.6 eV, 29 points) than where $S\times I_{583} > I_{613}$,(13.8-15 eV, 7 points), the PIE summed result from the Clausius-Clapeyron calculation will systematically overestimate the actual heat of vaporization, although these effects will tend to cancel somewhat. If, instead of determining the heat of vaporization of $[pyrr_{14}]^+[NTf_2]^-$ using the ratio of summed PIE intensities ($I_{613}/I_{583} = 6.17$, $\Delta H_{vap} = 180.3$ kJ/mol, Table 5.1) of mass 142 in the Clausius-Clapeyron equation, one uses the curve fitting scaling factor S = 5.29 from Figure 5.5(a) using equation (5.6), the result is $\Delta H_{vap} = 165.0$ kJ/mol, a reduction in the calculated value of ΔH_{vap} by 8.9% A similar treatment for mass 84 (Figure 5(a)) and for masses 97 and 137 of $[BMIM]^+[dca]^-$ in Figures 5.5(c)-(d) result in overestimates of 1.1%, 6.3%, and 1.1% respectively.

The similar shifts in the PIE curves in Figure 5.5 indicate this is a systematic phenomenon. Based on ΔH_{vap} calculated from the measured PIE curve sum values and comparison with the scaling factor analysis which takes into account the slight temperature shift in PIE curves, the

ΔH_{vap} values determined by PIE summed data likely contain a systematic overestimation of 1 to 10%, depending on how much the PIE curve shifts at the higher temperature. An improvement in the accuracy of this method will be to select a photon energy where competition between photoionization cross section and ion fragmentation tend to cancel each other out, namely where the scaled PIE curves cross and $S = I_2/I_1$. For example, monitoring the vapor density as a function of temperature at ~13.6 eV and determining ΔH_{vap} from the slope of a plot[95] of lnI versus 1/T would increase both the accuracy and precision of this method.

The PIE curve shift at higher temperature could be due to several factors. Competition between increased photoionization cross section and increased ion fragmentation at high temperatures may account for this observed shift. Below 13.6 eV, a larger photoionization cross section at high temperatures could explain the shift to higher intensities, and above 13.6 eV, increased ion fragmentation reduces the PIE intensity. A direct comparison of the branching ratios of masses 84/142 at two different temperatures is shown in Figure 5.6. Above ~12 eV, the increase in branching ratio at higher temperature indicates increased ion fragmentation with increasing temperature.

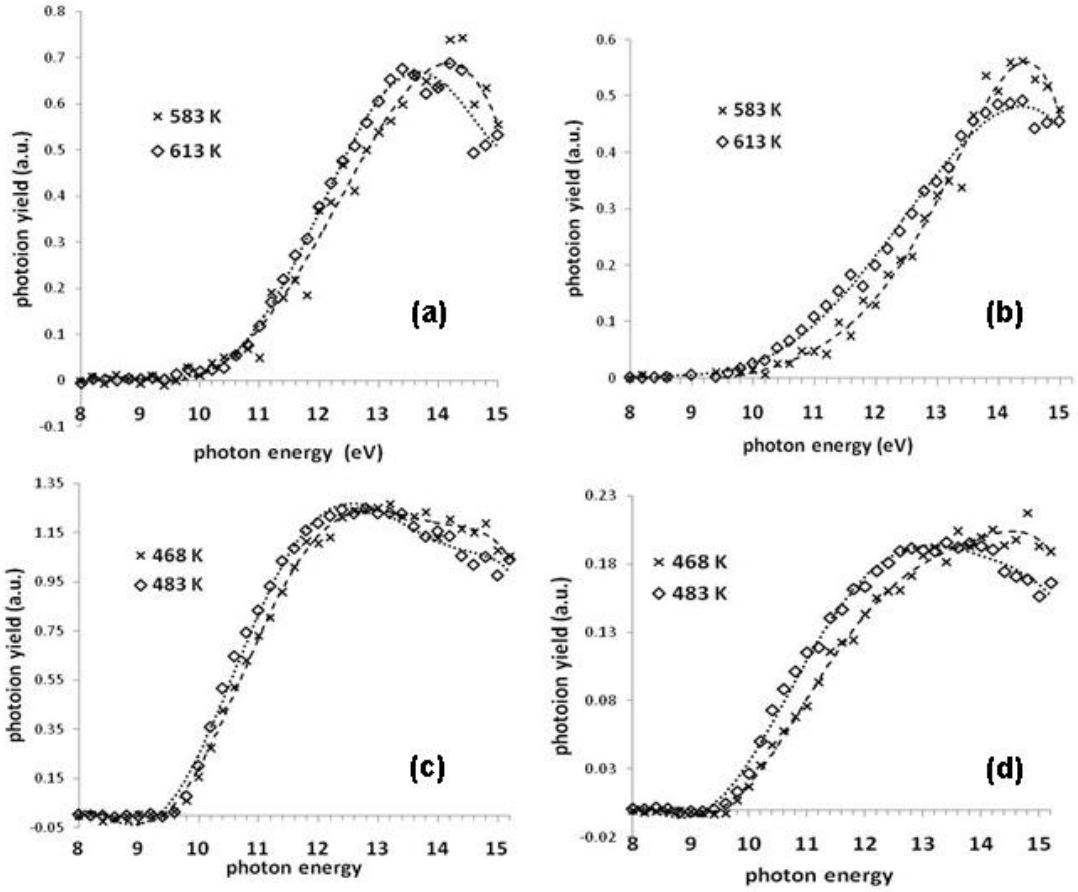

Figure 5.5. Least-squares fit analyses using equation (5.6) of the PIE curves for (a) $[pyrr_{14}]^+[NTf_2]^-$ of mass 142 at 583 K relative to 613 K, (b) $[pyrr_{14}]^+[NTf_2]^-$ of mass 84 at 583 K relative to 613 K, (c)

$[BMIM]^+[dca]^-$ of mass 97 at 468 K relative to 483 K, and (d) $[BMIM]^+[dca]^-$ of mass 137 at 468 K relative to 483 K.

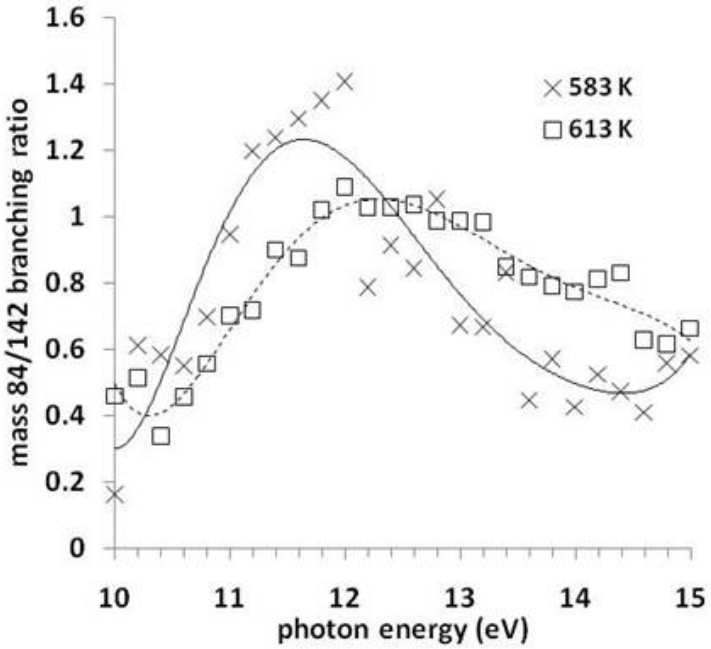

Figure 5.6. Mass 84/142 branching ratios for $[pyrr_{14}]^+[NTf_2]^-$ at 583 K and 613 K as a function of photon energy.

There are several advantages for using photoionization versus electron impact ionization for measuring heats of vaporization for RTILs. The narrow energy spread of the light source (0.025 eV) and soft ionization conditions minimize the effect of fragmentation of the parent cation and allows for appearance energies to be determined accurately. Typical electron impact ionization energies are around 70 eV, where the electron impact ionization cross section curve is large and the shape of the curve is flat for many atomic and molecular species, but fragmentation to smaller species can be extensive. In this work, photoionization measurements yield a branching ratio of masses 84/142 of nearly one for $[pyrr_{14}]^+[NTf_2]^-$, indicating the small extent of fragmentation of the $[pyrr]^+$ under the present soft ionization conditions versus electron impact ionization of $[pyrr_{14}]^+[dca]^-$ with a branching ratio of masses 84/142 that is about an order of magnitude higher.[95] Although fragmentation of the parent ion can be minimized by lowering the electron impact energy, the electron impact ionization cross section changes rapidly as a function of electron energy near the ionization threshold,[107-108] and the result may be highly susceptible to thermal effects near the ionization threshold. Also, the energy spread of a typical electron gun is limited to > 0.5 eV, limiting the energy resolution in threshold measurements. Therefore, determining appearance energies of ions by electron impact ionization is difficult and has large associated uncertainties.

From the accurate determination of photoion appearance energies by the present method, comparison with theoretical energy calculations can be made. *Ab initio* calculations of the

energetics involved in the dissociative photoionization processes (described below) are in excellent agreement with the experimentally determined photoion appearance energies. The measured mass 142 appearance energy in Figure 5.4 (9.4 ±0.2 eV) agrees well with the *ab initio* value of 9.2±0.1 eV calculated at the MP2 6-31+G(d,p) level of theory (0 K, ZPVE corrected) for the $[pyrr_{14}]^+[NTf_2]^-$ ion pair (equation 5.7). An appearance energy of 10.1 ± 0.1 eV (experimental value = 10.0 ± 0.2 eV) was calculated for mass 84, assuming elimination of C_4H_{10} from the $pyrr_{14}^+$ cation to form the resonance stabilized cationic structure postulated in a previous publication (equation 5.8),[95] The electron affinity for the $NTf_2\cdot$ radical is calculated to be 5.7 eV at the MP2 6-31+G(d,p) level of theory.

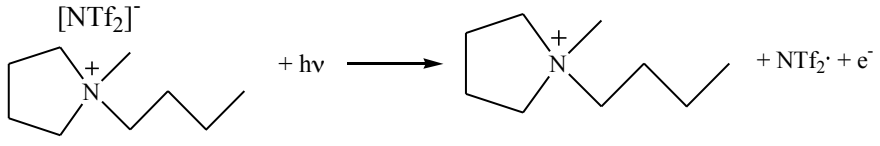

(5.7)

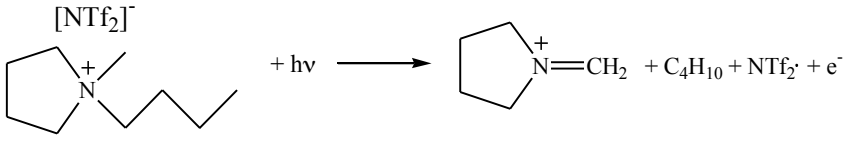

(5.8)

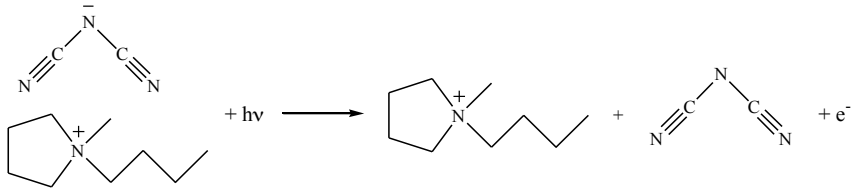

(5.9)

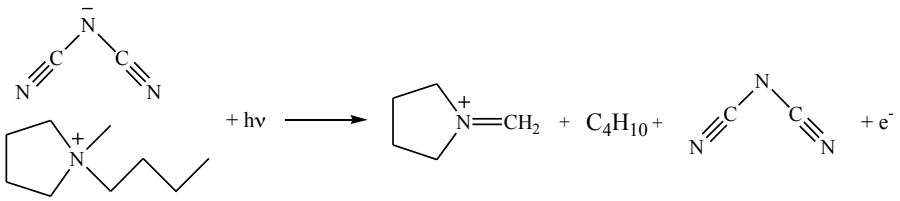

(5.10)

Calculation of the adiabatic ionization potential of dicyanamide at the MP2 level was precluded due to the inadequacy of a single configuration reference wavefunction for the neutral dicyanamine species.[2] However, the electron affinity for the dicyanamide radical has been determined experimentally to be 4.135 eV.[109] Using this value along with the theoretical values in Table 5.3, the appearance energy for mass 84 in equation 5.10 is estimated to be 8.73 ± 0.1 eV, which is in excellent agreement with the experimental appearance energy for mass 84 in the $[pyrr_{14}]^+[dca]^-$ dissociative photoionization of 8.8±0.2 eV. The estimated appearance energy of the intact $[pyrr_{14}]^+$ cation in equation 5.9 is 7.81 eV. However, the experimental signal-to-noise ratio for this species was not sufficient to determine its appearance energy although it was detectable at higher energies. Overall, the agreement between theory and experiment supports the dissociative photoionization of isolated cation-anion ion pairs in the gas phase.

Table 5.3. *Ab initio* energies (in eV) of proposed species involved in dissociative photoionization of $[pyrr_{14}]^+[NTf_2]^-$.

specie	E_0	zero point energy	total H_0
$[pyrr_{14}]^+[NTf_2]^-$ ion pair	-60738	9.48	-60728
$[pyrr_{14}]^+[NTf_2\bullet]$ ion pair cation	-60729	9.43	-60720
$[pyrr_{14}]^+$ cation	-11108	7.98	-11100
$[NTf_2]^-$ anion	-49626	1.46	-49625
$NTf_2\bullet$ neutral radical	-49620	1.44	-49619
$[dca]^-$ anion	-6526	0.54	-6526
mass 84 cation	-6810	4.11	-6806
butane	-4297	3.69	-4293

5.1.4 Conclusions

Heats of vaporization for several room temperature ionic liquids have been determined by effusive beam VUV photoionization mass spectrometry. The photoionization cross section is considered to be temperature independent when using the PIE curves for the Clausius-Clapeyron analysis. We estimate a positive systematic error of up to 10% for this assumption. After thermal correction to 298.15 K, the ΔH_{vap} values of $[BMIM]^+[dca]^-$ and $[pyrr_{14}]^+[dca]^-$ reported here are in reasonable agreement with the previously reported experimental values. For $[pyrr_{14}]^+[NTf_2]^-$, ΔH_{vap}(298.15 K) is calculated to be 195±19 kJ mol^{-1}, which has not been reported previously. Detection of the intact $[pyrr_{14}]^+$ cation is indicative of the presence of neutral cation-anion ion pairs in the effusive beam which dissociate to form $[pyrr_{14}]^+$ and neutral $NTf_2\cdot$ at low VUV photon energy. A second dissociation pathway detected is the efficient fragmentation of $[pyrr_{14}]^+$ to produce mass 84. Together, these experimental heats of vaporization, photoionization appearance energies, and *ab initio* calculations support a vaporization mechanism for RTILs as intact cation-anion ion pairs.

- Acknowledgement

Funding for this work was provided by the Air Force Office of Scientific Research under Contract No. FA9300-06-C-0023 with the Air Force Research Laboratory, Edwards AFB, CA 93524, and grant FA9550-07-1-0059 to the University of California, Berkeley. Research at the Advanced Light Source is supported by the Director, Office of Science, Office of Basic Energy Sciences, of the U.S. Department of Energy under Contract No. DE-AC02-05CH11231 at the Lawrence Berkeley National Laboratory. S.R.L. gratefully acknowledges the generous support of a Morris Belkin Visiting Professorship at the Weizmann Institute of Science. This research is partly supported by the Air Force Summer Faculty Fellowship Program administered by the ASEE (Contract No. FA9550-07-C-0052). Special thanks to Dr. Jerry Boatz for helpful discussions on MP2 calculations and donation of CPU time.

5.2 Ultraviolet Photoionization Efficiency of the Vaporized Ionic Liquid 1-Butyl-3-Methylimidazolium Tricyano-methanide: Direct Detection of the Intact Ion Pair

We present the first direct measurement of a neutral, intact ion pair photoionization efficiency (PIE) curve for a vaporized ionic liquid, 1-butyl-3-methylimidazolium tricyanomethanide, using tunable vacuum ultraviolet (VUV) photoionization time of flight mass spectrometry (PI-TOFMS). The ionization potential (IP) for the ion pair is experimentally determined to be 6.6 ± 0.5 eV, which matches reasonably well with the adiabatic IP of 7.3 ± 0.2 eV calculated at the M06/6-31+G(d,p) level of theory. The lifetime to dissociation of the cation-radical complex formed upon ionization of the ion pair is highly dependent upon entropic contributions. Thermal gravimetric analyses (TGA) determined both the enthalpy of vaporization ΔH_{vap}(298 K) = 143.5 ± 6.2 kJ/mol and the activation enthalpy for thermal decomposition for this ionic liquid $\Delta H^{\ddagger}$(T_{avg} = 582 K) = 183.0 ± 4.3 kJ/mol, indicating vaporization of $BMIM^{+}TCM^{-}$ as ion pairs is the dominant mechanism for mass loss under the experimental conditions for VUV PI-TOFMS (T = 433 K).

5.2.1 Introduction

Although molten salts, more recently known as ionic liquids (ILs), have been known for almost a century (for example, ethylammonium nitrate, MP = 12 °C, was discovered in 1914),[2] the rapid development of ionic liquid chemistry has only occurred within the last decade; In 2000, only 217 papers were published on the subject, whereas in 2010, over 6,000 papers were published.[3] The major interests in ionic liquids are due to such properties as: 1) extremely low vapor pressures, making ILs suitable for volatile organic compound (VOC) solvent replacements, 2) thermal stability (non-flammability), 3) high conductivity (suitable for electrochemistry and fuel cells), and 4) high energy density (suitable as "green" propellants). The number of possible ILs has been estimated at 10^{18}.[21] ILs are based on cations such as, but not limited to, ammonium, imidazolium, triazolium, tetrazolium, and phosphonium cations. Common anions include halides, nitrates, dicyanamides, bistrifluoromethylsulfonylimides and sulfonates. The popular assumption that ionic liquids exert no vapor pressure was disproved when certain classes of ILs were shown to distill in vacuum and the material recovered was identical to the starting

[3] SciFinder results searching for the concept 'ionic liquid' (August 2011).

material.[26] However, the vaporization mechanism of a distilling IL has been somewhat controversial. Many ILs have activation barriers to thermal decomposition that can be comparable or below the enthalpy of vaporization of the IL so that decomposition competes with or dominates over vaporization.[74, 110-111] The question has arisen that upon vaporization, do the ILs, which exist as discrete ions in the liquid, vaporize as individual ions, as neutral ion pairs, or as neutral or charged ion clusters?

It has been shown that the most acidic proton on the cation largely determines the ILs thermal stability.[8] When hydrogens are attached to the cationic nitrogens, they are more acidic and those ILs have been termed "protic" ILs.[112] In general, protic ILs have lower thermal stability than ILs with alkyl substituents on the ring nitrogens, known as "aprotic" ILs. Vaporization of protic ionic liquids occurs via proton transfer from the cation to the anion, and the resulting neutral species formed can then evaporate.[112] Recent mass spectrometric experiments indicate the vaporization of many aprotic ionic liquids under vacuum distillation conditions proceeds via neutral cation-anion pairs, which is evidenced by the dissociative ionization of the ion pair and subsequent detection of the resulting cation:[27, 29]

$$C^+A^- + e^- \rightarrow C^+ + A\cdot + 2e^- \quad (5.11)$$
$$C^+A^- + h\nu \rightarrow C^+ + A\cdot + e^- \quad (5.12)$$

Ion cyclotron resonance experiments indicate vaporization of intact ion pairs from the detection of the cation upon injection of ionizing electrons and the further formation of charged clusters:[112-113]

$$C^+A^- + e^- \rightarrow C^+ + A\cdot + 2e^- \quad (5.13)$$
$$C^+ + [C^+A^-] \rightarrow [C^+A^-]C^+ \quad (5.14)$$

Selected ion flow tube (SIFT) experiments indicate vaporization of intact ion pairs by attachment of a third ion: $C_1^+A^- + C_2^+ \rightarrow C_1^+A^- C_2^+$.[114] Matrix isolation FTIR experiments have been able to identify the structure of ion pairs frozen in a rare gas matrix.[52] Due to the large UV photoabsorption cross section of the ion pair, UV measurements under vacuum distillation conditions have been able to accurately determine the values for the enthalpy of vaporization.[115] Theory has shown that the formation of single ion pairs is energetically favored over the formation of separate ions or clusters.[55] Gas phase ion pairs of vaporized 1-butyl-3-methylimidazolium tricyanomethanide ($BMIM^+TCM^-$) have been previously detected directly by pulsed field ionization mass spectrometry[99] at temperatures near or above the thermal decomposition onset temperature of the ionic liquid, presumably as vaporization still competes with thermal decomposition at these temperatures for this IL. It should be noted that $BMIM^+TCM^-$ was the first IL discovered to be enriched upon fractional distillation of IL mixtures,[99] and it has one of the lowest reported values for the enthalpy of vaporization for ionic liquids: $\Delta H_{vap}(298\ K) = 143.2 \pm 5$ kJ/mol.[116]

In this letter, we present the direct detection of intact ion pairs from the vaporized ionic liquid 1-butyl-3-methylimidazolium tricyanomethanide ($BMIM^+TCM^-$) by soft VUV photoionization, as well as the first measured PIE curve of a vaporized ionic liquid ion pair. This experimental breakthrough was possible due to the combination of high ion pair number density (by locating the effusive IL source as close as possible to the ionization region, Figure 5.7) and the high

sensitivity afforded by the synchrotron VUV light source. Thermal gravimetric analyses imply that the activation enthalpy to thermal decomposition is significantly higher than the enthalpy of vaporization, therefore vaporization of the ionic liquid dominates mass loss in these photoionization experiments. Once the ion pair is vaporized and subsequently ionized, even though entropy favors the dissociation of the cation-radical complex, the lifetime of the ionized ion pair is sufficiently long to measure the PIE curve of the intact ion pair.

5.2.2 Experimental Methods

The present experimental PIE measurement setup is a modification of a setup used previously.[27-28, 32, 53, 74] It uses a new, smaller effusive ionic liquid source that is mounted directly onto the repeller plate of the mass spectrometer ion optics; a pinhole in the repeller plate introduces the ionic liquid vapor into the ionization region (Figure 5.7).[117] This new configuration increases the ionic liquid vapor number density in the ionization region by approximately 250 times versus the previous setup. The ionic liquid source was maintained at 433 K, which is significantly lower than the thermal decomposition temperature for $BMIM^+TCM^-$, which is ~ 513 K as measured by thermogravimetric analysis (TGA), or the temperatures used (> 573 K) in the previous study where ion pairs were detected.[99] The ionic liquid sample (purchased from EMD, purity = 99.8%, HPLC) was loaded into the source, mounted into the vacuum chamber, pumped to < 10^{-7} Torr and degassed for 12 hours at 298 K, prior to carrying out any photoionization measurements. The PIE measurements were carried out between 7.4 eV and 10.0 eV in 0.050 eV steps and co-added for every 500,000 pulses (the VUV linewidth was 0.023 eV, FWHM). The PIE spectra were normalized for photon flux at each photon energy. TGA analysis was performed on a TA Instruments 2050 using approximately 5 mg of the ionic liquid sample, heated at 10 K/min from 323 K to 1073 K under N_2. The thermal decomposition temperature was determined by the temperature where a non-zero slope of the TGA curve was detected. In a separate isothermal TGA experiment, approximately 40 mg of the ionic liquid was heated from 423 K to 493 K in 5 K steps, and the temperature was held constant at each step for 450 minutes. DFT single point energy calculations were performed at the M06/6-31+G(d,p) level of theory (298 K, ZPVE corrected) using the Gaussian 09 suite of programs[100] unless otherwise noted, and the ionization potentials and photoion appearance energies are reported as ΔG values. The geometry of the $BMIM^+TCM^-$ ion pair was taken from reference 55.

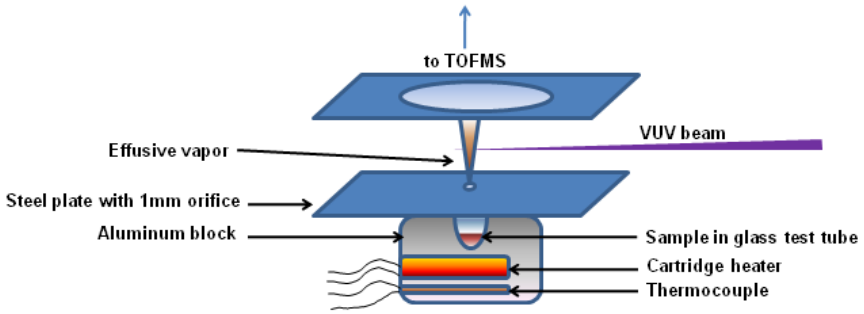

Figure 5.7. Effusive ionic liquid source.

5.2.3 Results and Discussion

The TGA of $BMIM^+TCM^-$ in Figure 5.8(a) reveals the thermal decomposition temperature to be ~ 513 K as determined by the onset of the non-zero slope. Figure 5.8(b) is an Arrhenius-type plot of the mass loss rate versus 1/T whose slope is equal to $-\Delta H^{\ddagger}/R$, where the activation enthalpy for decomposition is $\Delta H^{\ddagger}$ = 183.0 ± 4.3 kJ/mol at an average temperature of 582 K, where the reported error is twice the standard deviation (± 2σ). Isothermogravimetric analysis to determine the enthalpy of vaporization, ΔH_{vap}, of the ionic liquid[118] is shown in Figures 5.8(c)-(d), where ΔH_{vap} is determined to be 126.0 ± 6.2 kJ/mol (where the error is ± 2σ) at an average temperature of 473 K. Using a $\Delta_g{}^lC^o{}_{pm}$ value of 100 J/mol-K[116] for the change in molar heat capacity upon vaporization, the corrected ΔH_{vap}, at 298 K is 143.5 ± 6.2 kJ/mol, in excellent agreement with a previously reported value of 143.2 ± 5.0 kJ/mol.[116] Because $\Delta H^{\ddagger}$ is significantly higher than ΔH_{vap}, mass loss of the ionic liquid sample at 433 K should occur almost exclusively via vaporization, presumably as intact ion pairs.

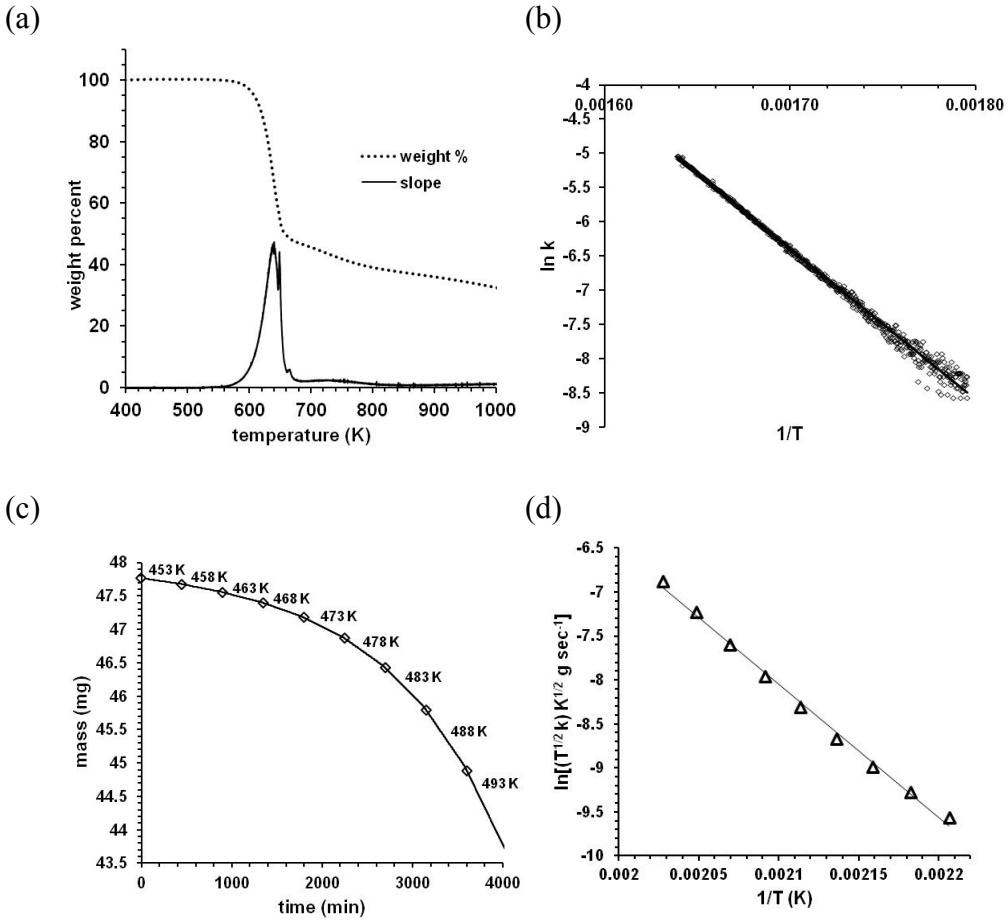

Figure 5.8. (a) Thermal gravimetric analysis (TGA) of 1-butyl-3-methylimidazolium tricyanomethanide ionic liquid. (b) $\Delta H^{\ddagger}$ = 183.0 ± 4.3 kJ/mol determined from the slope of the plot for the thermal decomposition of $BMIM^+TCM^-$ (TGA data from Figure 5.8(a), (c) Isothermal TGA of $BMIM^+TCM^-$ from 423 to 473 K at 5 K intervals, (d) ΔH_{vap} = 120 ± 6.2 kJ/mol at an average temperature of 473 K, determined from the slope of the plot for vaporization of $BMIM^+TCM^-$ (isothermal TGA data from Figure 2(c)). The 298 K corrected ΔH_{vap} is 143.5 ± 6.2 kJ/mol.

Photoionization mass spectra at a photon energy of 7.50 eV for $BMIM^+TCM^-$ is shown in Figure 5.9(a). Figure 5.9(b) clearly shows the ion pair at m/z = 229, and Figure 5.9(c) shows the cation formation at m/z = 139 from dissociative ionization of the ion pair, and the corresponding ^{13}C peaks are visible at m/z = 230 (15%) and 140 (9.6%), respectively.

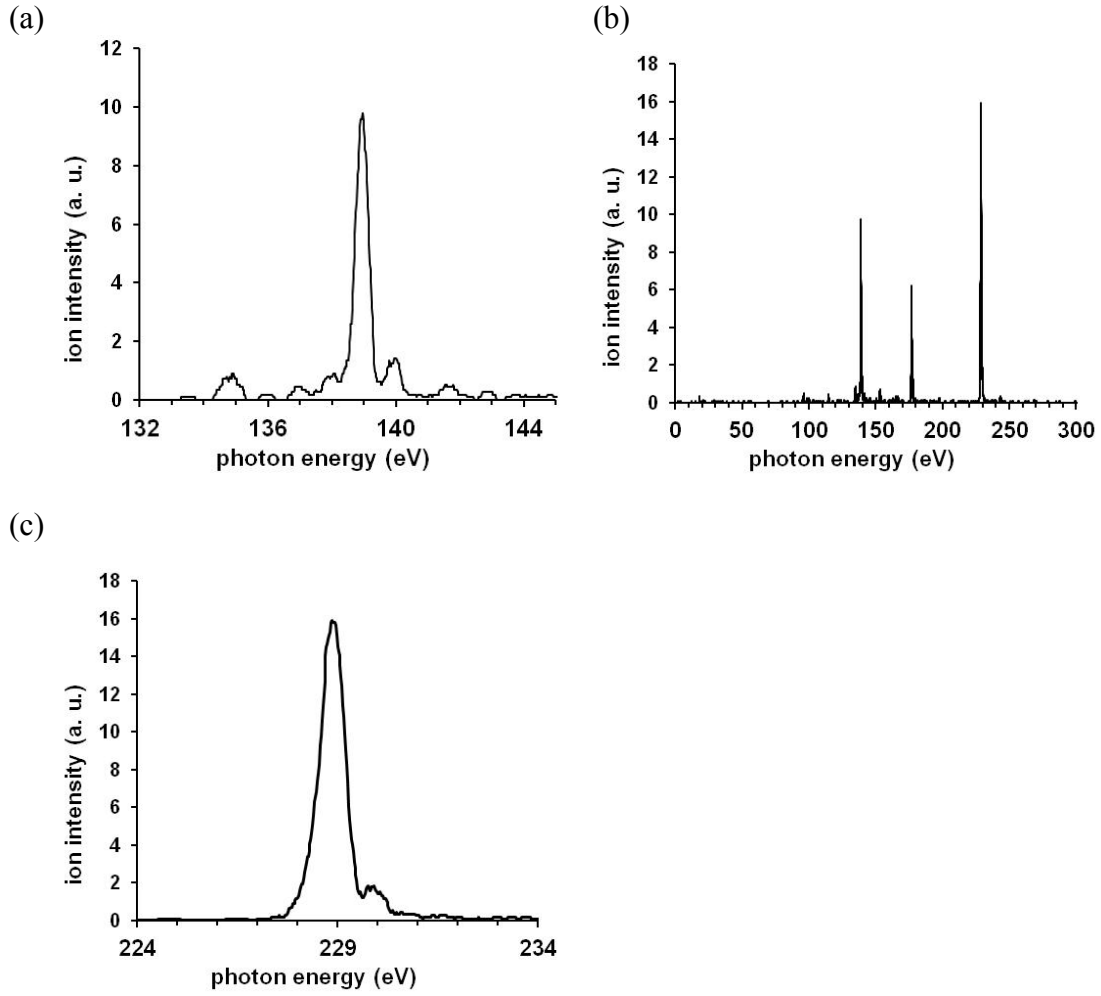

Figure 5.9. Mass spectra of 1-butyl-3-methylimidazolium tricyanomethanide at 7.50 eV photon energy: (a) full spectrum, (b) m/z 229 corresponding to the $BMIM^+TCM^-$ ion pair, and (c) m/z 139 corresponding to the $BMIM^+$ cation. All spectra have been smoothed by 25 points.

No cluster formation at higher masses is detected up to m/z 600. Figures 5.10(a)-(b) show the photoionization efficiency (PIE) curve for the ion pair (m/z = 229). In Figure 5.10(b), the PIE curve is fit using a functional form $a(E-E_o)^2$ using a least squares analysis where a is a normalization factor, E is the photon energy, and E_o is the ionization potential (IP) to be fit.[32] This analysis yields an IP of 6.6 ± 0.5 eV, which matches reasonably well with the M06 calculated adiabatic IP of 7.3 ± 0.2 eV. The $BMIM^+$ cation formed upon dissociative ionization of the ion pair has an appearance energy (AE), determined similarly to the IP above, of 6.9 ± 0.5

eV, with a calculated value of 6.9 ± 0.2 eV at the M06/6-31+G(d,p) level of theory. The larger uncertainty of ± 0.5 eV associated with the experimental IP and AE values below 7.4 eV is due to the need to extrapolate the IP from the PIE data which are only measured above 7.4 eV (7.4 eV being the lower limit of the synchrotron undulator output).

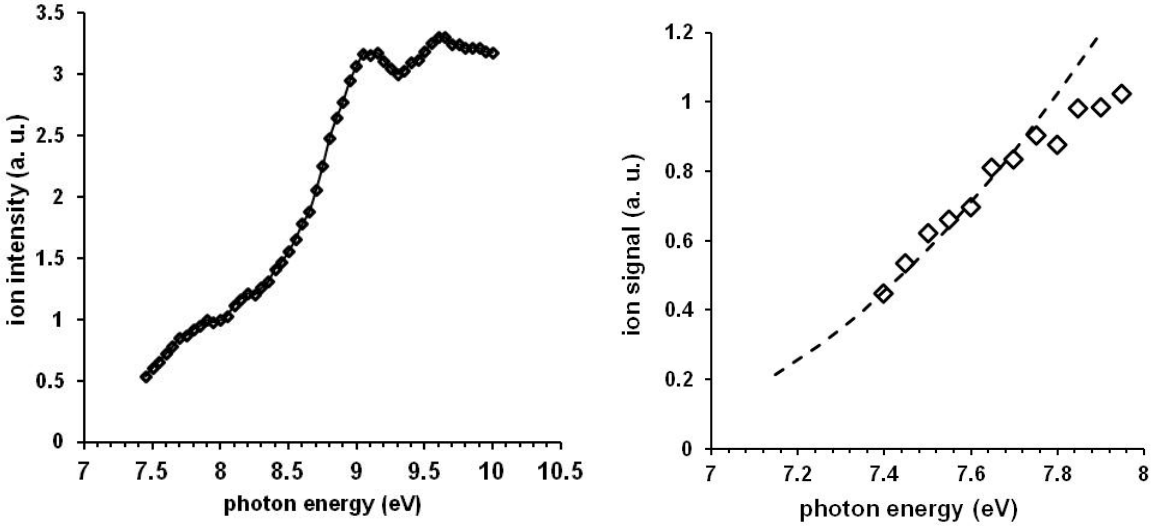

Figure 5.10. (a) Photoionization efficiency (PIE) curve for the $BMIM^+TCM^-$ ion pair, m/z 229 and (b) enlarged image of (a) near the appearance threshold, where the dashed line indicates the fit to determine the ionization potential (IP).

It has been postulated that previous photoionization experiments on vaporized ionic liquids have been unable to detect the intact ion pair because the IP of the ion pair and the AE of the cation (corresponding to the energy of the separated cation and radical: $C^+A\cdot \rightarrow C^+ + A\cdot$) have similar energies and that the ionized ion pair may dissociate on a timescale much faster than that of the ion's residence time in the high field acceleration region of the TOFMS.[28] For the case of $BMIM^+TCM^-$, it is important to note the experimental AE of the cation is at least 300 meV higher in energy than the IP for the ion pair. This energy difference could mean that the lifetime of the ionized ion pair is long enough relative to the timescale of ion acceleration in the TOF mass spectrometer so that it is readily detected in this experiment. The relatively low temperature of the effusive source required, due to the high vapor pressure of $BMIM^+TCM^-$ relative to other ILs, could also help to minimize the internal energy of the vaporized ion pair, aiding in the detection of its parent photoion. Using Rice-Ramsperger-Kassel-Marcus (RRKM) theory with a tight transition state, the upper limit of the lifetime of the ion pair cation to dissociate to the cation plus radical can be estimated. At 433 K, using ChemRate,[119] the density of states of the ground electronic state of the $BMIM^+TCM^\cdot$ cation-radical complex is calculated from the vibrational frequencies (scaled by 0.994[120]) at the M06/6-31+G(d,p) level of theory and the number of states in the dissociating complex is determined by removing the vibrational frequency corresponding to the dissociation of the complex.[121] The calculated lifetimes of the reaction $BMIM^+TCM^\cdot \rightarrow BMIM^+ + TCM^\cdot$ as a function of the enthalpy of reaction are shown in Table 5.4. With a barrier of 300 meV, which corresponds to the experimental difference in the ion pair IP and the AE of the cation, the lifetime is 1.0 nsec. Due to the large uncertainty in the IP and AE of the cation of 0.5 eV, if a barrier height of 500 meV is used, the lifetime of the

cation-radical complex increases to 100 nsec. Under our experimental conditions, the time duration of m/z 229 in the acceleration region of the TOFMS is calculated to be 188 nanoseconds. The latter m/z 229 lifetime is sufficiently long for the intact cation-radical complex to reach the field-free region in the TOFMS, and thus the parent ion is detectable. Dissociation of m/z 229 to smaller cationic fragments in the field-free region of the TOFMS could also occur, but these ion fragments would still be detected at nearly the same time of flight as the intact ionized ion pair. If fragmentation in the field free region imparts significant kinetic energy to the ion fragment, peak broadening can occur, but broadening of the m/z 229 peak is not apparent, so either little fragmentation takes place or fragmentation occurs with very little kinetic energy release. In contrast, the 1-ethyl-3-methylimidazolium-$NTf_2^{\cdot}$ cation-radical complex, as well as other aprotic ionic liquids, may not have such a large barrier to dissociation, which would explain why the ion pair is not detected in previous experiments.[28, 32, 53]

Table 5.4. Calculated lifetimes of the reaction $BMIM^+TCM^{\cdot} \rightarrow BMIM^+ + TCM^{\cdot}$ as a function of the enthalpy of reaction (ΔH).

ΔH (kJ/mol)	**Lifetime (nsec)**
28.9	1.0
48.2	100

In evaluating the dissociation energy of the ionized $BMIM^+TCM^-$ ion pair, which can be described as an ion-radical complex, $BMIM^+TCM^{\cdot}$, there are dispersion forces that weakly bind the $TCM^{\cdot}$ radical to the $BMIM^+$ cation, and the dissociation process is endothermic. However, the entropy gained upon dissociation of the cation-radical complex from a single particle to two particles can lower the free energy enough to make this dissociation process exoergic. While the M06 calculated difference between enthalpy and free energy for the ionization process is small: $\Delta H_{\text{ionization}} = 7.40$ eV, $\Delta G_{\text{ionization}} = 7.34$ eV, the difference between enthalpy and free energy in the dissociative ionization (DI) of the cation-radical process is large (0.62 eV): $\Delta H_{\text{DI}} = 7.49$ eV, $\Delta G_{\text{DI}} = 6.91$ eV, indicating that the dissociation is an entropy-driven process. Calculation of the free energy profile of the cation-radical dissociation is beyond the scope of this paper, but it could be possible that, due to competition between energetic and entropic effects, there exists a barrier on the free energy coordinate that leads to dissociation. This barrier might be large enough to keep the cation-radical complex intact long enough for it to be detected in the VUV-TOFMS experiment. For other aprotic ionic liquid systems, this free energy barrier may not be sufficiently high for the cation-radical to exist long enough to be measured experimentally, which would explain why their ion pairs have not been detectable experimentally.

5.2.4 Conclusion

We have presented the first measured photoionization efficiency curve of an intact ion pair of the vaporized ionic liquid 1-butyl-3-methylimidazolium tricyanomethanide, which has an estimated RRKM lifetime of the ionized ion pair of up to 100 nsec. Dissociation of the ionized ion pair is dominated by the entropic contributions. Experimental determination that the enthalpy of activation for thermal decomposition is substantially higher than the enthalpy of vaporization for

this ionic liquid provides further evidence that vaporization is the dominant mechanism under VUV PI-TOFMS experimental conditions.

▪ Acknowledgement

The authors gratefully acknowledge funding from the U.S. Air Force Office of Scientific Research for supporting S.D.C. (Grant No. FA9300-06-C-0023) and for C.K. and S.R.L. (Grant No. FA9550-10-1-0163). This work at the ALS was supported by the Director, Office of Energy Research, Office of Basic Energy Sciences, Chemical Sciences Division of the U.S. Department of Energy under Contract No. DE-AC02- 05CH11231 (A.G. and S.R.L.). We would like to thank Jerry Boatz for helpful discussions and Amanda Wheaton for obtaining the TGA data.

5.3 Thermal decomposition mechanism of 1-ethyl-3-methyl-imidazolium bromide ionic liquid

In order to better understand the volatilization process for ionic liquids, the vapor evolved from heating the ionic liquid 1-ethyl-3-methylimidazolium bromide ($[Emim]^+[Br]^-$) was analyzed via tunable vacuum ultraviolet photoionization time of flight mass spectrometry (VUV-PI-TOFMS) and thermal gravimetric analysis mass spectrometry (TGA-MS). For this ionic liquid, the experimental results preclude the possible vaporization of intact ion-pairs or the formation of carbenes, but instead indicate the evolution of alkyl bromides and alkylimidazoles, presumably through alkyl abstraction via an S_N2 type mechanism, and show that vaporization of intact ion pairs or the formation of carbenes is negligible. Activation energies for the formation of the methyl and ethyl bromides were evaluated experimentally, $\Delta H^{\ddagger}$ (CH_3Br) = 116.1 ± 6.6 kJ/mol and $\Delta H^{\ddagger}$ (CH_3CH_2Br) = 122.9 ± 7.2 kJ/mol, and the results are found to be in agreement with calculated values for the S_N2 reactions. Comparisons of product photoionization efficiency (PIE) curves with literature data are in good agreement, and *ab initio* thermodynamics calculations are presented as further evidence for the proposed thermal decomposition mechanism. Estimates for the heat of vaporization of 1-ethyl-3-methylimidazolium bromide, $[Emim]^+[Br]^-$, and 1-butyl-3-methylimidazolium bromide, $[Bmim]^+[Br]^-$, from molecular dynamics calculations and their gas phase enthalpies of formation obtained by G4 calculations yield estimates for the ionic liquids' enthalpies of formation in the liquid phase: ΔH_{vap}(298 K) ($[Emim]^+[Br]^-$) = 168 ± 20 kJ/mol, $\Delta H_{f,\,gas}$(298 K) ($[Emim]^+[Br]^-$) = 38.4 ± 10 kJ/mol, $\Delta H_{f,\,liq}$(298 K) ($[Emim]^+[Br]^-$) = −130 ± 22 kJ/mol, $\Delta H_{f,\,gas}$(298 K) ($[Bmim]^+[Br]^-$) = −5.6 ± 10 kJ/mol, and $\Delta H_{f,\,liq}$(298 K) ($[Bmim]^+[Br]^-$) = −180 ± 20 kJ/mol.

5.3.1 Introduction

Recent interest in ionic liquids, salts with melting points ≤ 100 °C, has stemmed from their extremely low volatility, thermal stability, and the enormous number of ionic liquids possible ($\sim 10^{18}$)[21] by varying either the cation or the anion. The physical and chemical properties of ionic liquids can also be tailored by modifying the functional groups on either ion. Ionic liquids have been studied for use as replacement solvents for volatile organic compounds (VOCs),[122-125] fuel cells,[77-79, 126] electrolytes,[16, 76] ingredients for energetic materials and propellants,[20, 23, 80] and as high temperature lubricants.[127-129]

Understanding thermal stability of ionic liquids is important for the safe storage and transportation of these compounds.[130] Protic ionic liquids, having a hydrogen bound to a nitrogen on the cation, are thermally unstable and easily neutralized via proton transfer to the anion.[35] These neutral species can volatilize and reform ionic liquids on co-condensation of the vapors by the acid-base reaction. Aprotic imidazolium ionic liquids, having alkylated nitrogens in the cation, have been seen to undergo dealkylation under pyrolytic conditions to yield 1-substituted imidazoles, presumably through an S_N2 type mechanism,[98, 130-132] which would explain why the thermal stability of imidazolium-based ionic liquids increases with increasing anion size,[106, 131] increasing the length of the side chain (steric effects),[131] or decreasing nucleophilicity of the anion.[131] Alkyl substituents such as vinyl and phenyl tend to increase the stability of the cation due to charge delocalization to the side chain and are not susceptible to cleavage,[131] while secondary and tertiary alkyl groups on the cation make the ionic liquid less thermally stable, presumably due to the elimination of the stabilized alkyl cations.[93] There is also some evidence for the elimination of ethylene from ethylimidazolium ionic liquids with increasing basicity of the anion.[131] The acidic character of the C2 proton of the imidazolium cation, illustrated by the facile deuterium exchange in D_2O,[133] seen also in thiazolium salts,[134] could also be a factor in the thermal stability of imidazolium-based ionic liquids, and addition reactions with the imidazolium ring have been observed at high temperatures.[132] Alkyl substitution of the C2 hydrogen on the imidazolium ring has the largest effect on the thermal stability due to the acidity of this proton.[93] This acidity stems from the stability of the carbene species formed upon proton loss from C2.[133, 135] This n-heterocyclic carbene (NHC) species may play an important role in the addition reactions mentioned above,[136-138] and its formation can be facilitated by basic anions.[139] While the presence of oxygen does not appear to affect the temperature of decomposition of imidazolium ionic liquids, ionic liquids having endothermic decompositions in an inert atmosphere turn exothermic in an oxygen atmosphere midway through the observed mass loss in thermal gravimetric analysis (TGA) when combustion dominates.[93]

Previous studies on the vaporization of ionic liquids indicate that some aprotic ionic liquids, especially those with anions which are the conjugate bases of superacids,[140] vaporize as intact ion pairs, evidenced by the dissociative ionization (equation 1.1) of the ion pair and the detection of the intact cation by mass spectrometry: $C^+A^- + h\nu \rightarrow C^+A + e^- \rightarrow C^+ + A\bullet + e^-$. The removal of the electron from the anion eliminates the coulombic attraction between the ions, and the weakly bound cation-radical complex dissociates prior to detection in the mass spectrometer. Direct detection of the ion pair via mass spectrometric techniques has been elusive, but recent progress has been made to directly identify these in the gas phase.[54, 81]

If the rates of thermal decomposition of ionic liquids are comparable to the rate of evaporation of ion pairs from the ionic liquid, the resulting species in the gas phase are a mixture of thermal decomposition products and vaporized ion pairs. Effusive sources of ionic liquid vapors[27-28, 32, 53] impart substantial internal energy to the ion pair upon vaporization which can facilitate dissociation.

In this section, a combination of mass spectrometric techniques is used to evaluate the gas phase decomposition products upon heating the aprotic ionic liquid 1-ethyl-3-methylimidazolium bromide ($EMIM^+Br^-$). The high sensitivity of vacuum ultraviolet photoionization time-of-flight

mass spectrometry (VUV PI-TOFMS) enables the detection of thermal decomposition products well below the thermal decomposition onset temperature determined via differential scanning calorimetry (DSC) and thermal gravimetric analysis (TGA). The results from the TGA-MS experiments complement the VUV PI-TOFMS data and give a better understanding of the underlying processes and chemistry involved when heating $EMIM^+Br^-$. Accompanying *ab initio* calculations support the proposed decomposition mechanism by enabling the determination of possible photoion fragmentation pathways and gas phase heats of formation. The calculated gas phase enthalpies of formation in conjunction with enthalpies of vaporization determined by molecular dynamics simulations allow for estimation of heats of formation of ionic liquids in the liquid phase, a valuable but difficult to determine property of ionic liquids. Enthalpy of vaporization and enthalpy of formation values determined here are consistent with previously reported values[110] for $Bmim^+Br^-$ and further support this thermal decomposition mechanism.

5.3.2 Experimental Methods

$EMIM^+Br^-$ was purchased from Fluka (certified purity = 99.6%, water = 0.27%), and was used without further purification. DSC measurements were carried out on a TA Instruments DSC 2010 apparatus with a typical sample mass of 5 mg at a heating rate of 2 K/min in sealed aluminum pans with a nitrogen flow rate of 20 mL/min. The reference sample was an empty Al container, which was sealed under nitrogen atmosphere. Temperatures are determined to (±1 K with a previously calibrated thermocouple.

TGA-MS was carried out on a TA Instruments Q500 apparatus with an electron impact ionization energy of 70 eV. An ionic liquid sample of approximately 5 mg was analyzed under N_2 (10 mL/min) at 473 K for 1 h, followed by increasing the temperature at a rate of 5 K/min up to 643 K. The capillary tube between the TGA unit and the mass spectrometer was held constant at 473 K.

The VUV-PI-TOFMS experiments were performed at the Chemical Dynamics beamline 9.0.2.3 at the Advanced Light Source synchrotron facility at the Lawrence Berkeley National Laboratory, Berkeley, CA. Details of the experiment and the effusive source have been described previously.[28, 53] Briefly, photoionization mass spectra were measured from 8.0 to 15.0 eV in 0.2 eV steps at 457 K (Figure 5.13). At each energy the spectrum was averaged over 500,000 pulses of the ion repeller.

Ab initio calculations were carried out at the DFT (utilizing the B3LYP and M06[120] functionals), MP2, and CCSD(T) levels of theory using the 6-31+G(d,p) basis set. Enthalpies of activation and reaction were refined at the M06 and CCSD(T) levels with the more flexible augmented correlation-consistent polarized valence triple-ζ (aug-cc-pvtz) basis set. All MP2 and CCSD(T) calculations described above were performed using GAMESS,[101-102] and the DFT computations were performed using Gaussian09.[100] Furthermore, gas phase enthalpies of formation of selected species were computed at the G454 level of theory using Gaussian09.[141] All calculated results are at 298 K and include zero point vibrational energy (ZPVE) corrections, unless otherwise stated. While B3LYP did not provide sufficient accuracy for these systems, MP2 and M06

methods provided accurate results when compared to similar bromine-containing species with known enthalpies of formation. M06 resulted in comparable accuracy to MP2 for these systems with significantly reduced computational cost.

MD simulations were performed using a polarizable force field, APPLE&P,[142] which was extended to include a description of the Br anion. MD simulations of bulk $BMIM^+Br^-$ and $EMIM^+Br^-$ ILs have been conducted at the desired temperatures and at atmospheric pressure. Each system contained 150 ionic pairs. MD simulations were conducted using the molecular simulation package Lucretius, which has the capability to handle polarization effects. Covalent bond lengths were constrained using the velocity-Verlet form of the SHAKE algorithm. The Ewald summation method was used for treatment of long-range electrostatic forces between partial atomic charges and between partial charges and induced dipoles. A tapering function was used to drive the induced dipole/induced dipole interactions to zero at the cutoff of 10 Å, with scaling starting at 9.3 Å. Induced dipoles were calculated via a direct iteration with a predictor corrector method. A cutoff of 10 Å was used for all van der Waals interactions and the real part of electrostatic interactions in the Ewald summation. A multiple time step reversible reference system propagator algorithm58 was employed. A time step of 0.5 fs was used for bonding, bending, dihedral, and out-of-plane deformation motions, while a 1.5 fs time step was used for nonbonded interactions within a cutoff radius of 6.0 Å. Finally, the nonbonded interactions in the range between 6.0 Å and 10.0 Å and reciprocal part of electrostatic interactions were updated every 3 fs. Each system was initially equilibrated in the NPT ensemble for at least 1 ns, while production runs were over 5 ns. To calculate the enthalpy of vaporization, an ensemble of 150 ion pairs in the gas phase has been simulated using Brownian dynamics simulations. In these simulations, ions in a given (predefined) pair were allowed to interact only with each other, while any interactions with other ion pairs were turned off. All non- bonded interactions (van der Waals and electrostatic) were directly calculated for all possible pairwise interactions without any cutoff radius. Polarization effects were calculated taking into account only the electrostatic field created by the ionic pair. The duration of these simulations was over 1 ns allowing accurate sampling of the total energy per ion pair in the gas phase.

5.3.3 Results

Differential Scanning Calorimetry

In order to evaluate the thermal decomposition onset temperature for the ionic liquid in this study, differential scanning calorimetry (DSC) was carried out (Figure 5.11). For $EMIM^+Br^-$, melting occurs between 320 K and 340 K, which is slightly lower than the literature value (349.9 K), and this melting point depression is likely due to impurities and a small amount of absorbed water present. The decomposition is exothermic, indicated by a positive peak from 585 K to 640 K. The jagged features in the DSC curve are probably a result of the sealed aluminum sample holder bursting from the increase in pressure upon decomposition; this feature was reproducible even with very small samples, and damage to the DSC sample containers was observed after the experiments. The onset thermal decomposition temperature, T_{dec}, for $EMIM^+Br^-$, reported as the initial nonzero slope of the DSC curves, is 585 K. It should be noted that for the VUV-PI-

TOFMS experiments, temperatures well below this apparent onset decomposition temperature were chosen to look for possible vaporization of the ionic liquid (T=457 K, 510 K, 560 K). However, the slight increase in the DSC heating curve beginning at around 450 K could indicate that a small amount of thermal decomposition occurs well below T_{dec}.

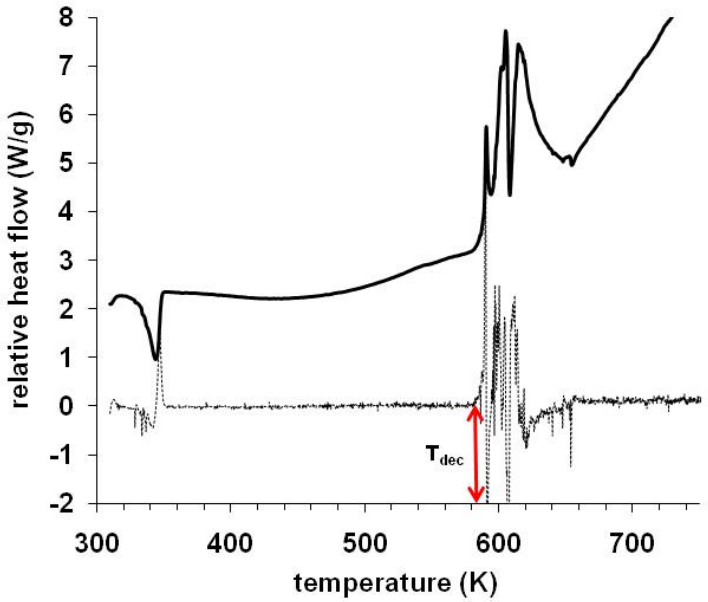

Figure 5.11. Differential scanning calorimetry (DSC) curve for 1-ethyl-3-methylimidazolium bromide ionic liquid (solid line). Dotted line is the slope of the DSC curve. T_{dec} = 585 K.

Thermal Gravimetric Analysis: Mass Spectrometry

In an effort to understand the gas phase species evolved from the heated ionic liquid as a function of temperature, thermal gravimetric analysis mass spectrometry (TGA-MS) measurements were performed. Typical results for $EMIM^+Br^-$ are presented in Figure 5.12. In Figure 5.12(a), the major product peaks detected are at masses (amu/q) 94($CH_3{}^{79}Br$), 96($CH_3{}^{81}Br$), 108($CH_3CH_2{}^{79}Br$), and 110($CH_3CH_2{}^{81}Br$), and their temperature profiles can be seen in Figure 5.12(b). These masses are seen at all temperatures (473-643 K). Their relative mass intensities do not change significantly with increasing temperature, indicating that thermal decomposition occurs even at 473 K, which is well below the thermal decomposition onset temperature indicated in the DSC (T_{dec}=585 K, Figure 5.11).

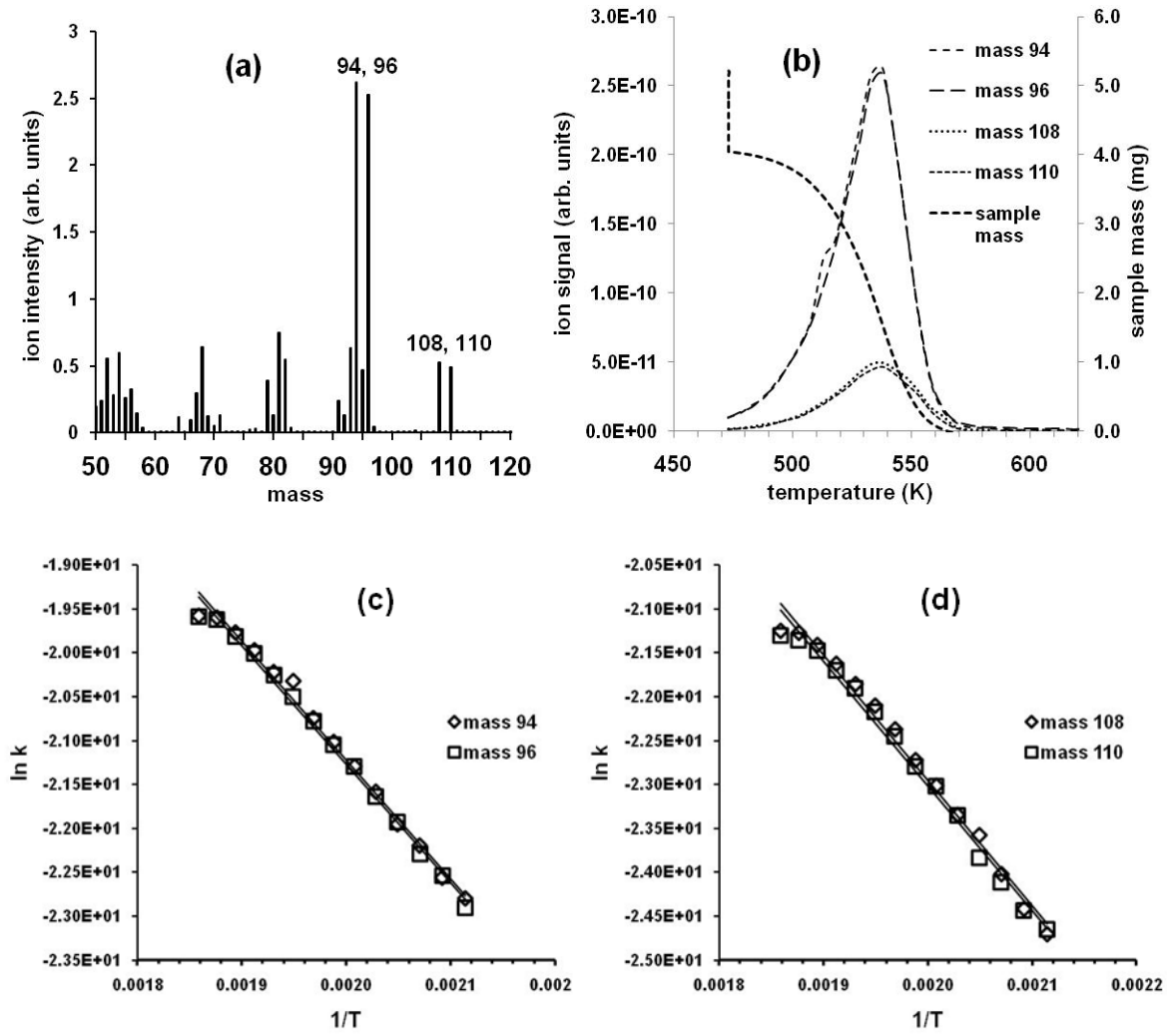

Figure 5.12. (a) TGA-MS data of $EMIM^+Br^-$ averaged over 60 minutes at 473 K. (b) TGA-MS data of $EMIM^+Br^-$ and for masses 94, 96, 108, and 110 as a function of temperature. The isotherm at 473 K is represented by the vertical dashed line. (c) Arrhenius plot for determination of E_a for the formation of CH_3Br. (d) Arrhenius plot for determination of E_a for the formation of C_2H_5Br.

VUV-PI-TOFMS

The mass spectra as a function of photon energy are shown in Figure 5.13 (T = 457 K), and the appearance energies (AE) of the photoions are presented in Table 5.5. No signals were detected that correspond to either the ion pair (masses 190 and 192 for $EMIM^+ {}^{79}Br^-$ and $EMIM^+ {}^{81}Br^-$, respectively) or the intact $EMIM^+$ cation (mass 111). Also absent from the mass spectra is mass 79, corresponding to $^{79}Br^+$. It should be noted that the $EMIM^+$ cation has been detected on the same apparatus under similar conditions previously with the ionic liquid 1-ethyl-3-methylimidazolium bistrifluorosulfonylamide.[143]

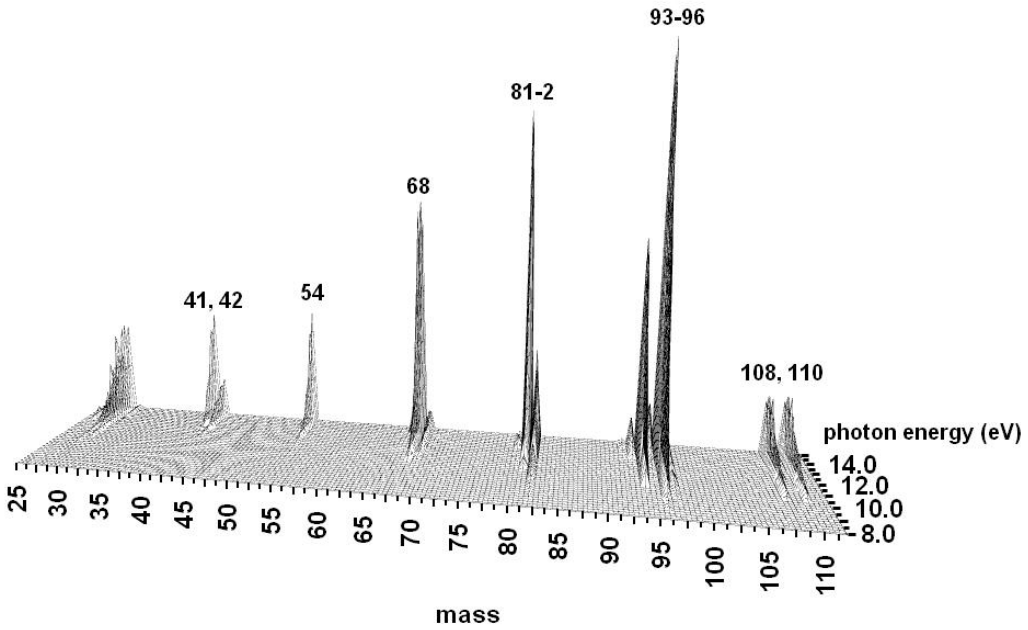

Figure 5.13. VUV PI-TOFMS results for heated $EMIM^+Br^-$ ionic liquid in an effusive source, with source temperature T=457 K. Photoion appearance energies are listed in Table 5.1.

Table 5.5. VUV photoion appearance energies (in eV, ±0.2 eV) for the gaseous products when 1-ethyl-3-methylimidazolium bromide is heated to 457 K.

Mass	**41**	**42**	**54**	**68**	**81**	**82**	**94**	**96**	**108**	**110**
Appearance Energy	12.7	12.0	11.9	10.9	11.1	8.6	10.5	8.5	10.3	10.3

5.3.4 Discussion

Previous studies on aprotic imidazolium-based ionic liquids indicate their vaporization to intact C^+A^- ion pairs, based on the mass spectrometric detection of the intact cation, presumably following the dissociative ionization of the intact ion pair:

$$C^+A^- + h\nu \rightarrow C^+A + e^- \rightarrow C^+ + A\cdot + e^- \qquad (5.15)$$

Even though the temperatures selected for the VUV PI-TOFMS experiments were well below the apparent onset decomposition temperature from the DSC (T_{dec}=585 K, 5.11), a strong photoion signal was obtained in which signal corresponding to the cation resulting from the dissociative ionization of the ion pair ($EMIM^+$, mass 111) was noticeably absent. However, prominent peaks at 94, 96, 108 and 110 were observed. In order to determine if these peaks were a result of dissociative photoionization of the $EMIM^+Br^-$ ion pair, *ab initio* calculations were

performed at the MP2/6-31+G(d,p) level of theory to calculate the appearance energies in the photofragmentation of the anticipated ion pair (Figure 5.14). It was found that, within the expected uncertainties, these AEs are calculated to occur at approximately the same AE values that occur in the experiment. However, the MP2 calculated appearance energy for the EMIM cation at mass 111 is 6.8 ± 0.1 eV (Figure 5.14) and m/z 111 is not seen experimentally, which would suggest the presence of gaseous ion pairs is negligible under the experimental conditions.

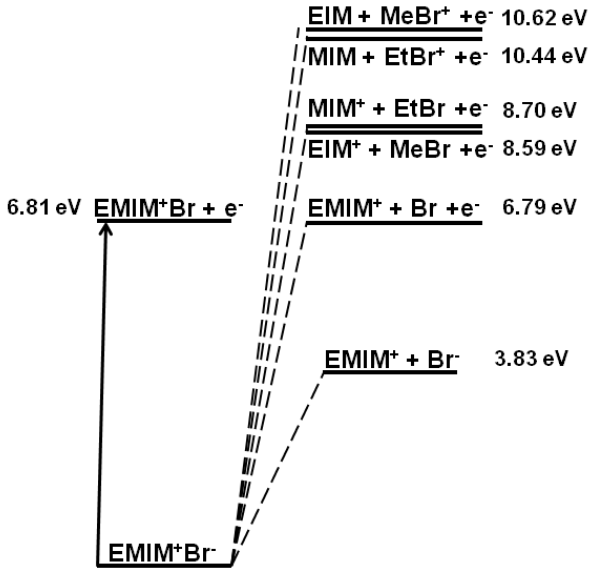

Figure 5.14. Energetics of the possible dissociative photoionization of $EMIM^+Br^-$. Stationary points are calculated at the MP2/6-31+G(d,p) level of theory (0 K, ZPVE corrected).

Ultimately, by comparing not only the experimental appearance energies of the photoions to literature values of possible neutral species, but by also comparing their corresponding photoionization efficiency (PIE) curves to available literature PIE curves and photoelectron spectroscopy data, it is possible to identify the source of the photoions in the experiments.

One beneficial aspect of the bromine system is that there are two isotopes of bromine: ^{79}Br and ^{81}Br, with natural isotope abundances of 50.69% and 49.31% respectively. The appearance of m/z 108 and 110 with identical ion appearance energies and PIE curve shapes, with a 1:1 ion signal ratio would indicate that these species have a bromine atom incorporated, and likely correspond to the $C_2H_5Br^+$ ion. When our low resolution PIE curves for masses 108 and 110 are compared to high resolution experimental total PIE data of ethyl bromide[144] (Figure 5.15), not only are the photoion appearance energies equal (10.3 eV), but the features of the PIE curves match as well, strongly indicating that the photoion masses 108 and 110 originate from the presence of ethyl bromide in the gas phase, and not from the dissociative photoionization of gaseous $EMIM^+Br^-$ ion pairs.

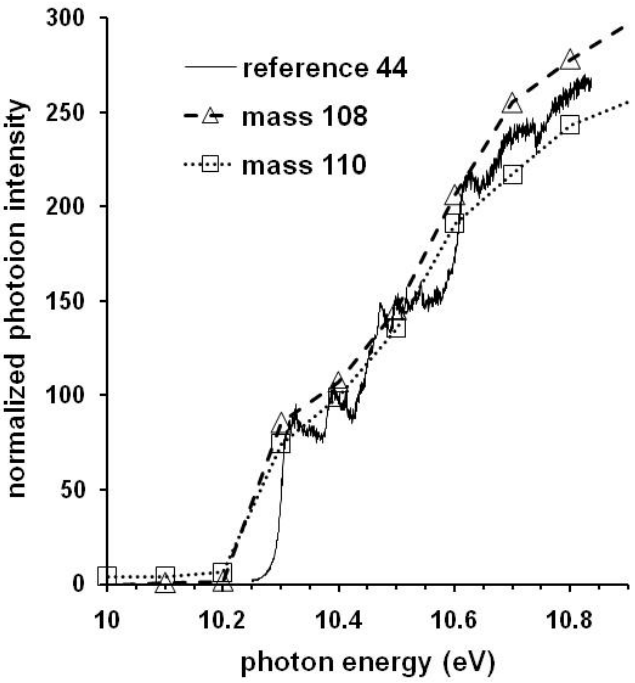

Figure 5.15. Photoionization efficiency (PIE) curves for m/z 108 ($C_2H_5{}^{79}Br^+$) and mass 110 ($C_2H_5{}^{81}Br^+$). Solid curve is total PIE data for C_2H_5Br from reference 144 (reproduced with permission of The Royal Society of Chemistry).

A similar analysis has been performed for the possibility of generating methyl bromide from the condensed phase heating of the $EMIM^+Br^-$ ionic liquid. In this case, the corresponding masses for $CH_3{}^{79,81}Br$ would be 94 and 96. However, in Figure 5.13 the signal from m/z 96 is almost twice the intensity for m/z 94, and this is likely due to the contribution from two different photoions to the m/z 96 signal, $CH_3{}^{81}Br^+$ and the ethylimidazolium cation, the origin of which will be discussed below. These features are very similar to previous mass spectra generated by rapid thermolysis/mass spectrometric experiments on $EMIM^+Br^-$.[132] In comparison of the experimental PIE curve to the literature PIE of methyl bromide,[145] the appearance energies are equal (10.5 eV), the features of both curves match quite well (Figure 5.16(a)), and the derivative of the experimental PIE curve correlates with features in the literature photoelectron spectroscopy data[145] for CH_3Br (not shown). In addition, the PIE curves for the fragment ion, CH_2Br^+ (m/z 93 and m/z 95), have the same AEs (13.0 eV) and the curves match almost exactly (Figure 5.16(b)).

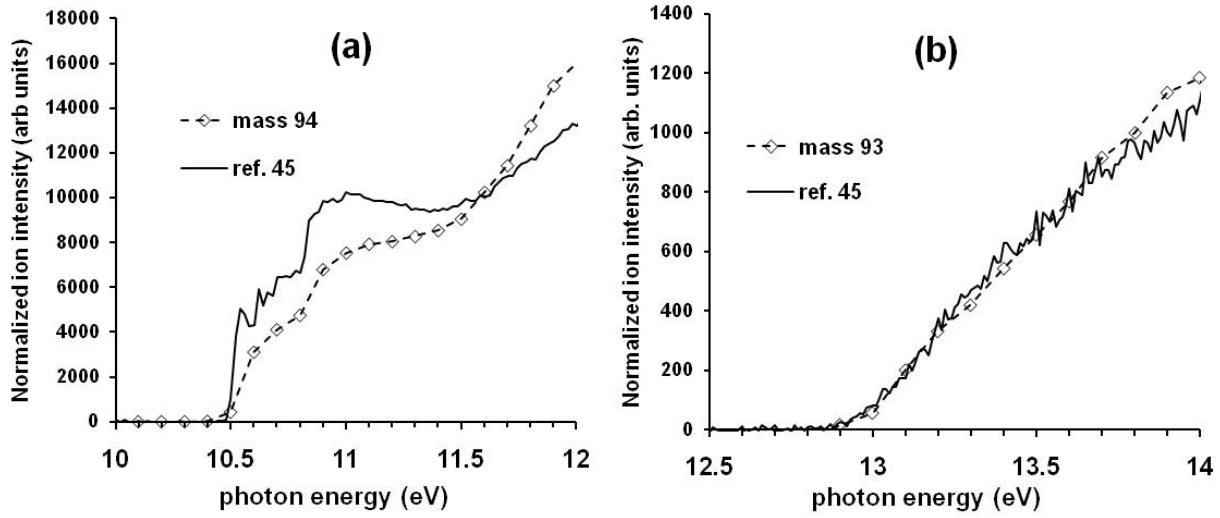

Figure 5.16. (a) Experimental PIE data for mass 94 ($CH_3{}^{79}Br^+$) and (b) experimental PIE curve for mass 93 ($CH_2{}^{79}Br^+$). Solid curves are total PIE data for CH_3Br from reference 45 (reproduced with permission from Elsevier).

If methyl bromide and ethyl bromide are being formed by thermolysis in the heated ionic liquid, the condensed phase reactions involved would likely be:

$$EMIM^+Br^- \xrightarrow{\Delta} CH_3Br + EIM \quad (5.16)$$

$$EMIM^+Br^- \xrightarrow{\Delta} CH_3CH_2Br + MIM \quad (5.17)$$

where MIM is 1-methylimidazole (MW=82), and EIM is 1-ethylimidazole (MW=96). The measured AEs of photoion m/z 82 (8.6 ± 0.2 eV) and 96 (8.5 ± 0.2 eV) match well with the MP2/6-31+G(d,p) calculated ionization potentials for MIM and EIM (8.66 ± 0.1 and 8.59 ± 0.1 eV), respectively, as well as with the NIST WEBBOOK[146] database value for MIM (8.66 eV). Assuming that the contribution from $CH_3{}^{81}Br$ to the mass 96 PIE curve is similar in strength to the PIE for $CH_3{}^{79}Br$, the experimental EIM^+ PIE curve can be obtained simply by subtracting the PIE of m/z 94 ($CH_3{}^{79}Br$) from the observed PIE of m/z 96 (Figure 5.17), resulting in an experimental ionization energy for EIM of 8.5 ± 0.2 eV. From the measured AE of mass 94 ($CH_3{}^{79}Br$), the AE of $CH_3{}^{81}Br$ of 10.5 ± 0.2 eV can be assumed (literature value for CH_3Br: IP = 10.54[147]).

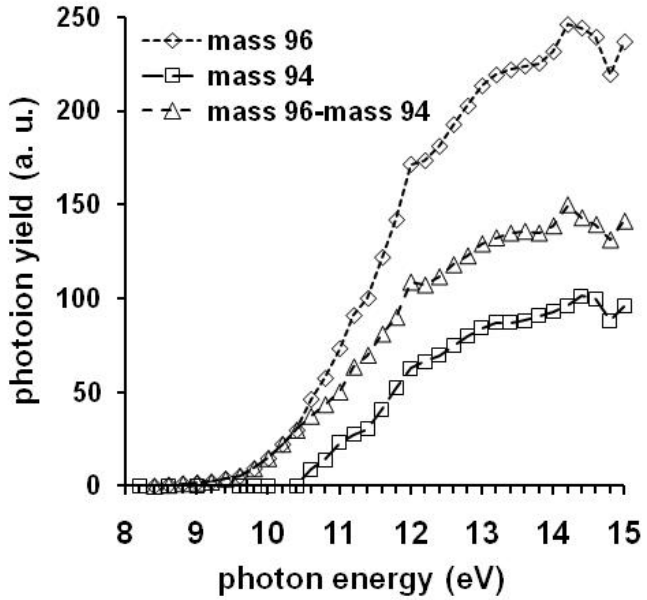

Figure 5.17. PIE curves for m/z 94 and m/z 96. Triangles are the difference of mass 96 and mass 94 PIE curves, and represents the PIE curve for EIM^+.

The lower ion masses between 40-81 are dissociative fragments mainly of EIM with a small contribution from fragmentation of MIM, and their formation will be discussed below. Ion masses 26-30 are a combination of dissociative fragments from CH_3CH_2Br, MIM, and EIM, and their formation will not be discussed here. Mass 81 (AE = 11.1±0.2 eV) cannot be from $^{81}Br^+$, not only because there would be a comparable isotopic signal at mass 79 from $^{79}Br^+$, which is completely absent in Figure 5.13, but the $^{81}Br^+$ photoion appearance energy from CH_3Br is >15 eV.[145] Rather, the mass 81 peak could be from either dissociative photoionization of MIM or of EIM as shown in Scheme 5.1.

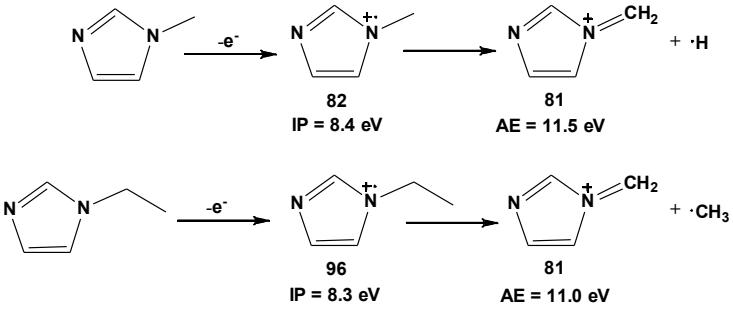

Scheme 5.1

From the M06 calculated appearance energies for these two photofragments of 11.5±0.2 and 11.0±0.2 eV, respectively, the experimental appearance energy of 11.1±0.2 eV indicates that mass 81 more likely results from the latter (5.1.2) fragmentation channel. The relative formation of $H^{79}Br$ (and the corresponding EMIM carbene, EMIM:) is negligible, as mass 80 is less than 1% of mass 82. This is consistent with calculations at the MP2/6-31+G(d,p) level, which show that (a) separated HBr + EMIM: is less stable than the $EMIM^+Br^-$ ion pair by 1.31 eV and (b)

proton transfer occurs from HBr to EMIM: to form the $EMIM^+Br^-$ ion pair occurs without an energy barrier. Mass 68 (AE = 10.9 ± 0.2 eV) likely comes from EIM^+ fragmentation to form the imidazolium cation and the thermodynamically stable C_2H_4, a rather common ion fragmentation mechanism.[148] Although the calculated M06 energies (Scheme 5.2) for mass 68 ion formation do not match the experimental value exactly, the closest energy pathway is the hydrogen transfer from the ethyl CH_3 to C4 on the imidazolium ring, followed by elimination of C_2H_4 with a calculated AE = 11.5 eV.

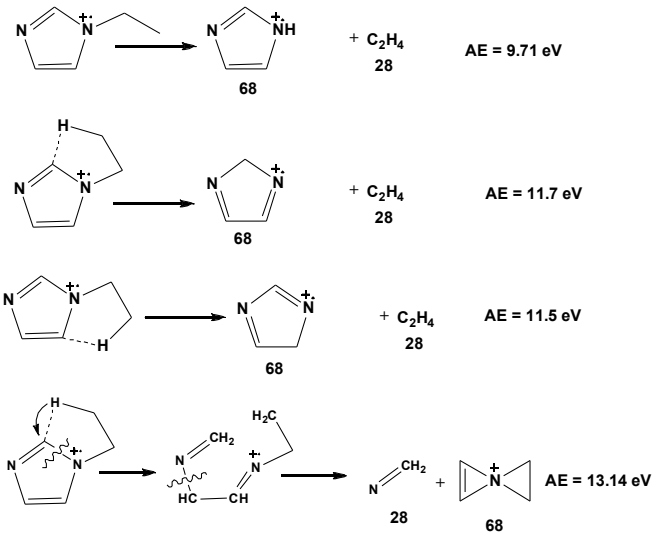

Scheme 5.2

Another possibility is that the pathway leading to ethylene plus imidazolium ion via hydrogen transfer from the methyl group to N1 (N1-ethyl) has a high barrier due to a strained geometry in the transition state, which could raise the AE above 9.74 eV. The pathway leading to formation of mass 68 ion plus CNH_2 was also considered, but the energetics are prohibitively high for this channel (AE = 13.1 eV, Scheme 5.2). The formation of mass 68 from MIM would involve the elimination of a CH_2 radical, which is highly energetically unfavorable (AE=13.2 eV):

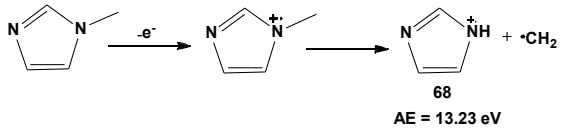

Also, from the literature, the electron impact ionization mass spectrum of EIM shows a mass 68 fragment whereas that of MIM does not, even at 70 eV ionization energy.[146]

Hydrogen transfer followed by ring opening fragmentation pathways will lead to masses 54(AE = 11.9±0.2 eV) and 42(AE = 12.0±0.2 eV). Ring opening without hydrogen transfer would lead to ion masses not observed in the experiment. While ring opening to form mass 54 can only occur from EIM, mass 42 can form from possible ring opening of both EIM and MIM. To evaluate the fragmentation of EIM^+ (m/z 96, $C_5N_2H_8$) to form mass 42 (C_2NH_4) and mass 54 (C_3NH_4), the heats of formation of the fragments with different possible structures, both neutrals and cations, were calculated at the M06/6-31+G(d,p) level of theory. The heats of formation of

eight possible structures for mass 42 and 16 possible structures for mass 54 were evaluated, the appearance energies of each combination of cation and neutral fragments were calculated, and the fragmentation pathways within ±0.5 eV of the experimental AEs were evaluated further, resulting in nine pathways in this AE range for mass 54 cations and 26 pathways for mass 42 cations. From this analysis, the most likely pathways were determined (Scheme 5.3) by matching theoretical AEs to experimental AEs and looking for the most reasonable geometries resulting from fragmentation of EIM^+. Formation of the mass 42 and mass 54 fragments from the EIM^+ parent must involve a hydrogen transfer followed by two ring bond cleavages. The hydrogen transfer can come from the terminal methyl group on the ethyl to the C2 position on the imidazolium ring. The calculated M06 energies are in good agreement with the experimental AEs for this pathway. Mass 42 could possibly result from fragmentation of MIM to form mass 40 plus mass 42 (Scheme 5.3). However, the calculated AE for mass 42 is 12.7 eV, which doesn't match with the experimental result for the m/z 42 AE (12.0 eV).

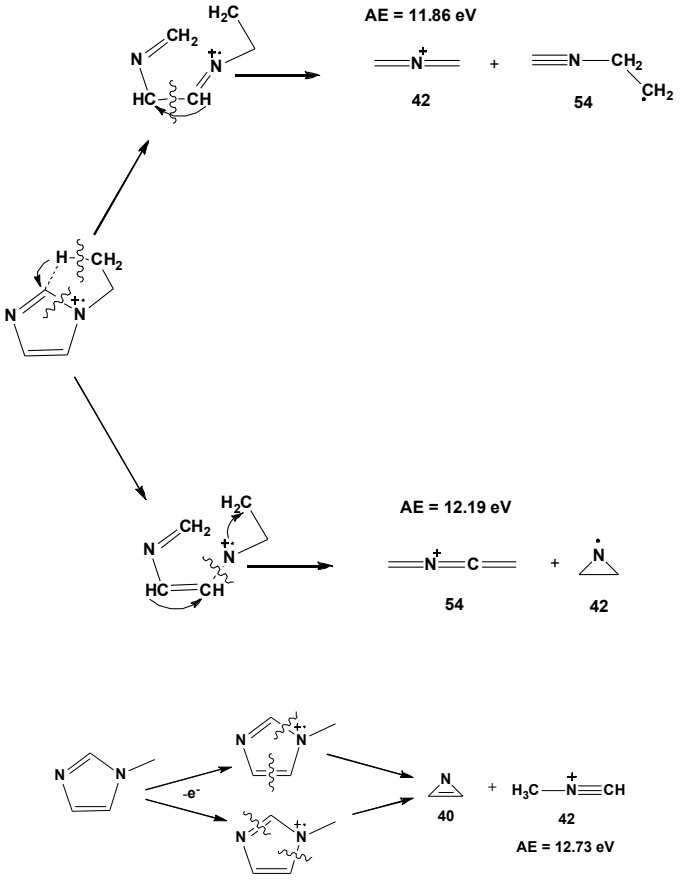

Scheme 5.3

M/z 41 could result from MIM fragmentation involving hydrogen transfer followed by ring cleavage to form two m/z 41 fragments, and the calculated AE for the second pathway in Scheme 5.4 agrees very well with the experimental AE.

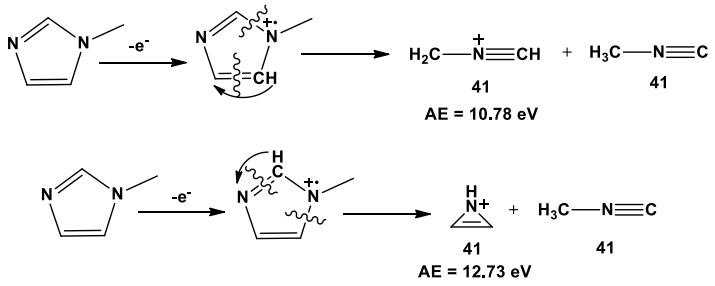

Scheme 5.4

Assuming the rates of evaporation of CH_3Br (BP = 277 K,[146] ΔH^o_{vap} = 23.24 kJ/mol[146]) and CH_3CH_2Br (BP = 312 K,[146] ΔH^o_{vap} = 28.26 kJ/mol[146]) are much faster than the reaction rates of their formation at T = 454 K through reactions 5.16 and 5.17, the branching ratio between reactions 5.16 and 5.17 above can be calculated simply by comparing the ion counts (Figure 5.13) for methyl bromide versus ethyl bromide. To quantify the ethyl bromide reaction, the mass 108 and mass 110 photoion signals were summed over all photon energies and added together. To quantify the methyl bromide reaction, the mass 94 photoion signal was summed over all photon energies and multiplied by two in order to include the contribution from $CH_3{}^{81}Br$ (mass 96). At T = 454 K, the calculated branching ratio for CH_3Br: C_2H_5Br is 0.76:0.24.

Previous TGA-MS/DSC studies have suggested that significant mass loss can occur well below the thermal decomposition onset temperature.[130, 149] In Figure 5.12(b), the isothermal portion of the TGA curve at T=473 K indicates that >20% of the sample mass is lost in one hour, while the DSC does not indicate that any reaction takes place until almost 600 K. By making an Arrhenius plot with the natural log of the rate of product formation (ion signal intensity divided by temperature ramp rate, 5 K/min) versus 1/T (Figure 5.12(c)-(d)), the slope of the plot corresponds to $-\Delta H^{\ddagger}/R$ for the thermal decomposition. These activation enthalpies for m/z 94, 96, 108 and 110 yield 112.1±6.6 kJ/mol and 118.4±7.2 kJ/mol for reactions 5.16 and 5.17, respectively, which are consistent with the VUV-PI-TOFMS branching ratio results reported above. Uncertainties in the experimental activation energies are the 95% confidence limits (±2σ, precision) determined by the linear least squares fit of the experimental data in Figures 5.12(c) and 5.12(d). Since the activation enthalpies for thermal decomposition to CH_3Br and C_2H_5Br are almost 5 times the enthalpies of vaporization for CH_3Br and C_2H_5Br, the assumption that vaporization occurs much more rapidly than thermal decomposition seems reasonable.

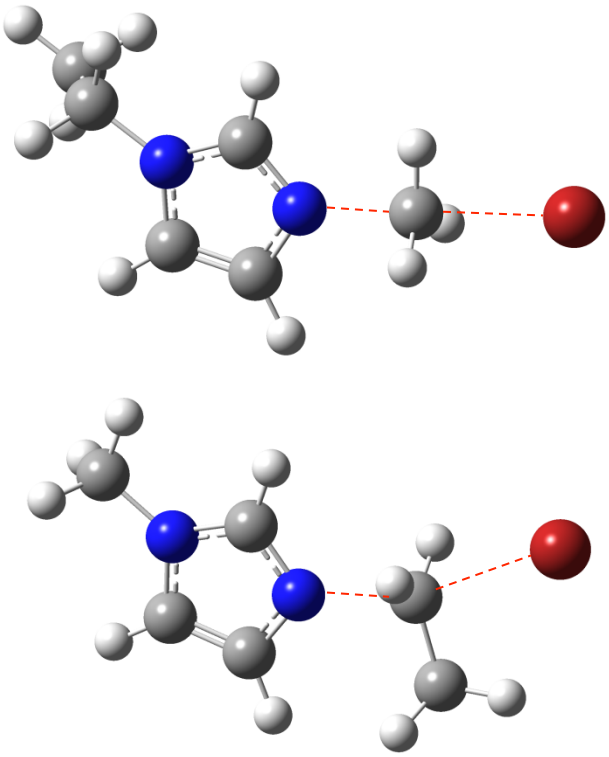

Figure 5.18. Transition states for the S_N2 alkyl abstraction of methyl (top) and ethyl (bottom) by the bromide ion at the M06/6-31+G(d,p) level of theory.

Ab initio calculations were performed to determine if the reactions 5.16 and 5.17 proceed via a bond insertion or via an S_N2 type mechanism. Transition states for Br^- to insert into the N-C bond of the methyl and ethyl side chains were located and their activation barriers were calculated. The transition states were confirmed by frequency calculations resulting in a single imaginary frequency, and intrisic reaction coordinate (IRC) calculations confirmed that the products are CH_3Br + EIM (reaction 5.16) or CH_3CH_2Br + MIM (reaction 5.17). The calculated activation barriers via bond insertion for reactions 5.16 and 5.17 are 239.3 kJ/mol and 212.1 kJ/mol, respectively (at M06/6-31+G(d,p) level of theory). Not only are these barriers prohibitively high, but also reaction 5.17 would be favored on energetic grounds, contrary to what is observed experimentally. However, for the S_N2 reactions, the transition state enthalpies and reaction enthalpies are in good agreement with experimental results. The activation enthalpies ($\Delta H^{\ddagger}$) and enthalpies of reaction (ΔH_{rxn}, 298K) for reactions 5.16 and 5.17 at several levels of theory can be seen in Table 5.6. The increased activation barrier for reaction 5.17 can be explained by steric factors, seen in Figure 5.18. The transition state for reaction 5.16 has a linear N-C-Br geometry with a near planar CH_3 group, and a C-Br distance of 2.55 Å at the M06/6-31+G(d,p) level of theory. The transition state for reaction 5.17 shows repulsion between the ethyl CH_3 group and the incoming Br^-, which causes a bend in the N-C-Br angle away from linearity, and the C-Br distance elongates to 2.65 Å, which is consistent with the presence of higher steric strain relative to the transition state for reaction 5.16. Increasing the basis set to aug-cc-pvtz only decreases the C-Br distance by 0.02 Å to 2.63 Å, therefore the moderate size of

the 6-31+G(d,p) basis set is appropriate to accurately describe the transition state geometry for reaction 5.17. The decrease in magnitude of E_a values from theory to experiment is likely due to solvent stabilization effects in the condensed phase relative to the gas phase, where the ionic liquid solvent lowers the energy of the transition state more than it does for the reactant.

Table 5.6. Calculated Reaction Enthalpies (298 K, kJ/mol) for Reactions 5.16 and 5.17[a]

reaction 2	activation enthalpy, $\Delta H^{\ddagger}$	ΔH_{rxn}
MP2/6-31+G(d,p)	n/a	23.1
M06/6-31+G(d,p)	134.0	15.4
CCSD(T)/6-31+G(d,p)//M06/6-31+G(d,p)	137.3	28.1
M06/aug-cc-pvtz	136.0	16.5
CCSD(T)/aug-cc-pvtz//M06/aug-cc-pvtz	130.3	21.3
reaction 3	activation enthalpy, $\Delta H^{\ddagger}$	ΔH_{rxn}
MP2/6-31+G(d,p)	n/a	24.9
M06/6-31+G(d,p)	139.0	16.2
CCSD(T)/6-31+G(d,p)//M06/6-31+G(d,p)	148.6	29.5
M06/aug-cc-pvtz	140.2	17.7
CCSD(T)/aug-cc-pvtz//M06/aug-cc-pvtz	139.9	23.1

[a] Thermal corrections obtained using unscaled harmonic vibrational frequencies.

To determine whether vaporization competes with thermal decomposition under vacuum distillation conditions, it is necessary to estimate the heat of vaporization for $EMIM^+Br^-$. In order to estimate the heat of vaporization of $EMIM^+Br^-$, several approaches were investigated. Recent work by Paulechka and coworkers[110] on the thermochemistry of the formation of 1-butyl-3-methylimidazolium bromide ($BMIM^+Br^-$) determined that the heat of vaporization of $BMIM^+Br^-$ is sufficiently higher than the activation barrier for thermal decomposition such that saturated vapor pressure due to intact $BMIM^+Br^-$ will never be experimentally attainable. Although the enthalpy of formation of halogen containing compounds can be calculated from the enthalpy of combustion, experimental enthalpies of combustion of halogen containing compounds are difficult to determine accurately due to incomplete combustion and the need to accurately identify combustion products. Instead, Paulechka measured the heat of reaction $MIM_{(l)} + BuBr_{(l)} \rightarrow BMIM^+Br^-_{(l)}$ calorimetrically, where BuBr is 1-butylbromide, and they calculated the heat of formation of the ionic liquid from this measurement using known C_p values and heats of formation of MIM and BuBr. By adding the experimentally determined activation energy to the heat of the reaction for: $MIM_{(l)} + BuBr_{(l)} \rightarrow BMIM^+Br^-_{(l)}$, the activation energy for the reverse reaction (thermal decomposition) can be calculated (Figure 5.19). With an activation enthalpy of $\Delta H^{\ddagger} = 73 \pm 4$ kJ/mol (determined over the range of 303-334 K) and ΔH_{rxn} (298 K) = 87.7 ± 1.6 kJ/mol, the resulting activation barrier for the reverse reaction is 161 ± 4

kJ/mol (±2σ). From the experimentally determined enthalpy of formation of $BMIM^+Br^-_{(l)}$ as well as the gas phase enthalpy of formation of the ion pair calculated by quantum chemical methods, the enthalpy of vaporization was determined to be ΔH_{vap} (298 K) = 174 ± 9 kJ/mol. Since the estimated ΔH_{vap} (298 K) = 174 ± 9 kJ/mol is greater than the barrier for the reverse reaction (161 ± 4 kJ/mol), on energetics grounds, thermal decomposition will dominate, and vaporization to ion pairs will not be experimentally detectable.

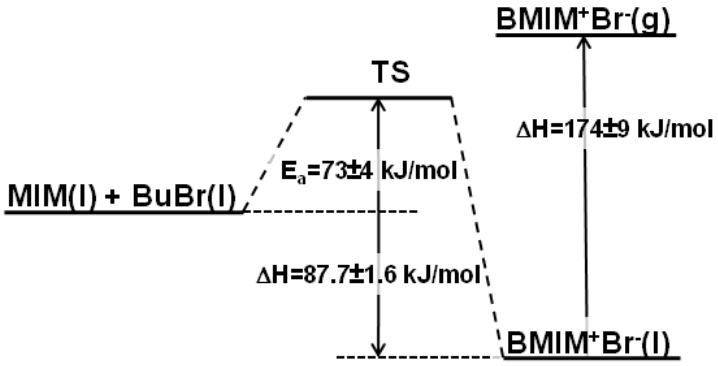

Figure 5.19. Energy diagram for the conversion of $BMIM^+Br^-$ to MIM + BuBr (data used with permission from reference[110]).

An alternate method for determining the enthalpy of formation in the liquid phase of the ionic liquid is to calculate the enthalpy of formation of the ion pair in the gas phase by *ab initio* methods (G4), and to calculate the enthalpy of vaporization of the ionic liquid using molecular dynamics (MD) methods. If the enthalpy of formation of the gaseous ion pair and the enthalpy of vaporization can be calculated, the enthalpy of formation in the liquid phase of the ionic liquid can be calculated as the difference between the gas phase enthalpy of formation and the enthalpy of vaporization (see Figure 5.19). The gas phase enthalpy of formation $\Delta H_{f,\ gas}$(298 K) of $EMIM^+Br^-$ and $BMIM^+Br^-$ at the G4 level of theory are 38.4 ± 10 and −5.6 ± 10 kJ/mol, and the $\Delta H_{f,\ gas}$(298 K) value for $BMIM^+Br^-$ satisfactorily agrees with the literature value of $\Delta H_{f,\ gas}$(298 K) = 16 ± 7 kJ/mol.[110] The uncertainty of the G4 calculations for systems involving bromine were conservatively estimated at ±10 kJ/mol based on a caparison of calculated G4 enthalpies of formation of bromine containing molecules to their known literature values (Table 5.7). The difference in the gas phase heats of formation $\Delta H_{f,\ gas}$(298 K) between $EMIM^+Br^-$ and $BMIM^+Br^-$ of 44.0 kJ/mol is consistent with the general trend of decreasing $\Delta H_{f,\ gas}$(298 K) from C_2MIM to C_4MIM observed recently.[150] Using the value of 38.4 ± 10 kJ/mol for the G4 gas phase enthalpy of formation of $EMIM^+Br^-$ and, at first approximation, assuming the enthalpy of vaporization of $EMIM^+Br^-$ is the same as that of $BMIM^+Br^-$ (174 ± 9 kJ/mol), the enthalpy of formation of $EMIM^+Br^-_{(l)}$ is calculated to be −136 ± 13 kJ/mol at 298 K. To improve on the accuracy of this value, molecular dynamics simulations were carried out to determine the enthalpy of vaporization (ΔH_{vap}) of $EMIM^+Br^-$ and $BMIM^+Br^-$ (Table 5.8).[151] Enthalpies of vaporization at 298 K were determined for $EMIM^+Br^-$ and $BMIM^+Br^-$ by extrapolation from the enthalpies of vaporization determined by molecular dynamics simulations at higher temperatures as indicated in Table 5.8. Molecular dynamics simulations were performed for both $EMIM^+Br^-$ and

$BMIM^+Br^-$ in order to validate the ΔH_{vap} with Paulechka's experimental value for $BMIM^+Br^-$. Comparison of the ΔH_{vap}(298 K) value for $BMIM^+Br^-$ from Table 5.8 (152.8 kJ/mol) with the ΔH_{vap}(298 K) from Paulechka and coworkers (174 kJ/mol) indicates the molecular dynamics value is low by ~14%. Correcting for this observed systematic error would yield an estimate for $EMIM^+Br^-$ ΔH_{vap}(298 K) of 168 ± 20 kJ/mol. Using this value and the G4 gas phase enthalpy of formation of $EMIM^+Br^-$, our best estimate for the enthalpy of formation of $EMIM^+Br^-_{(l)}$ is -130 ± 22 kJ/mol at 298 K. A corresponding result for $BMIM^+Br^-_{(l)}$ yields a ΔH_f value of -180 ± 20 kJ/mol, which is consistent, within reported uncertainties, with that of Paulechka (-158 ± 5 kJ/mol). Similar to the findings for $BMIM^+Br^-$,[110] the ΔH_{vap} value for $EMIM^+Br^-$ at 473 K of 130.8 kJ/mol (uncorrected) is substantially larger than the experimental $\Delta H^‡$ values for thermal decomposition (116.1 and 122.9 kJ/mol for reactions 5.16 and 5.17). Therefore, thermal decomposition effectively dominates the mass loss process for $EMIM^+Br^-$ in our experiments.

Table 5.7. Analysis of uncertainties of the G4 method for bromine-containing systems[a]

	$\Delta H_{f,gas}$ G4 (298 K)	experiment[b]	uncertainty
Br^-	−215.7	−212.7	3.0
HBr	−34.1	−36.3	2.2
CH_3Br	−34.8	−34.3	0.5
CH_3CH_2Br	−62.5	−63.6	1.1

[a] Enthalpies are in kJ/mol. [b] Reference 62.

Table 5.8. Enthalpies of vaporization determined by MD simulations.

	T (K)	ΔH_{vap} (kJ/mol)
$EMIM^+Br^-$	298	147.1[b]
$EMIM^+Br^-$	393	138.3[a]
$EMIM^+Br^-$	473	130.8[a]
$BMIM^+Br^-$	298	152.8[b]
$BMIM^+Br^-$	323	150.5[a]
$BMIM^+Br^-$	393	144.0[a]

[a] MD direct calculation. [b] Linear extrapolation from higher temperature MD values.

5.3.5 Conclusion

The absence of m/z 111 ($EMIM^+$ cation) from the effusive source VUV-PI-TOFMS experiment indicates that vaporization of $EMIM^+Br^-$ as intact ion pairs is not a significant pathway leading to mass loss. Instead, the observed photoions and PIE curves strongly indicate the decomposition of $EMIM^+Br^-$ to CH_3Br, CH_3CH_2Br, MIM and EIM. TGA-MS studies and ab initio calculations support the S_N2 mechanism whereby CH_3Br formation is favored 3 to 1 over CH_3CH_2Br formation due to increased steric hindrance in the transition state for the latter path. From this

work, the best estimates for the enthalpy of formation and the enthalpy of vaporization of $EMIM^{+}Br^{-}$ are $\Delta H_{f,\,liq}(298\ K) = -130 \pm 22$ kJ/mol and $\Delta H_{vap}(298\ K) = 168 \pm 20$ kJ/mol.

▪ Acknowledgement

The authors gratefully acknowledge funding from the U.S. Air Force Office of Scientific Research for supporting SDC and GLV (Grant No. FA9300-06-C-0023), and for CK and SRL (Grant No. FA9550-10-1-0163). This work at the ALS was supported by the Director, Office of Energy Research, Office of Basic Energy Sciences, Chemical Sciences Division of the U.S. Department of Energy under Contract No. DE-AC02-05CH11231 (A.G., O.K., and S.R.L.). We would like to thank Erik Mitchell for obtaining the DSC data, Greg Yandek and Ray Campos for the TGA data, and Wasatch Molecular Inc. for the molecular dynamics ΔHvap data. This work was supported in part by a grant of computer time from the DoD High Performance Computing Modernization Program at the Air Force Research Laboratory, Army Research Laboratory, Engineer Research and Development Center, and Navy Department of Defense Supercomputing Resource Centers (DSRCs).

Chapter 6

Hypergolic ionic liquid aerosols

Hypergolic bipropellants usually consist of a fuel and an oxidizer and the propellants spontaneously ignite when they come into contact with each other. Use of these hypergolic bipropellants eliminates the need for an additional ignition source in rocket engines, spacecraft, and satellites. Today, due to the extreme toxicity and/or corrosiveness of conventional hypergolic propellants, such as monomethyl hydrazine and unsymmetrical dimethylhydrazine, environmental and health concerns are becoming more and more pressing in the propellant world. The volatility of hydrazine and its derivatives, which produce carcinogenic vapor toxins, is a problem for handling these hypergolic propellants; nevertheless they are still the state-of-the-art fuels for bipropellant applications.[20]

The low volatility and environmental friendliness of energetic ionic liquids provide great potential in replacing hydrazine-based propellants with hypergolic ionic liquids. The synthesis of hypergolic ionic liquids has stimulated interest in novel ways to store chemical energy for propulsion in ionic liquids. In 2008, the first hypergolicity of dicyanamide ionic liquids with nitric acid was reported and showed the crical role of the anion inducing hypergolicity. Despite their great performance, the corrosivity, high toxicity and high vapor pressure of nitric acid prevents it from being used to replace the excellent hydrazine-based propellant. More recently, military researchers in the U. S. have recently developed a less corrosive and toxic rocket fuel system using a hydrogen-rich ionic liquid that is hypergolic with hydrogen peroxide as the oxidizer.

To facilitate the search for hypergolic ionic liquids for bipropellant applications, understanding the hypergolic reaction mechanism is critical. As ionic liquids are “designer solvents”, hypergolic ionic liquids can be designed as green rocket propellants based on the understanding of their reaction mechanism. There is little work to investigate hypergolic reaction mechanisms due to the difficulty of probing the highly reactive transient species. The new method for measuring the heterogeneous chemistry using the “aerosol flow tube method” has been proved to be an excellent way to obtain qualitative and quantitative understanding of chemical reactions. Studies of heterogeneous reactions by this method on very low vapor pressure hydrocarbons, e.g. 100 nm squalane liquid aerosol droplets with gaseous OH, are now routinely performed at the beamline 9.0.2.1. In the case of OH + squalane liquid in the presence of oxygen, products showing the substitution of one, two, three, four, etc. oxygens are observed in succession and the kinetics of this multistep process are unraveled for the first time.[152]

Using this “aerosol flow tube method” in conjunction with high-resolution mass spectrometry, the reaction mechanism of dicyanamide ionic liquid with nitric acid was first investigated. For this study, we first configured the system; to nebulize the ionic liquid into fine (100 nm

diameter) aerosol particles, to characterize the intact IL aerosol particles (discussed in section 6.1), to react those IL particles with the oxidizer in a flow tube, and then to observe the products of the heterogeneous reaction using tunable ultraviolet radiation (discussed in section 6.2).

6.1 Soft ionization of thermally evaporated hypergolic ionic liquid aerosols

Isolated ion pairs of a conventional ionic liquid, 1-Ethyl-3-Methyl-Imidazolium Bis(trifluoro-methylsulfonyl)imide ($[Emim^+][Tf_2N^-]$), and a reactive hypergolic ionic liquid, 1-Butyl-3-Methyl-Imidazolium Dicyanamide ($[Bmim^+][Dca^-]$), are generated by vaporizing ionic liquid submicron aerosol particles for the first time; the vaporized species are investigated by dissociative ionization with tunable vacuum ultraviolet (VUV) light, exhibiting clear intact cations, $Emim^+$ and $Bmim^+$, presumably originating from intact ion pairs. Mass spectra of ion pair vapor from an effusive source of the hypergolic ionic liquid show substantial reactive decomposition due to the internal energy of the molecules emanating from the source. Photoionization efficiency curves in the near threshold ionization region of isolated ion pairs of $[Emim^+][Tf_2N^-]$ ionic liquid vapor are compared for an aerosol source and an effusive source, revealing changes in the appearance energy due to the amount of internal energy in the ion pairs. The aerosol source has a shift to higher threshold energy (~0.3 eV), attributed to reduced internal energy of the isolated ion pairs. The method of ionic liquid submicron aerosol particle vaporization, for reactive ionic liquids such as hypergolic species, is a convenient, thermally "cooler" source of isolated intact ion pairs in the gas phase compared to effusive sources.

6.1.1 Introduction

Ionic liquids (ILs) are ambient temperature molten salts[1] with fascinating properties, including extremely low volatility, tunable chemical properties, and distinctive reactivity.[6, 17-18, 44-50] The unique properties of ILs are a direct result of the interactions between the ions[153-154] and this led to an explosion of interest to utilize ILs for broad applications such as catalysts,[15] batteries,[16-18] and hypergolic fuels.[20, 23-24, 51] Some energetic ionic liquids, the dicyanamide,[23] nitrocyanamide,[51] and azide systems,[24] have shown promising potential for propellant applications,[20] as substitutes for conventional energetic compounds, monomethyl hydrazine/nitrogen tetroxide (MMH/NTO), with several advantages including thermal stability, environmental friendliness, and low volatility. For the task-specific use of ILs, they can be designed accordingly by varying the choices of the cation-anion combinations. Physicochemical properties of ILs change dramatically based on the constituents, and Plechkova and Seddon[21] estimate that possible ion pairings can be as many as 10^{18}. This vast number of possible combinations makes it almost impossible to test all available ILs for specific applications. It is therefore valuable to understand in greater depth

the fundamental properties of the isolated ion-pairs and to extrapolate and predict the features of ILs.

Recent studies[8, 27-29, 34-35, 52-58] show that isolated ion-pairs can be prepared in the gas phase by thermal vaporization of ILs despite their extremely low vapor pressure. Earle and collaborators[26] reported in 2006 that intact cations (C^+) and anions (A^-) associated in the vapor are produced by vaporization, and this result initiated multiple studies that investigate the vaporization mechanism and the nature of IL vapor.[8, 27-29, 34-35, 52-54, 57] Various experimental methods, such as soft ionization mass spectrometry,[28, 53] line-of-sight mass spectrometry,[29, 56] UV spectroscopy[34] and cryogenic neon matrix-isolation FTIR spectroscopy,[52] provide direct evidence for the existence of vaporized ion pairs in the form of cation-anion 1:1 pairs. Ionization of these vaporized ion pairs by photons or electrons often produces intact cations (C^+) as a result of dissociative ionization (equation (1.1)).

Intact cations are observed whether the origin of the ion pair vapor is a bulk sample or a thin film heated for the vaporization. However, highly reactive ionic liquids show dissociative ionization as well as decomposition, and it becomes difficult to identify the intact cation signal and to distinguish thermal decomposition from fragmentation of ion pairs upon ionization. This makes it nearly impossible to study reaction mechanisms and kinetics of hypergolic ionic liquids because of the difficulty of detecting small changes in their complicated mass spectra.

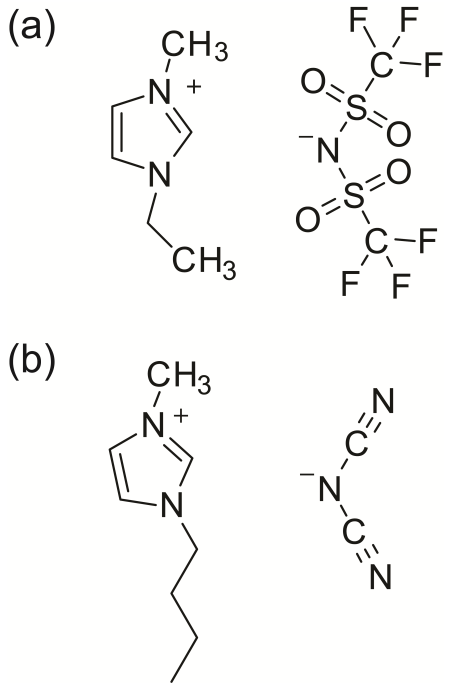

Figure 6.1. Schematic molecular structure drawings of ionic liquid, (a) 1-ethyl-3-methyl-imidazolium ([Emim$^+$]) bis(trifluoromethylsulfonyl)imide ([Tf_2N^-]), [Emim$^+$][Tf_2N^-], and (b) 1-butyl-3-methyl-imidazolium ([Bmim$^+$]) dicyanamide ([Dca^-]), [Bmim$^+$][Dca^-].

Typically ions with high internal energies fragment extensively producing a mass spectrum that contains a wide variety of abundant fragment ions.[155] The internal energy content of the

molecular ion (M^+) is from two sources: the thermal energy from evaporation and the energy imparted by the ionization process. Molecular ions (M^+) of labile molecules can only be detected if the internal energy of the molecular ion is kept very low, by obtaining mass spectra with low photon energies and low temperatures. Aerosol particle generation[43, 152, 156-159] has previously been demonstrated as a new way to introduce fragile biomolecules into the gas phase with nearly fragmentation-free mass spectra by minimizing their internal energy imparted into the molecular ion in gas phase. We apply this new method to hypergolic IL studies, to produce isolated ion pairs in the gas phase from IL aerosol particles followed by thermal vaporization, and monitor the ion pair vapor by soft ionization using tunable vacuum ultraviolet (VUV) photoionization mass spectrometry. This report focuses on comparing the degree of fragmentation depending on the isolated ion pair vapor source of a hypergolic ionic liquid, 1-Butyl-3-Methyl-Imidazolium Dicyanamide ([$Bmim^+$][Dca^-]), shown in Figure 6.1(b), and on finely controlling the internal energy imparted by thermal vaporization and photoionization. For a better understanding of the internal energy extent originating from different ion pair vapor sources, effusive and aerosol, the appearance energy shifts of 1-Ethyl-3-Methyl-Imidazolium Bis(trifluoromethylsulfonyl)imide ([$Emim^+$][Tf_2N^-]) ionic liquid vapor are measured by photoionization efficiency (PIE) curves at the same vaporization temperatures, clearly showing the effect that the vapor source has on the ion pairs.

6.1.2 Experimental Methods

Isolated ion pairs of ionic liquids are generated in the gas phase by thermal vaporization of IL aerosol particles and are monitored using soft ionization detection with tunable vacuum ultraviolet (VUV) photoionization mass spectrometry. Those ion pairs that are generated by aerosol particles are compared to those generated by a conventional effusive beam.[27-28, 53] The aerosol experimental apparatus at the Chemical Dynamics Beamline 9.0.2.1 of the Advanced Light Source in Berkeley, California, previously described in detail,[35] includes a particle generation system, a particle size analyzer, and an aerosol mass spectrometer (AMS).

Ionic liquid aerosols are generated by a constant output atomizer (TSI model no. 3076) from 0.5 g/L in water solutions of ionic liquid, [$Emim^+$][Tf_2N^-] (Sigma, ≥97% purity) or [$Bmim^+$][Dca^-]) (Aldrich, ≥97% purity), structures shown in Figure 6.1. Generated liquid droplets are then entrained in a nitrogen carrier gas at 10 psi and are dried by passing through a room-temperature diffusion dryer with a small chance of water still remaining in the particles. The aerosol particle size distribution and number density are measured with a commercial differential mobility analyzer (DMA; TSI model 3081) coupled to a condensation particle counter (CPC; TSI model 3772). Aerosol particles of [$Emim^+$][Tf_2N^-] produced in this way have a median diameter of 187 ± 3 nm, as shown in Figure 6.2(a), and a total concentration of 1.4×10^5 particles/cm^3, where similarly produced aerosol particles of [$Bmim^+$][Dca^-] have a median diameter of 184 ± 3 nm (Figure 6.2(b)) and a total concentration of 2.0×10^5 particles/cm^3. To generate isolated ion pairs in the gas phase, the dry aerosol particles, focused through the aerodynamic lens with a particle flux of about 3×10^7 particles/s entering the interaction region,[43] are thermally vaporized by a heated copper block typically held at a temperature between 423 K and 493 K. In all cases, ionic liquids, [$Emim^+$][Tf_2N^-] and [$Bmim^+$][Dca^-], were kept well under their thermal decomposition temperatures (T_d), which are 675 K[1] and 573 K,[160] respectively. The vapor from aerosol particles

provides isolated ion pairs and the mass spectra are followed by VUV photoionization to produce positive ions by single photon ionization. The time-of-flight (TOF) mass spectra and ion yields are measured with a pulsed TOF mass spectrometer and recorded as a function of the heater temperature and the photon energy of the tunable VUV source, between 7.5 and 11 eV in 75 meV steps, for each ionic liquid.

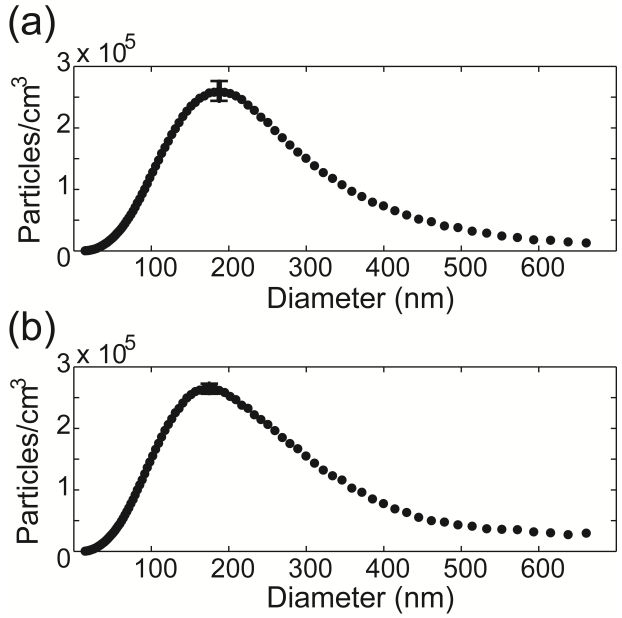

Figure 6.2. Aerosol particle size distribution of ionic liquid, (a) [$Emim^+$][Tf_2N^-] and (b) [$Bmim^+$][Dca^-] with median diameter of 184 ± 3 nm and 187 ± 3 nm respectively, obtained by atomizing 0.5 g/L aqueous solutions.

In the other sets of experiments, isolated ion pairs are prepared as an effusive beam, which is a typical pyrolysis source using an aluminum oven body with a glass interior heated by resistive heater cartridges. The glass interior prevents IL sample vapor from colliding with the aluminum wall, and there is no evidence for decomposition. IL sample is heated to 350 K overnight prior to experiments in order to remove contaminants. IL vapor is emitted through an opening in the oven as an effusive beam by heating the 0.5 ml size reservoir of a glass vial located in the aluminum oven.[27-28, 53] The effusive beam is skimmed by an ~1 mm skimmer before the beam is ionized by the VUV light. Similar to the experiments for ion pairs from the aerosol particles, TOF mass spectra and ion yields of the positive ions produced by photoionization of the effusive beam are recorded as a function of photon energy, tunable between 7.5 eV and 11 eV in 50 meV steps. All of the measurements, mass spectra, PIE scans, and heater block temperature scans, for two different sources (aerosol, and effusive source), were measured at least five, two, and three times, respectively. Temperature scans of the aerosol source were not only repeated but also measured while both heating and cooling the heater block in order to ensure that there is not thermal decomposition occurring during heating. Collected PIE curves were rebinned into 0.2 eV step data sets for comparison of the two sources, effusive beam and aerosol source beam.

6.1.3 Results and Discussion

Isolated ion pairs of ionic liquids are prepared in the gas phase by thermally vaporizing from submicron aerosol particles with median diameter around 180 nm; the particle size distribution is shown in Figure 6.2. These ion pairs in the effusive and aerosol source beam are monitored by near threshold photoionization with mass resolutions of 480 and 1061 at 96 amu/q, respectively. Both ionic liquids studied here, $[Emim^+][Tf_2N^-]$ and $[Bmim^+][Dca^-]$, show the intact cation signal, which is an indication of isolated ion pairs. The intact cation signals, $Emim^+$ (111 amu/q), from $[Emim^+][Tf_2N^-]$ in the effusive beam (top) and aerosol source beam (bottom) are shown in Figure 6.3(a) and are highlighted in grey color. The intact cation signal dominates in both mass spectra, whereas the aerosol source beam shows small hydrogen loss from the intact cation as well. The hydrogen loss from the intact cation that is ca. 0.5% signal of intact cation can originate by proton transfer from the ionic liquid to the solvent since the submicron aerosol particles have a trace of water remaining in the particles. This hydrogen loss from the ionic liquid during aerosol generation is being studied further. However it is noteworthy that isolated ion pairs from the aerosol source of $[Emim^+][Tf_2N^-]$ are successfully prepared. Whether those pairs have some associated water molecules may be revealed by particle size measurements discussed in the following section 6.2. In the case of DNA bases, the addition of water molecules in cluster studies reveals both masses containing water and shifts in the ionization energies.[40]

To further explore the isolated ion pair and its internal energy depending on the type of vapor source, photoionization efficiency (PIE) curves of the intact cation $Emim^+$ for the ionic liquid $[Emim^+][Tf_2N^-]$ were measured, as shown in Figure 6.3. The two different sources are the aerosol and effusive source. Unfortunately, the changes in the appearance energy of the intact cation from the hypergolic ionic liquid, $[Bmim^+][Dca^-]$, could not be directly measured because of the limited signal of the intact cation for the effusive beam, as shown in the mass spectra of Figure 6.4. The shift in appearance energy in the near-threshold ionization region for $[Emim^+][Tf_2N^-]$ was therefore explored at 493 K for the two sources, as a measure of the internal energy. The photoionization efficiency curve of the intact cation, $Emim^+$, produced from the aerosol source beam, is shown in Figure 6.3(b). Raw PIE curves (○) of $Emim^+$ produced from vaporization of aerosol particles show an additional low energy component due to a minor contribution from slowly vaporizing residual ionic liquid on the heater block. This contribution from the residual vapor (●) to the PIE curve is measured by turning off the aerosol source, keeping the heater at the same temperature, and scanning the photon energy either increasing or decreasing, in order to make sure there is no artifact coming from sample flux changes while scanning. The pure PIE curve of the immediately vaporized ion pair, shown in Figure 6.3(b) top (▲), is found by subtracting the normalized residual signal from the total raw PIE curve.

This subtracted signal (▲) that is the PIE curve of the intact cation from dissociative ionization of ion pairs vaporized directly from the aerosol source beam is plotted together with the other PIE curve measured for the effusive beam (○) for comparison in Figure 6.3(c). Data from the two sources is rebinned into photon energy steps of 0.2 eV to compare consistent resolution of data sets.

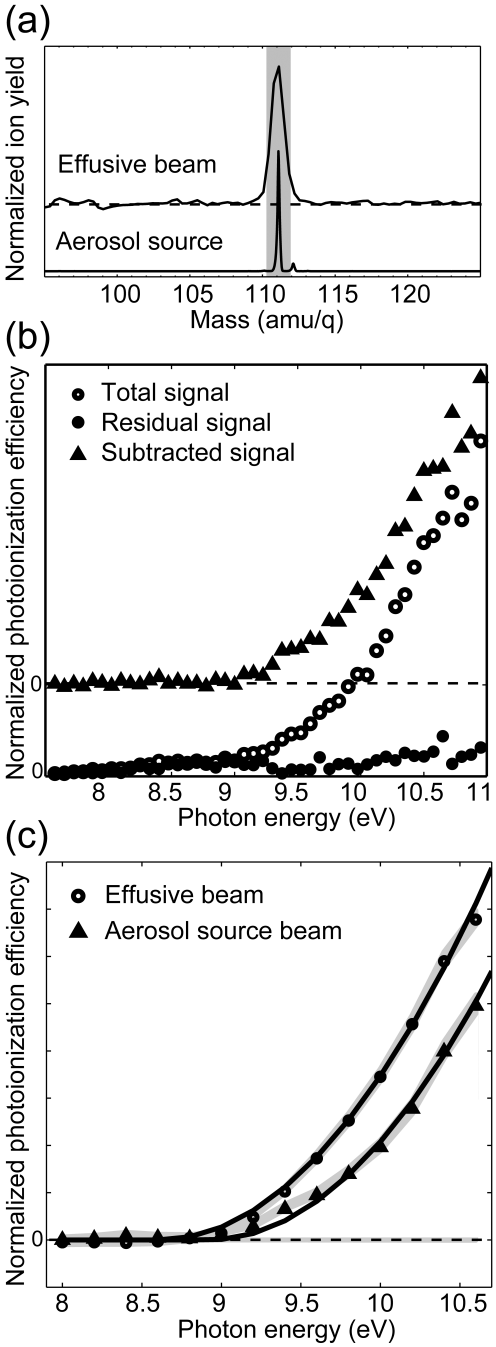

Figure 6.3. Mass spectra of (a) $[Emim^+][Tf_2N^-]$ from effusive beam (top) and aerosol source beam (bottom) at a photon energy of 9.5 eV with intact cation ($Emim^+$, 111 amu/q) highlighted in grey. Each mass spectrum of the effusive beam (top) and the aerosol source beam (bottom) is collected with mass resolution of 480 and 1061 at 96 amu/q, respectively. (b) Photoionization efficiency (PIE) curves of the intact cation ($Emim^+$) from $[Emim^+][Tf_2N^-]$ aerosol particles of total signal (○), which is the raw data collected upon aerosol vaporization, residual signal (●) that is measured without immediately vaporizing the aerosol particles, and the subtracted signal that is the pure contribution of immediately vaporized aerosol particles (total−residue, ▲) at 473 K. (c) Comparison of the photoionization efficiency curves of the intact cation ($Emim^+$) from two different sources, Effusive beam (○), and Aerosol source beam (▲) with the area of error in grey.

Near threshold the PIE curves are fitted similar to previous studies,[28] but they are not convoluted with a Gaussian which was previously used based on the assumption that the source temperature was all the same. The PIE curves are fitted with the functional form $0.5 \cdot \alpha(E-E_0)^2$ with two fit parameters, normalization factor α and the ionization threshold E_0, in order to find the changes in the ionization threshold that are due to the source temperature change. The normalization factor α, which is a fit parameter, takes into account the molecular density difference of two sources and the PIE curves are fitted over a wide range of photon energy up to 10.8 eV. The solid lines in Figure 6.3(c) are the fitted threshold functions, corresponding to threshold ionization energies of 8.61 ± 0.12 eV and 8.93 ± 0.13 eV for the effusive beam and aerosol source beam, respectively. For all experiments, the vaporization temperature was kept at 493 ± 2 K, and thus the observed shifts are not expected to be due to different temperatures of the sources. As expected from previous studies,[43, 161] the appearance energy increases from the effusive beam to the aerosol source beam. The aerosol source beam shows a +0.3 eV shift toward higher appearance energy compared to the effusive beam. This increased appearance energy of the aerosol source suggests that the aerosol source beam produces ion pair vapor with less internal energy than the effusive beam does. Evaporation of the IL aerosol particles may produce some of the cooling by molecules vaporizing from an impact at the heater block that leads to less internal energy.

The hypergolic ionic liquid is also studied using the aerosol source to produce isolated ion pairs that are internally cooler than those generated by the effusive source. Mass spectra obtained for the hypergolic ionic liquid, $[Bmim^+][Dca^-]$, vaporized at 473 K from both the aerosol and effusive sources are shown in Figure 6.4. The overall mass spectra of the hypergolic IL vapors prepared from the effusive and aerosol sources show dramatic differences regardless of the photon energy, (a) 8.5 eV or (b) 9.4 eV, used for ionization. Prominent peaks in the mass spectra of the aerosol source beam are 139 amu, the intact cation, and 137 amu, a fragment of the intact cation in which two hydrogens are lost or a fragment resulting from multiple proton transfers to the solvent as in the $[Emim^+][Tf_2N^-]$ case. On the other hand, mass spectra of the effusive beam do not show any of those intact cation signals, but instead there are evident peaks at 178 and 124 amu. A molecular structure shown in Figure 6.4 above the 178 amu peak is the strongest candidate for this possible ion species, which is a structurally reorganized fragment of the ion pair from which two hydrogens on the cation have been displaced by the anion fragment, -NCN. The 124 amu peak is assigned either to the cation fragment with the loss of a methyl group or to a decomposition product of 1-Butyl-Imidazolium. Details of the fragments, whether they are from thermal decomposition or dissociative ionization of the effusive beam of the hypergolic ionic liquid, $[Bmim^+][Dca^-]$, are under further investigation. Despite the fact that the photodissociation mechanism and vaporization of the $[Bmim^+][Dca^-]$ ion pair from the effusive beam is not yet established, it is important to note that the photoionization masses change drastically with the source and there is much more extensive fragmentation and formation of new products in the effusive source.

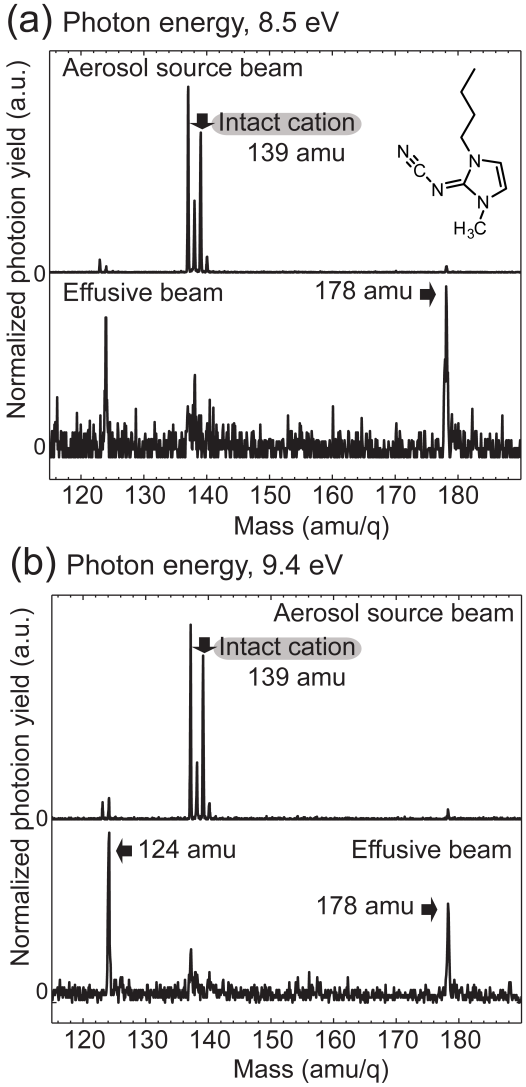

Figure 6.4. Photoionization mass spectra of hypergolic ionic liquid, [$Bmim^+$][Dca^-], at photon energy of (a) 8.5 and (b) 9.4 eV obtained from effusive beam and aerosol source beam both vaporized at 473 K. Intact cation, $Bmim^+$ (139 amu), that represents the ion pair is detected at both photon energies, whereas fragments of 178 amu (([$Bmim^+$]–H)+NCN) and 124 amu (([$Bmim^+$]–CH_3) or [Bim]$^+$) dominate in the mass spectrum of the effusive beam with little indication of the ion pair at 139 amu. Mass spectra of the aerosol source beam has better signal-to-noise of ca. 800 with 2,000,000 pulses of integration than the effusive beam which has signal-to-noise of ca. 7 with 500,000 pulses of integration.

In addition to the intact cation ($Bmim^+$, 139 amu) signal, it is also possible to observe the corresponding ^{13}C isotope peak at 140 amu in the mass spectra of the aerosol source beam. The relative yields of the ^{13}C isotope peak, 8.4 ± 0.4% measured at a photon energy of 8.5 eV, and 8.9 ± 0.3% measured at photon energy of 9.4 eV, are in good agreement with the natural isotope abundance, 8.8%, for $Bmim^+$ (139 amu) with eight carbon atoms. The ^{13}C isotope peak of the 137 amu ([$Bmim^+$]–2H) at 138 amu cannot be measured due to the overlapping signal of another 138 amu fragment ([$Bmim^+$]–H). However, if we assume the natural isotope abundance of 8.8%

for the unknown [$Bmim^+$]–2H fragment (137 amu) and [$Bmim^+$]–H fragment (138 amu) signal, we can estimate the ratio of fragments to intact cation, [$Bmim^+$]–2H / [$Bmim^+$]–H / [$Bmim^+$], to be 1.3/0.4/1.0 at 8.5 eV and 1.2/0.2/1.0 at 9.4 eV.

The intact cation, $Bmim^+$ (139 amu), that is observed in the mass spectra of the aerosol source beam is most likely produced by dissociative photoionization (equation (1.1)). This is typical evidence[28-29, 53] for the production of an isolated ion pair in the gas phase upon vaporization of [$Bmim^+$][Dca^-] ionic liquid aerosol particles. There is no indication of ionic liquid clusters with water or extensive thermal decomposition (data not shown) from the aerosol source beam as long as the impact heater temperature is kept lower than would be needed to produce cluster formation or thermal decomposition (T_d, 573 K[160]). Furthermore no parent ionic liquid mass is observed, similar to previous studies.[28-29, 53] The dominant peak other than the intact cation, the loss of two hydrogens from the cation fragment (137 amu), and other small features of 178 and 124 amu mass peaks, which are mainly observed in the effusive beam, suggest that there is enough energy in the aerosol heater zone for the ion pair to dissociatively ionize to other ion species or to decompose into these fragments. The results show that the ion pairs generated from the aerosol source acquire some internal energy that eventually leads to a small amount of dissociative photoionization or decomposition resulting in fragments other than the intact cation upon vaporization or ionization.

The general difference in the mass spectra of the aerosol source beam and the effusive beam is that the major photofragments from the effusive beam are the minor ones in the mass spectra of the aerosol source beam. Since those minor photofragments of the aerosol source beam, 178, 138, and 124 amu, are due to the excess energy imparted to the isolated ion pair, it shows that the aerosol beam has isolated ion pairs with considerably less internal energy resulting in much less extensive dissociative ionization and reaction. Ion pairs vaporized from the effusive source have a high probability to gain more energy and possibly react via intermolecular collisions and multiple high temperature wall collisions, resulting in a considerable internal energy, whereas aerosol particles vaporized by an impact at the heater block are both energized and further cooled by evaporation, resulting in an ion pair vapor that has less decomposition or reaction and a lower temperature. This means that the isolated ion pair vapor prepared from aerosol particles has less internal energy imparted upon thermal vaporization compared to those from the effusive beam, which is in good agreement with previous studies,[43] where reduced thermal internal energy content is reported for biomolecules in gas phase produced by aerosol particle vaporization. Therefore, to explore the unique reaction dynamics of hypergolic ionic liquids, aerosol particle vaporization is a suitable way to introduce intact ion pairs into the gas phase to decrease the internal energy, essentially by having only one impact on the heater block to energize and evaporate the molecules into the gas phase.

Another difference in the mass spectra of the aerosol source beam and the effusive beam is that the signal-to-noise of the aerosol source beam measurement (S/N, ca. 800) is better than the effusive beam measurement (S/N, ca. 7). Data for the aerosol source beam is collected for 2,000,000 pulses while the data for the effusive beam is collected for 500,000 pulses, which is 4 times less integration time than the aerosol source beam. If we assume that the signal-to-noise will increase by the square root of the integration time, the mass spectra of the effusive beam will have a signal-to-noise of ca. 14 better at the same integration time as the aerosol source beam

measurement. Thus the signal-to-noise in the mass spectra of the aerosol source beam is an order of magnitude greater with the effusive beam after taking into account the integration time difference. Better signal-to-noise in the mass spectra of the aerosol source beam is probably due to the closer distance of the vaporization source from the ionization region. This shows that the aerosol particle vaporization has the advantage in not only producing molecules with less internal energy, but also in having superior signal-to-noise in TOF measurements.

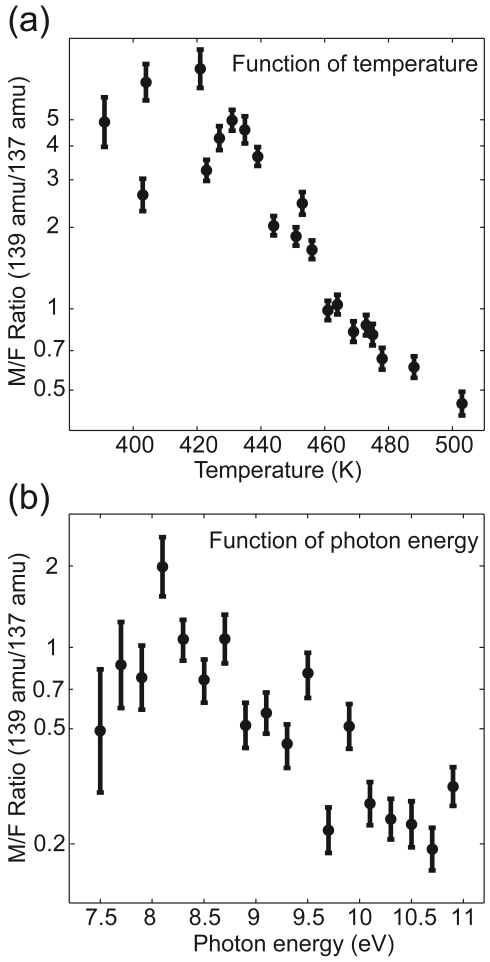

Figure 6.5. Molecule (M) to Fragment (F) ratio for ion pairs of [Bmim$^+$][Dca$^-$] from aerosol source beam (M/F Ratio, 139 amu/137 amu) (a) as a function of temperature at photon energy of 8.5 eV and (b) as a function of photon energy at vaporization temperature of 473 K.

The influence of the internal energy on photofragmentation of [Bmim$^+$][Dca$^-$] ion pairs prepared by the aerosol method is investigated in more detail by monitoring the molecule to fragment ratio as a function of both (a) temperature and (b) photon energy, as shown in Figure 6.5. The molecule (M) to fragment (F) ratio is determined by the intensity ratio of the intact cation (139 amu), which represents the molecular ion, and the cation fragment with the loss of two hydrogens (137 amu). The M/F ratios decrease with temperature and photon energy as the amount of internal energy imparted into the isolated ion pair increases, thus leading to more

dissociative photoionization. At a fixed photon energy, 8.5 eV, the M/F ratio exponentially decreases with temperature over the 50 K range studied and is consistent with the previous effect[43] observed for biomolecules. The exponential decay behavior was suggested[43] to be due to an "Arrenhius-like" phenomenological activation energy, which leads to efficient dissociative photoionization when excess energy is imparted by photoionization into the thermally activated ion pair. The M/F ratio is also observed to decrease as a function of photon energy at a fixed temperature of 473 K. As the photon energy is increased to ionize the neutral ion pair, the amount of internal energy deposited increases and results in greater fragmentation. The intact cation signal used to monitor the isolated ion pairs decreases relative to the fragment signal regardless of the fragment chosen (124, 137, 138, 178 amu, data not shown) as a function of temperature and photon energy. As expected, the highest M/F ratio is observed at the lowest vaporization temperature around 423 K and at the lowest photon energy used for ionization near threshold (8.0 eV). The results show that the internal energy of ion pairs can be reduced by using near threshold ionization and lower vaporization temperature for nearly "fragmentation-free" mass spectra. This decreased fragmentation of isolated ion pairs from the aerosol source beam clearly affords a number of advantages over conventional effusive beams for monitoring reaction dynamics of hypergolic ionic liquids in the future.

6.1.3 Conclusion

Using aerosol particle vaporization as a source, isolated ion pairs of a hypergolic ionic liquid and a relatively stable ionic liquid are generated in the gas phase and these ion pairs are compared to the ones produced via a conventional effusive beam, all of which are monitored with a tunable synchrotron light source in the near threshold ionization region. Vaporizing ionic liquid aerosol particles reduces the amount of internal energy imparted into the isolated ion pair upon thermal vaporization and minimizes reactive processes. This capability not only affords greater insight into the various methods of generating ion pair vapors, but also provides a better way to monitor reaction dynamics of hypergolic ionic liquids in the future, with simpler photofragmentation patterns of the ion pair itself and fewer complications in tracing molecular changes. Given the distinctively strong intensity of the intact cation and superior signal-to-noise with this aerosol experimental setup, which has also been shown to be capable of studying reaction dynamics,[162] future studies are planned to utilize and apply this technique to further understand hypergolic IL reactivity.

- Acknowledgments

The authors gratefully acknowledge funding from the U.S. Air Force Office of Scientific Research for supporting CK, DS and SL (Grant No. FA9550-10-1-0163), and for SC and GV (Grant No. FA9300-06-C-0023). This work at the ALS was supported by the Director, Office of Energy Research, Office of Basic Energy Sciences, Chemical Sciences Division of the U.S. Department of Energy under Contract No. DE-AC02-05CH11231 (CL, CH, AG, OK, KW, MA, and SL). The authors thank Dr. Musahid Ahmed and Dr. Kevin Wilson of the Chemical Dynamics Beamline for help in the measurements.

6.2 Identification of reaction intermediates: Hypergolic reaction of an ionic liquid with nitric acid

Aerosol particles of a hypergolic ionic liquid (IL), 1-butyl-3-methyl-imidazolium dicyanamide ([$Bmim^+$][Dca^-]), are used to study the reaction dynamics of the [$Bmim^+$][Dca^-] with nitric acid. Isolated ion pairs and reaction products generated upon vaporization of the reacted aerosol particles are investigated by single photon ionization with tunable vacuum ultraviolet (VUV) to identify the reaction intermediates/products. Ionization potentials (IP) of the reaction products with masses of 42 amu/q and 85 amu/q, are measured to be 10.3 ± 0.1 eV and 10.2 ± 0.2 eV, respectively, in good agreement with the literature/theoretical values of cyanamide (10.4 ± 0.1 eV) and isocyanourea (10.0 ± 0.1 eV). More volatile products, CO_2 and N_2O, are observed as well in the hypergolic reaction. Evidence for the initial stage intermediate, the nitro-substituted intermediate ($C_2N_4O_3H_2$) is shown by the direct observation of cyanamide, CO_2, and N_2O for the first time.

6.2.1 Introduction

Environmental concern for the most widely used hypergolic propellant, monomethyl hydrazine (MMH), which is highly toxic and carcinogenic, encourages the development of 'green' energetic compounds such as ionic liquids. Energetic ionic liquids (EILs) are ambient temperature molten salts[1] with potential applications as propellants, explosives, and pyrotechnics. EILs have recently received much attention as an attractive alternative to traditional energetic compounds due to their unique properties (e.g., negligible vapor pressure, high thermal stability, environmental friendliness). Since ionic liquids have little or no vapor toxicity and are thermally stable, they are environmental-friendly and safe to transport. EILs are emerging as promising next generation hypergolic propellants that are green and safe.

Recently, several energetic ionic liquids, the dicyanamide,[23] nitrocyanamide,[51] azide,[24] and aluminum borohydride systems,[19] have been shown to be hypergolic upon contact with common rocket oxidizers, such as nitric acid or hydrogen peroxide. Since 2008, the dicyanamide system has been studied as a stable energetic ionic liquid and shown to behave as a hypergolic fuel. The hypergolic reaction of an ionic liquid based on the dicyanamide anion with white fuming nitric acid has been demonstrated and the mechanism has been proposed.[23] Products of the reaction, N_2O, CO_2, and HNCO, have been observed by fourier transform infrared (FTIR), a positive biuret test in the solution, and initial ab initio calculations. A reaction intermediate, dinitrobiuret, has been also found by investigating sodium dicyanamide, which was used to investigate the role of the anion in the reaction.[163] In addition, reaction products in the condensed phase including melamine have been discovered.[164] However, an initial stage reaction intermediate or product that causes ignition as well as a clear mechanism has yet not been fully understood.

Understanding the reaction mechanism of the ignition reactions for hypergolic ionic liquids is a key in developing and optimizing a next generation bipropellant. Insight into the ignition

mechanism can be obtained by direct observation of the early stage reaction products and intermediates. Previously, other heterogeneous chemistries have been successfully studied using flow tube methods coupled with an aerosol mass spectrometer, which can directly detect chemical changes upon reaction. In this study, the aerosol flow tube method has been applied to investigate the hypergolic reaction of an ionic liquid. Initiating oxidation in a flow tube and observing the reaction downstream has advantage of providing a variety of experimental conditions and the coupled aerosol mass spectrometer (AMS) allows quantitative measurement of the products that are at different reaction stages depending on the conditions.

Ionic liquid aerosol particle generation and its thermal vaporization have previously been demonstrated and characterized in previous section 6.1 and chapter 5.[32, 53, 74, 81] It has been shown that isolated ion pairs can be prepared in the gas phase by thermal vaporization of submicron IL aerosol particles. Soft ionization of those isolated ion pairs leads to dissociative ionization that produces the intact cation as a result. These nearly fragmentation free mass spectra provide advantages in monitoring the intact cation as an indication of an isolated ion pair in the gas phase and in following the chemical changes upon reaction in the flow tube with background free measurements. In addition, reaction products can be identified using a tunable ionizing light source and obtaining the photoionization efficiency (PIE) curves since ionization thresholds are mostly distinguishable for molecules. We apply this new approach to study the dynamics and kinetics of the reaction of hypergolic ionic liquid, 1-Butyl-3-Methyl-Imidazolium Dicyanamide ($[Bmim^+][Dca^-]$), with nitric acid using the flow tube method with tunable vacuum ultraviolet (VUV) soft ionization mass spectrometry. This section focuses on investigating the reaction intermediates and products in the condensed particle phase as well as in the gas phase and on obtaining better insight into the reaction mechanism.

6.2.2 Experimental Methods

Hypergolic reaction dynamics is studied using the "aerosol flow tube method" in conjunction with soft ionization detection with tunable vacuum ultraviolet (VUV) photoionization mass spectrometry. The reaction intermediates/products produced upon hypergolic reaction of ionic liquid and nitric acid are identified by obtaining their photoionization efficiency (PIE) curves. The aerosol experimental apparatus[35] at the Chemical Dynamics Beamline 9.0.2.1 of the Advanced Light Source in Berkeley, California, previously described in detail in Chapter 2, includes a particle generation system, a particle size analyzer, reactor flow tube, and an aerosol mass spectrometer (AMS).

Ionic liquid aerosols are generated by a constant output atomizer (TSI model no. 3076) from 0.5 g/L in water solutions of ionic liquids, $[Emim^+][Tf_2N^-]$ (Sigma, ≥97% purity) for particle characterization and $[Bmim^+][Dca^-]$) (Aldrich, ≥97% purity) for reaction dynamics studies, structures shown in Figure 6.1. Generated liquid droplets are then entrained in a nitrogen carrier gas at 10 psi and are dried by passing through a room-temperature diffusion dryer, with a small chance of water still remaining in the particles. To quantify the amount of water left in the aerosol particle of $[Emim^+][Tf_2N^-]$, a narrow range of size distribution of particles was selected by a differential mobility analyzer (DMA; TSI model 3081) and then introduced into a thermodenuder to heat up the particles and remove further water from the particles. The particle

size distribution is measured with an additional differential mobility analyzer (DMA; TSI model 3081) coupled to a condensation particle counter (CPC; TSI model 3772) after the thermodenuder.

For the reaction dynamics studies, ionic liquid aerosol particles at room temperature were used without going through the thermodenuder and the full size distribution of the particles generated by the atomizer was used. The aerosol particle size distribution and number density are measured with a commercial differential mobility analyzer (DMA; TSI model 3081) coupled to a condensation particle counter (CPC; TSI model 3772). Aerosol particles of $[Bmim^+][Dca^-]$ have a median diameter of 184 ± 3 nm (Figure 6.2(b)) and a total concentration of 2.0×10^5 particles/cm^3.

Dry aerosol particles are entrained in nitrogen carrier gas to the home-built glass reactor flow tube, which has a volume of 250 ± 5 cc. Nitric acid vapor is introduced by bubbling nitrogen carrier gas at a flow rate of 610 sccm through a fuming nitric acid sample (Sigma-Aldrich, ≥ 99.5%) at room temperature. The nitric acid vapor is diluted with 400 sccm of nitrogen, and then the diluted nitric acid vapor enters the reactor flow tube at a controlled flow rate of 0.4 scfh (189 sccm). The flow rate at the reactor flow tube is 1.6 ± 0.1 slm and the total reaction time is about 9.4 ± 0.1 sec. At this flow rate, there are 3.2×10^{12} molecules/cm^3 of ionic liquid and 4.4×10^{16} molecules/cm^3 of nitric acid. All experiments are performed at room temperature.

A nitric acid denuder[165] is placed after the flow tube to trap all the excess nitric acid and end the hypergolic reaction before it enters the interaction chamber. The nitric acid denuder is a diffusion dryer that is a foot long tube filled with sodium carbonate (Na_2CO_3) while a hollow mesh tube in the center allows aerosol particles to pass through. Powdered sodium carbonate is held together around the hollow mesh tube by fine glass wools.

To monitor the isolated ion pairs and reaction intermediates/products, the reacted aerosol particles are focused through the aerodynamic lens with a particle flux of about 3×10^7 particles/s entering the interaction region.[43] The particles are thermally vaporized by a heated copper block typically held at 423 K for condensed phase product measurements and at 323 K for volatile product measurements. In all cases, ionic liquid, $[Bmim^+][Dca^-]$, was kept well under the thermal decomposition temperature (T_d), which is 573 K.[160] The vapor from aerosol particles provides isolated ion pairs and reaction intermediates/products and the mass spectra are followed by VUV photoionization to produce positive ions by single photon ionization. The time-of-flight (TOF) mass spectra and ion yields are measured with a pulsed TOF mass spectrometer and recorded as a function of the photon energy of the tunable VUV source, between 9 eV and 15 eV in 50 meV steps, for each measurement.

Ab initio calculations were performed using Gaussian 03W[100] at the B3LYP 6-31+G(d,p) level of theory to preoptimize geometries. Final optimization and energy calculations were performed at the MP2 6-31+G(d,p) level of theory using GAMESS.[101-102] Resulting MP2 energies at 0 K were corrected for unscaled zero-point vibrational energies. The MP2 6-31+G(d,p) level of theory was assigned an uncertainty of ±0.1 eV based on our previous calculations.

6.2.3 Results and Discussion

Hypergolic reaction of ionic liquid, [Bmim$^+$][Dca$^-$], with nitric acid is monitored with soft ionization mass spectrometry. Mass spectra of the aerosol particles that are reacted and not reacted with nitric acid at a fixed photon energy of 11 eV are shown in Figure 6.6. The reacted mass spectrum in Figure 6.6(a) shows not only the reaction intermediates/products but also the fragments resulting from dissociative ionization of the ionic liquid itself. To clearly spot the change upon reaction, the mass spectrum of ionic liquid from unreacted aerosol particles is shown (Figure 6.6(b)) as in previous studies (section 6.1). Isolated ion pairs, [Bmim$^+$][Dca$^-$], are produced from thermal vaporization and the intact cation, Bmim$^+$ (139 amu/q), is observed as a result of dissociative ionization. The baseline of ionic liquid mass spectrum (b) is subtracted from the mass spectrum of reacted particles (a) to obtain a transient mass spectrum exhibiting new products upon reaction as a positive signal and depleted reactant as a negative signal. Depletion of the intact cation, Bmim$^+$ (139 amu/q), is observed in (c), indicating the decrease of ionic liquid molecules during the hypergolic reaction, as the intact cation signal represents the intact ion pairs.

Appearance of additional masses such as 17, 42, 44, 58, 72, and 85 amu/q are observed upon the hypergolic reaction as shown in Figure 6.6(c). The additional masses are either true reaction intermediates/products or fragments resulting from introducing nitric acid to the system. Nitric acid vapor is monitored without mixing IL aerosol particles together to eliminate the products resulting from nitric acid only. Masses of 17, 58, and 72 amu/q are found to arise from nitric acid only (not shown here). While the masses of 58 and 72 amu/q are not identified, 17 amu/q seems to be ammonia (NH_3), perhaps an impurity from the system. The small signal of 17, 58, and 72 amu/q in the IL aerosol mass spectrum (b) may be a signal from the remaining nitric acid on the copper heater block.

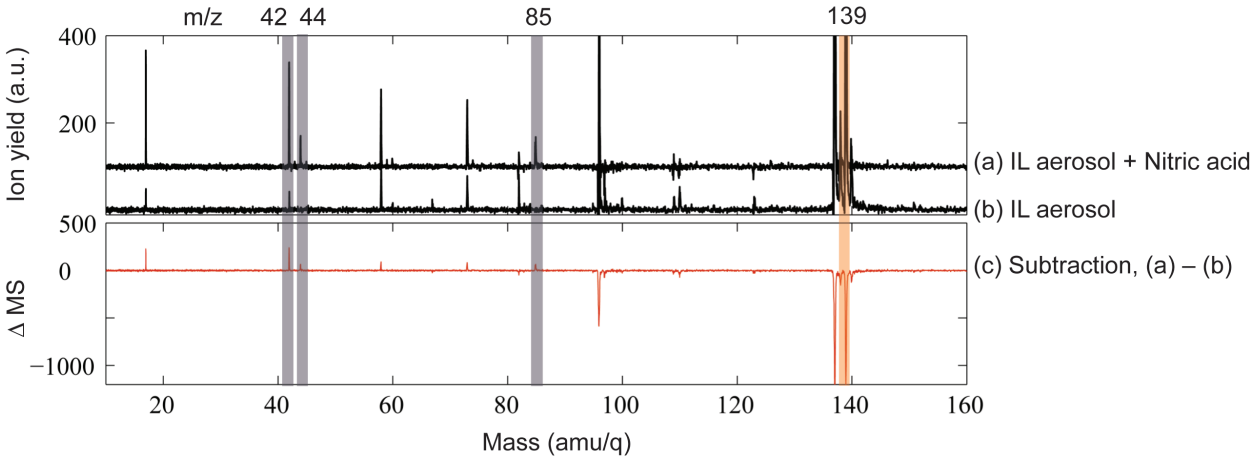

Figure 6.6. Mass spectra of (a) reacted IL aerosol particle with nitric acid, exhibiting intact cation and reaction intermediates/products, and (b) IL aerosol particle only, which is a baseline for the dissociative ionization of [Bmim$^+$][Dca$^-$]. (c) Mass spectrum reacted IL aerosol minus unreacted IL aerosol, '(a) – (b)'. It shows depletion of the intact cation (139 amu/q) in orange and appearance of the reaction products of 42 amu/q, 44 amu/q, and 85 amu/q in grey color.

Other masses of 42, 44, and 85 amu/q are most likely reaction intermediates/products as the possibility of these fragments arising from the ionic liquid or nitric acid has been eliminated. These masses that we suggest to be reaction intermediates/products are highlighted in grey in Figure 6.6(c). It is neither easy nor reliable to guess what these products are only by their masses. Their photoionization efficiency curves (PIE) were obtained using the tunable vacuum ultraviolet light from the synchrotron. The PIE curves of the reaction products are measured at least five times to confirm the experimental ionization thresholds of each mass.

The ion yields of these three reaction products that are found from integrating peaks of each mass are shown as a function of photon energy in Figure 6.7. Each PIE curve (○) is collected in the photon energy range of 9 eV to 11 eV in 50 meV steps and the fitted functions are shown with solid red lines (−). Near threshold, the PIE curves are fitted as in previous studies[28, 32] with the functional form $0.5\alpha(E-E_0)^2$ with two fit parameters, normalization factor α and the ionization threshold E_0 in order to find the ionization thresholds of the reaction products. Those ionization threshold values that are obtained from the fitting procedure are shown in each of the PIE curves. Ionization threshold for the reaction product (a) with mass 42 amu/q is measured to be 10.3 ± 0.1 eV, which is in good agreement with the ionization potential value (10.4 eV) of cyanamide (NH_2CN) that is found in the NIST webbook. The ionization potentials of other molecules with mass 42 amu/q such as diazomethane (CH_2N_2, IP=8.999 ± 0.001 eV) or ketene (C_2H_2O, IP=9.617 ± 0.003 eV) do not match well with the experimental IP value. The molecular structure of cyanamide, which seems to be the reaction product of mass 42 amu/q produced by the hypergolic reaction, is shown in Figure 6.8(a).

Reaction product (b) with mass 44 amu, with a measured ionization threshold of 10.5 ± 0.2 eV, is not clearly identified yet. The mass 44 amu corresponds to N_2O and CO_2, but these have ionization thresholds of 12.9 eV, and 13.7 eV, respectively, which do not match the experimentally measured ionization potential. Acetaldehyde (C_2H_4O) with an IP of 10.229 ± 0.0007 eV is close to the experimentally obtained IP, but ethylene oxide (C_2H_4O) with an IP of 10.56 ± 0.01 eV has an IP that better matches the experimental value of 10.5 ± 0.2 eV than acetaldehyde. However, it is not clear how these molecules, acetaldehyde or ethylene oxide, can be formed during the hypergolic reaction in the suggested reaction mechanism that will be discussed later. It is possible that ethylene oxide is formed during a side reaction rather than the main reaction or that a fragment of 44 amu/q is produced upon dissociative ionization of a larger molecule. It will require more insight on the reaction mechanism and additional investigation of the reaction by changing the conditions (reaction concentration, reaction time, and ionization photon energy) to confirm the reaction product with IP of 10.5 eV and mass 44 amu/q.

The ionization threshold measured for the reaction product with mass 85 amu/q is 10.2 ± 0.2 eV (Figure 6.7(c)). This experimental IP value is in good agreement with the calculated IP value of 10.0 ± 0.1 eV for isocyanourea ($C_2N_3H_3O$). The molecular structure of isocyanourea is shown in Figure 6.8(b). Other molecules, such as N-allyl-N,N-dimethylamine ($C_5H_{11}N$, IP=7.84 ± 0.03 eV), propionaldehyde ethylamine ($C_5H_{11}N$, IP=8.7 eV), acetone cyanohydrin (C_4H_7NO, IP=11.09 eV), and others, were considered as well before confirming that isocyanourea is a likely reaction product produced by the hypergolic reaction.

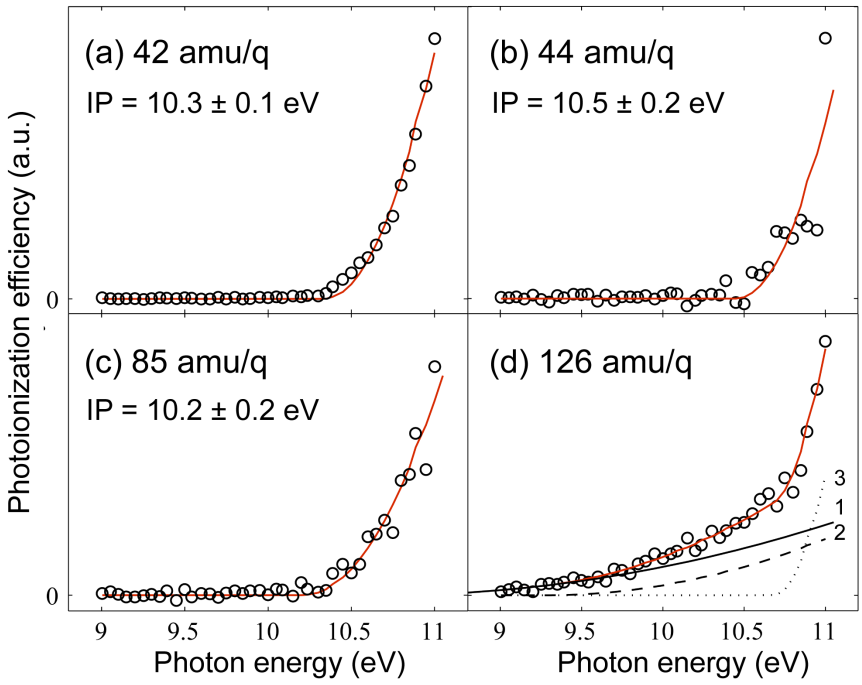

Figure 6.7. PIE curves of mass (a) 42 amu/q, (b) 44 amu/q, (c) 85 amu/q, and (d) 126 amu/q. Each PIE curve (○) is collected in the photon energy range of 9 eV to 11 eV in 50 meV steps and its fitted function is shown by a solid red line (–). Ionization threshold measured for 42 amu/q is 10.3 ± 0.1 eV, for 44 amu/q is 10.5 ± 0.2 eV, and for 85 amu/q is 10.2 ± 0.2 eV. PIE curve for 126 amu/q is fitted with a sum of three functions ($\sum_i 0.5\alpha(E-E_{0,i})^2$) where each of the three components of $E_{0,i}$ corresponds to each ionization threshold of (1) 8.3 ± 0.4 eV, (2) 9.6 ± 0.2 eV, and (3) 10.7 ± 0.1 eV.

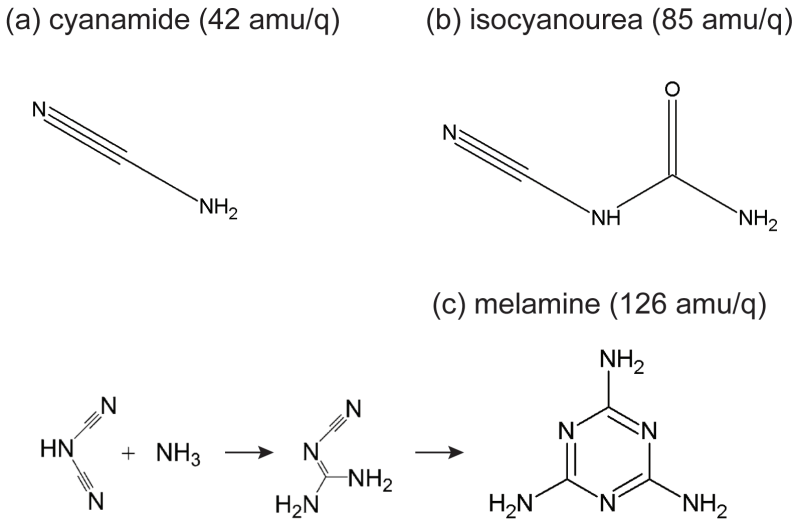

Figure 6.8. Molecular structure of reaction products (a) cyanamide (42 amu/q), (b) isocyanourea (85 amu/q), and (c) melamine (126 amu/q). Previously suggested[164] reaction mechanism for the formation of melamine (126 amu/q) during the hypergolic reaction is shown as well.

A reaction product with mass 126 amu/q is also observed at a very low signal (5% of mass 42 amu/q). Its experimentally obtained PIE curve is shown in Figure 6.7(d) with raw data in solid circles (○) and its total fitted function in solid red line (−). The raw data is fitted with the sum of the three functional forms ($\sum_i 0.5\alpha(E-E_{0,i})^2$) in order to include the ionization component to the ground state, first excited, and second excited state of the ion. Three of the fitted functions are individually shown in black, blue, and red solid lines indicating the ionization threshold of the three components. The three ionization thresholds are 8.3 ± 0.4 (IP_1), 9.6 ± 0.2 (IP_2), and 10.7 ± 0.1 eV (IP_3). This matches well with the calculated IPs of 8.4 ± 0.4 (IP_1), 9.7 ± 0.4 (IP_2), and 10.6 ± 0.4 eV (IP_3) corresponding to the ionization from the ground state of the neutral molecule to the ground state (black), first excited state (blue), and second excited state (red) of the ion, respectively, for melamine ($C_3H_6N_6$). Melamine was previously shown[164] to be produced from the protonated dicyanamide, which is the protonated intact anion, through reaction with ammonia to yield cyanoguanidine, which then polymerizes into melamine. This mechanism is shown in Figure 6.8(c). The trace of ammonia in our system shown in Figure 6.6 from the introduction of nitric acid supports that the melamine can be produced through a side reaction[164] with ammonia that competes with the hypergolic oxidation mechanism.

Based on the observation of the two reaction products, cyanamide and isocyanourea, a reaction mechanism (Scheme 6.1) for the oxidation reaction is proposed:

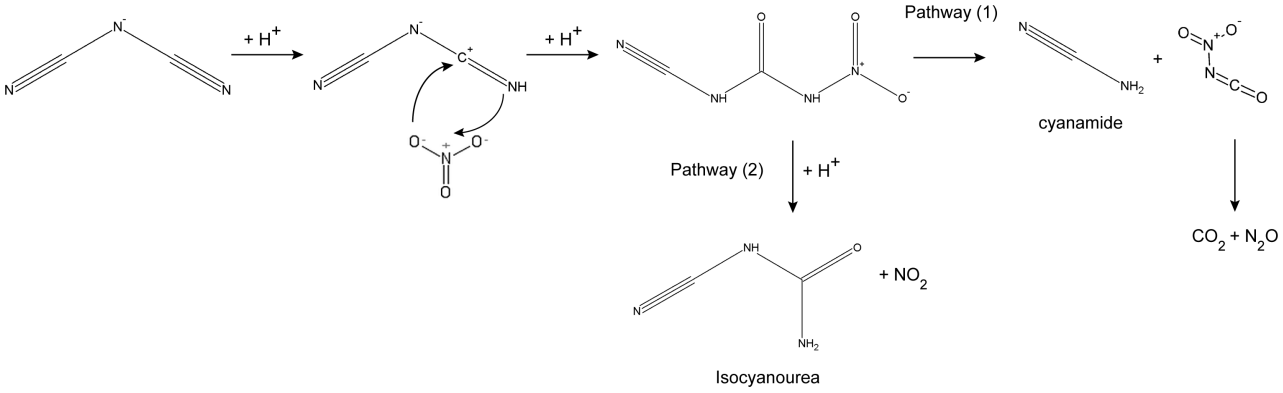

Scheme 6.1

The initial steps are the same as the suggested mechanism from previous studies.[23, 163] The dicyanamide anion is protonated first, and then the nucleophile NO_3^- attacks the electrophile carbon on the protonated anion. This forms the nitro-substituted intermediate ($C_2N_4O_3H_2$), which was suggested in the previously proposed mechanism.[23, 163] The nitro-substituted intermediate can decompose following several different pathways[163] including the formation of cyanamide as shown in the above proposed mechanism Pathway (1) in Scheme 6.1. This is the first time cyanamide is directly observed in the hypergolic reaction of a dicyanamide system with nitric acid. Previously, it was suggested[23] by Chambreau *et al*. that the nitro-substituted intermediate reacts furthermore with additional nitric acid and forms the dinitrobiuret (DNB) anion, and there was no experimental evidence of the nitro-substituted intermediate or cyanamide. However, in this study the reaction time is limited and the condensed phase products are probed allowing captures all the reaction intermediates, unlike previous studies.[23, 163] It is very likely that the

nitro-substituted intermediate is captured and that the cyanamide is observed as a decomposition product. The counter decomposition products, CO_2 and N_2O, are investigated as well, which will be discussed later, in order to confirm this pathway. Cyanamide can also be formed by a decomposition of the isocyanourea (85 amu/q) that is observed. However, the counter product, HNCO, of cyanamide upon decomposition of isocyanourea has not been detected under the reaction conditions here.

Isocyanourea can be formed from the nitro-substituted intermediate ($C_2N_4O_3H_2$) by an addition of a proton as shown in the proposed mechanism Pathway (2) in Scheme 6.1. Another possible pathway (Scheme 6.2) for the isocyanourea to be formed is by an addition of a water molecule instead of a NO_3^-:

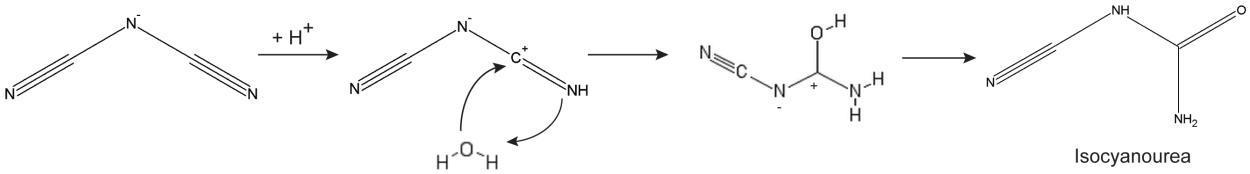

Scheme 6.2

Similarly to the first proposed mechanism in Scheme 6.1, the water molecule (H_2O) attacks the electrophile carbon on the protonated anion and forms the isocyanourea. It is possible that the isocyanourea is formed by water instead of NO_3^- because there is some water left in the aerosol particles even though they go through a diffusion dryer. The water content remaining in the particle is quantitatively measured by monitoring the particle size as a function of temperature assuming that the particle will shrink when water is removed by going through the heated dryer (thermodenuder).

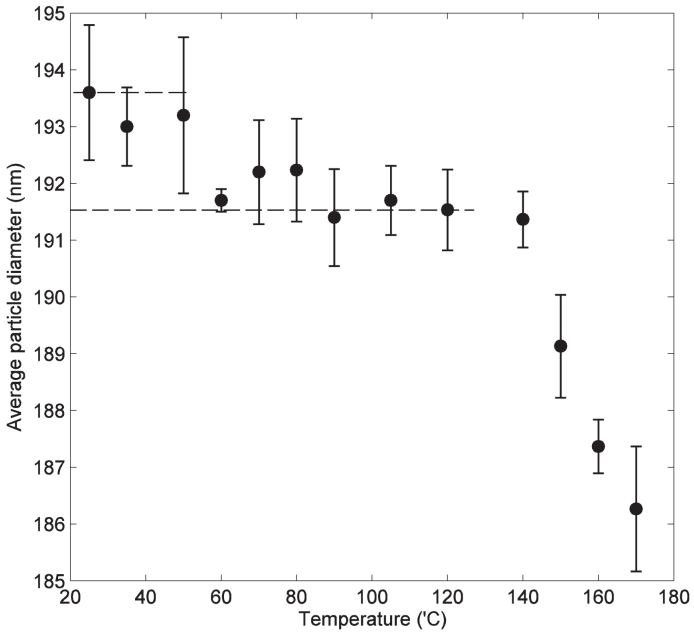

Figure 6.9. IL, [Emim$^+$][Tf_2N^-], aerosol particle size change upon the temperature change of the heated dryer (thermodenuder). Dotted lines are the particle size at 25°C and 120°C, respectively.

The size change of [Emim$^+$][Tf$_2$N$^-$] aerosol particle upon heating is shown in Figure 6.9. The two dotted lines show the initial particle size (193.7 nm) at 25°C and the final size (191.5 nm) after water removal at 120°C. The abrupt drop of aerosol particle size after 140°C is because the ionic liquid, [Emim$^+$][Tf$_2$N$^-$], starts vaporizing from the particle. It is assumed that the difference between the two dotted lines is due to the water loss only and that there are only ionic liquid molecules left at 120°C. The number of ionic liquid molecules (N^{IL}) and water molecules (N^{sol}) are calculated from the difference of volume (particle size) using the following equations:

$$N^{IL} = V^{IL} \times 10^{-21} \times {d(IL) \times N_A}/{MW(IL)} \pm \sigma_V^{IL} \times 10^{-21} \times {d(IL) \times N_A}/{MW(IL)} \quad (6.1)$$

$$N^{Sol} = V^{Sol} \times 10^{-21} \times {d(Solvent) \times N_A}/{MW(Solvent)} \pm \sigma_V^{Sol} \times 10^{-21} \times {d(Solvent) \times N_A}/{MW(Solvent)} \quad (6.2)$$

where V_{IL} is the volume of the particle at 120°C, V_{sol} is the V_{IL} subtracted from the volume of the initial particle at 25°C, σ is the error of the measured volume, d(IL) and d(solvent) are the densities. It has been found that there is 40 ± 28% of water in the IL aerosol particle. It is not surprising that the IL aerosol particle contains significant amount of water considering the hygroscopic nature of the ionic liquid and that the hygroscopic growth of IL particles was observed in a previous study.[166]

Knowing that water can actually be a reactant in the hypergolic reaction, more water is systematically added to the hypergolic reaction (ionic liquid aerosol and nitric acid) to determine whether isocyanourea is formed by water or not. A small amount of nitric acid (0.2% flow of the total flow) is needed to initiate the reaction by protonating the anion (Scheme 6.2) and the amount of water is varied. The ion yield of mass 85 amu/q is monitored as a function of water amount as shown in Figure 6.10.

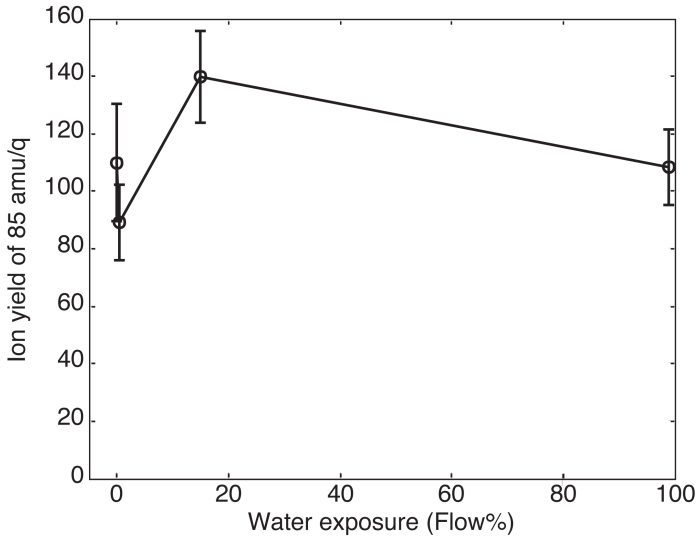

Figure 6.10. Ion yield of mass 85 amu/q (isocyanourea) as a function of water exposure in the hypergolic reaction with IL aerosol and 0.2% of nitric acid.

The result shows that the yield of the isocyanourea product (85 amu/q) is not increased by the addition of water in the hypergolic reaction. This indicates that the isocyanourea reaction product is most likely formed from nitric acid rather than from water. NO_3^- is a stronger nucleophile than H_2O allowing the reaction to favor the formation of the nitro-substituted intermediate. However, it is possible that the water content is already enough in the aerosol particle that more water does not affect the ion yield. Further studies in the future using isotope labeled nitric acid $HN^{18}O_3$ will allow confirmation of whether the isocyanourea results from nitric acid or water. The oxygen on isocyanourea will be isotope labeled by the isotope labeled nitric acid $HN^{18}O_3$ causing the mass peak to shift by 2 amu/q if the product is formed through the route of Scheme 6.1 Pathway (2).

Furthermore, reaction products of volatile species were monitored at lower copper heater block temperature of 323 K to find counter products of the condensed phase products, especially cyanamide (42 amu/q). Mass 44 amu/q peak increases relative to the other reaction products (42, and 85 amu/q) in the low temperature measurements because the condensed phase products are not vaporized as much as the volatile species. If the observed condensed phase products are produced through the nitro-substituted intermediate as proposed, the volatile fragment with mass 44 amu/q is presumably CO_2 and/or N_2O as seen in previous studies, and a counter product of the condensed phase product. Mass 45 amu/q, a 1 amu/q shift of 44 amu/q, is observed when isotope labeled nitric acid ($H^{15}NO_3$) is used during the hypergolic reaction (Figure 6.11). This is because one of the nitrogens from N_2O results from the heavy nitrogen (^{15}N) of nitric acid when N_2O is formed through the nitro-substituted intermediate (Scheme 6.1 Pathway(1)). Appearance of 47 amu/q is $^{15}NO_2^+$ due to the dissociative ionization of the heavy nitric acid ($H^{15}NO_3$).

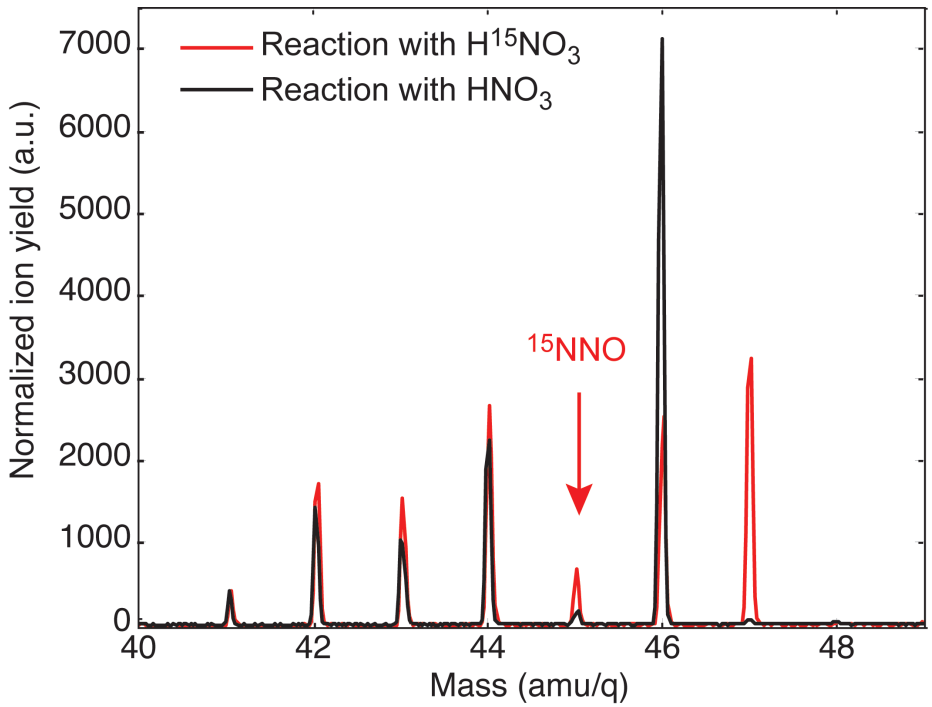

Figure 6.11. Mass spectrum of hypergolic reaction products obtained at copper heater block temperature of 323 K and using isotope labeled nitric acid ($H^{15}NO_3$) (in red solid line) or normal nitric acid (in black solid line) as a reactant.

The mass shift of 44 amu/q (N_2O) to 45 amu/q (^{15}NNO) by using isotope labeled nitric acid strongly indicates that the mass 45 amu/q is ^{15}NNO, and the collected PIE curves of mass 44 amu/q (Figure 6.12(a)) and 45 amu/q (Figure 6.12(b)) confirm the identity of these volatile reaction products. The mass 44 amu/q product with low ionization threshold of 10.5 eV, yet unknown, is still seen at the lower temperature of the heater block. The CO_2 feature (dotted line in (a)), peak at 13.7 ev, is clearly observed in the PIE curve of the reaction product (sold line in (a)) as well.

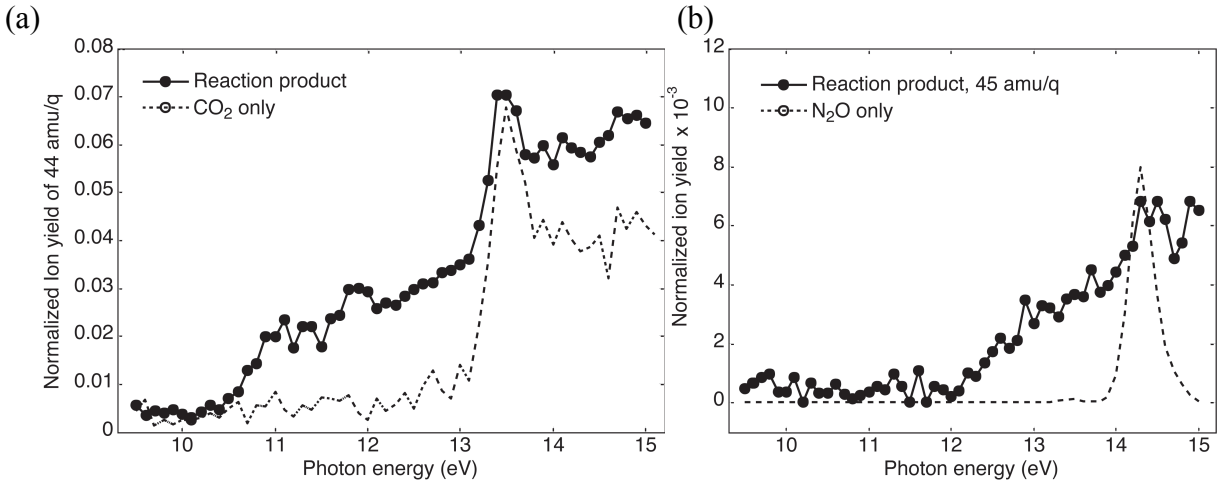

Figure 6.12. PIE curves of (a) mass 44 amu/q and (b) mass 45 amu/q collected at a copper heater block temperature of 323 K for the hypergolic reaction using isotope labeled nitric acid ($H^{15}NO_3$). In both figures solid lines with solid circles show the PIE curves of the reaction product whereas the dotted lines are showing the PIE curves of calibration gases, CO_2 (44 amu/q) and N_2O (44 amu/q).

The PIE curve of mass 45 amu/q from the reaction using isotope labeled nitric acid ($H^{15}NO_3$) reveals two components, one with an ionization threshold around 12 eV and the other with a peak around 14.3 eV. It requires more analysis of the data and all possible reaction mechanisms to find out what the reaction product with IP of 12 eV is. However the N_2O feature (dotted line in (b)), peak at 14.3 eV, is observed in the PIE curve of mass 45 amu/q indicating the formation of ^{15}NNO in the hypergolic reaction with the isotope labeled nitric acid ($H^{15}NO_3$). Therefore, it is concluded that there is production of CO_2 and N_2O in the hypergolic reaction of [$Bmim^+$][Dca^-] with nitric acid and that these are very likely to be a counter products to cyanamide (NH_2CN) according to the proposed mechanism (Scheme 6.1). This is the first direct evidence for the existence of the nitro-substituted intermediate, which is an early stage intermediate in the hypergolic reaction.

There is an indication of NO_2 (46 amu/q) formation in the hypergolic reaction during the volatile species detection (Figure 6.11). It is produced from dissociative ionization of HNO_3 with an appearance energy of 11.9 ± 0.1 eV, which agrees well with the NIST webbook value. It is not clear though if NO_2 is also produced upon the hypergolic reaction as a counter product of isocyanourea. The product NO_2 would have an IP of 9.586 ± 0.002 eV, but as the PIE curves are collected from 9.5 eV with low signal-to-noise it is not clear whether NO_2 product is formed or

not. It will be more clear how isocyanourea is formed when NO_2 is detected with a PIE curve measured from lower photon energies. Also using $HN^{18}O_3$ in the future will provide better results by shifting the NO_2 mass by 4 amu/q to 50 amu/q, which is a background free mass.

6.2.4 Conclusion

Hypergolic reaction of ionic liquid, $[Bmim^+][Dca^-]$, with nitric acid is studied using the aerosol flow tube method. The reaction intermediates/products are monitored after mixing the IL aerosol particles with nitric acid vapor using tunable vacuum ultraviolet (VUV) mass spectrometry detection. From photoionization efficiency measurements of reaction products, cyanamide (42 amu/q) is observed for the first time as an intermediate species in the hypergolic reaction. The counter products of cyanamide, N_2O and CO_2, which are volatile, are observed as well. This provides evidence for the existence of an early stage intermediate, nitro-substituted intermediate ($C_2N_4O_3H_2$), which was suggested previously but never seen experimentally. Isocyanourea (85 amu/q) is detected as well, but the reaction pathway is still debatable, whether through protonation of nitro-substituted intermediate or water addition to the protonated anion. Further investigation of other reaction products including the protonated anion, dinitrobiuret, and NO_2, as well as reaction kinetics studies will provide complete insight on how the dicyanamide ionic liquid undergoes fast ignition when reacted with nitric acid.

- Acknowledgments

The authors gratefully acknowledge funding from the U.S. Air Force Office of Scientific Research for supporting CK, and SL (Grant No. FA9550-10-1-0163), and for SC and GV (Grant No. FA9300-06-C-0023). This work at the ALS was supported by the Director, Office of Energy Research, Office of Basic Energy Sciences, Chemical Sciences Division of the U.S. Department of Energy under Contract No. DE-AC02-05CH11231 (DP, AG, and SL). The authors thank Dr. Musahid Ahmed and Dr. Kevin Wilson of the Chemical Dynamics Beamline for help in the measurements.

Chapter 7

Summary and Outlook

Ionic liquds that exhibit unique properties and are applicable in many different fields are tunable materials. To find the best matching ionic liquid for specific tasks among the vast number of ionic liquids, it is valuable to understand the fundamental properties such as their photophysics and reactivity. Understanding the building block (ion−pair) of the complex system will provide a simple picture that can extend the knowledge to complex systems. The building block for ionic liquids, isolated ion pairs, consist of an intact cation and an intact anion, which are contained in the ionic liquid vapor. The studies discussed in Chapters 3−4 aimed to learn about the excited state nature of these isolated ion pairs, and in Chapter 5−6 focused to investigate several aspects of thermo dynamical properties, and to explore the reaction dynamics by monitoring the isolated ion pairs using extreme ultraviolet light as a universal probe in all the studies:

- In Chapter 3, the dissociative pathways upon photoexcitation of isolated ion pairs of imidazolium-based ionic liquids are explored. The results revealed a new ion pair dissociation pathway of an IL, $[Emim^+][Tf_2N^-]$, as well as the previously suggested dissociative ionization pathway by probing the intact cation and/or intact anion using velocity map ion imaging. Not only does this study reveal a previously unobserved photodissociation pathway, but it also provides direct evidence for the existence of the ion pairs in the isolated gas phase molecules.

- In Chapter 4, ultrafast excited state dynamics of isolated ion pairs of an imidazolium-based ionic liquid is discussed. The first time-resolved results of an ionic liquid that are probed along ultrafast timescales using ultrafast extreme ultraviolet light combined with time-resolved photoion spectroscopy is reported. It generally suggests a short-lived electronically or internally vibrationally excited state dynamics that is initiated by multiphoton absorption.

- In Chapter 5, studies of thermal properties of ionic liquids using tunable vacuum ultraviolet light are described. Monitoring the isolated ion pairs by soft ionization allowed successful measurements of heats of vaporization of several ionic liquids despite their extremely low vapor pressure and a photoionization efficiency curve of a neutral, intact ion pair is obtained for the first time. Also the thermal decomposition mechanism of an ionic liquid is explored providing better understanding of the volatilization process for ionic liquids.

- In Chapter 6, the reaction dynamics of hypergolic ionic liquids using an aerosol flow tube method is described. It is shown that the isolated ion pairs are generated with less internal energy by vaporizing ionic liquid submicron aerosol particles for the first time. Using these aerosol particles, the hypergolic reaction of an ionic liquid with nitric acid is studied. The

results reveal a nitro−substituted intermediate in the early stage of the hypergolic reaction by simultaneous measurement of condensed phase and gas phase reaction intermediates.

So far photophysics, thermal properties, and reaction dynamics of ionic liquids are investigated and have provided a substantial amount of new information on the ionic liquid system. Most importantly, the obtained knowledge on the excited state dynamics upon photoexcitation are valuable for application of ionic liquids in the field of photochemistry, and the reaction dynamics of a hypergolic ionic liquid is useful in the propellant field. More investigation on different ionic liquid systems such as ammonium- or aluminum- based ionic liquids will extend the knowledge and increase the database.

In the future, excited state dynamics of various ionic liquid systems should be explored, as the interaction between the ions may primarily determine the electronic and nuclear structure. Hypergolic reaction dynamics of ionic liquids with several different oxidizers, such as H_2O_2, NO_2, and O_3, should be investigated as well to find the most essential step for hypergolic ignition. These basic understandings can ultimately facilitate the search for a green rocket fuel in the future.

Bibliography

1. Wasserscheid, P.; W., T., *Ionic liquids in synthesis*. 2 ed.; Wiley-VCH, Weinheim: 2007; p 724.
2. Walden, P., *Bulletin de l'Academie Imperiale des Sciences de St. Petersbourg* **1914,** (6), 405-422422.
3. Chum, H. L.; Koch, V. R.; Miller, L. L.; Osteryoung, R. A., *J. Am. Chem. Soc.* **1975,** *97* (11), 3264-3265.
4. Wilkes, J. S.; Levisky, J. A.; Wilson, R. A.; Hussey, C. L., *Inorg. Chem.* **1982,** *21* (3), 1263-1264.
5. Aparicio, S.; Atilhan, M.; Karadas, F., *Ind. Eng. Chem. Res.* **2010,** *49* (20), 9580-9595.
6. Castner, E. W.; Wishart, J. F., *J. Chem. Phys.* **2010,** *132* (12), 9.
7. Chiappe, C.; Pieraccini, D., *J. Phys. Org. Chem.* **2005,** *18* (4), 275-297.
8. Esperanca, J.; Lopes, J. N. C.; Tariq, M.; Santos, L.; Magee, J. W.; Rebelo, L. P. N., *J. Chem. Eng. Data* **2010,** *55* (1), 3-12.
9. Welton, T., *Chem. Rev. (Washington, DC, U. S.)* **1999,** *99* (8), 2071-2083.
10. Rogers, R. D.; Seddon, K. R., *Science* **2003,** *302* (5646), 792-793.
11. Pandey, S., *Anal. Chim. Acta* **2006,** *556* (1), 38-45.
12. Silvester, D. S.; Compton, R. G., *Zeitschrift Fur Physikalische Chemie-International Journal of Research in Physical Chemistry & Chemical Physics* **2006,** *220* (10-11), 1247-1274.
13. Endres, F.; El Abedin, S. Z., *Phys. Chem. Chem. Phys.* **2006,** *8* (18), 2101-2116.
14. Torimoto, T.; Tsuda, T.; Okazaki, K.; Kuwabata, S., *Adv. Mater. (Weinheim, Ger.)* **2010,** *22* (11), 1196-1221.
15. Olivier-Bourbigou, H.; Magna, L.; Morvan, D., *Applied Catalysis a-General* **2010,** *373* (1-2), 1-56.
16. Armand, M.; Endres, F.; MacFarlane, D. R.; Ohno, H.; Scrosati, B., *Nat. Mater.* **2009,** *8* (8), 621-629.
17. Hu, Y. S.; Li, H.; Huang, X. J.; Chen, L. Q., *Electrochem. Commun.* **2004,** *6* (1), 28-32.
18. Shin, J. H.; Henderson, W. A.; Passerini, S., *Electrochem. Commun.* **2003,** *5* (12), 1016-1020.
19. Schneider, S.; Hawkins, T.; Ahmed, Y.; Rosander, M.; Hudgens, L.; Mills, J., *Angewandte Chemie-International Edition* **2011,** *50* (26), 5886-5888.
20. Schneider, S.; Hawkins, T.; Rosander, M.; Vaghjiani, G.; Chambreau, S.; Drake, G., *Energy Fuels* **2008,** *22* (4), 2871-2872.
21. Plechkova, N. V.; Seddon, K. R., *Chem. Soc. Rev.* **2008,** *37* (1), 123-150.
22. Jones, C. B.; Haiges, R.; Schroer, T.; Christe, K. O., *Angewandte Chemie-International Edition* **2006,** *45* (30), 4981-4984.
23. Chambreau, S. D.; Schneider, S.; Rosander, M.; Hawkins, T.; Gallegos, C. J.; Pastewait, M. F.; Vaghjiani, G. L., *J. Phys. Chem. A* **2008,** *112* (34), 7816-7824.
24. Joo, Y. H.; Gao, H. X.; Zhang, Y. Q.; Shreeve, J. M., *Inorg. Chem.* **2010,** *49* (7), 3282-3288.
25. Schneider, S.; Hawkins, T.; Rosander, M.; Mills, J.; Vaghjiani, G.; Chambreau, S., *Inorg. Chem.* **2008,** *47* (13), 6082-6089.

26. Earle, M. J.; Esperanca, J.; Gilea, M. A.; Lopes, J. N. C.; Rebelo, L. P. N.; Magee, J. W.; Seddon, K. R.; Widegren, J. A., *Nature* **2006,** *439* (7078), 831-834.
27. Strasser, D.; Goulay, F.; Kelkar, M. S.; Maginn, E. J.; Leone, S. R., *J. Phys. Chem. A* **2007,** *111* (17), 3191-3195.
28. Strasser, D.; Goulay, F.; Belau, L.; Kostko, O.; Koh, C.; Chambreau, S. D.; Vaghjiani, G. L.; Ahmed, M.; Leone, S. R., *J. Phys. Chem. A* **2010,** *114* (2), 879-883.
29. Armstrong, J. P.; Hurst, C.; Jones, R. G.; Licence, P.; Lovelock, K. R. J.; Satterley, C. J.; Villar-Garcia, I. J., *Phys. Chem. Chem. Phys.* **2007,** *9* (8), 982-990.
30. Krischok, S.; Ottking, R.; Beenken, W. J. D.; Himmerlich, M.; Lorenz, P.; Hofft, O.; Bahr, S.; Kempter, V.; Schaefer, J. A., *Zeitschrift Fur Physikalische Chemie-International Journal of Research in Physical Chemistry & Chemical Physics* **2006,** *220* (10-11), 1407-1416.
31. Hofft, O.; Bahr, S.; Himmerlich, M.; Krischok, S.; Schaefer, J. A.; Kempter, V., *Langmuir* **2006,** *22* (17), 7120-7123.
32. Koh, C. J.; Liu, C. L.; Harmon, C. W.; Strasser, D.; Golan, A.; Kostko, O.; Chambreau, S. D.; Vaghjiani, G. L.; Leone, S. R., *J. Phys. Chem. A* **2011,** *115* (18), 4630-4635.
33. Lovelock, K. R. J.; Deyko, A.; Corfield, J.-A.; Gooden, P. N.; Licence, P.; Jones, R. G., *ChemPhysChem* **2009,** *10* (2), 337-340.
34. Wang, C. M.; Luo, H. M.; Li, H. R.; Dai, S., *Phys. Chem. Chem. Phys.* **2010,** *12* (26), 7246-7250.
35. Leal, J. P.; Esperanca, J.; da Piedade, M. E. M.; Lopes, J. N. C.; Rebelo, L. P. N.; Seddon, K. R., *J. Phys. Chem. A* **2007,** *111* (28), 6176-6182.
36. Attwood, D., *Soft X-rays and Extreme Ultraviolet Radiation: Principles and Applications*. Cambridge University Press: United States of America by Cambridge University Press, New York, 2007; p 504.
37. Ivanov, M. Y.; Corkum, P. B., *Phys. Rev. A* **1993,** *48* (1), 580-590.
38. Corkum, P. B., *Phys. Rev. Lett.* **1993,** *71* (13), 1994-1997.
39. Nugent-Glandorf, L.; Scheer, M.; Samuels, D. A.; Bierbaum, V.; Leone, S. R., *Rev. Sci. Instrum.* **2002,** *73* (4), 1875-1886.
40. Belau, L.; Wilson, K. R.; Leone, S. R.; Ahmed, M., *J. Phys. Chem. A* **2007,** *111* (31), 7562-7568.
41. Belau, L.; Wilson, K. R.; Leone, S. R.; Ahmed, M., *J. Phys. Chem. A* **2007,** *111* (40), 10075-10083.
42. Kwiatkowski, S.; Baptiste, K. In *ALS Booster Ring RF System Upgrade for Top-Off Mode of Operation*, Proceedings of 2005 Particle Accelerator Conference, Knoxville, Tennessee, IEEE: Knoxville, Tennessee, 2005; pp 3709-3711.
43. Wilson, K. R.; Jimenez-Cruz, M.; Nicolas, C.; Belau, L.; Leone, S. R.; Ahmed, M., *J. Phys. Chem. A* **2006,** *110* (6), 2106-2113.
44. Blanchard, L. A.; Hancu, D.; Beckman, E. J.; Brennecke, J. F., *Nature* **1999,** *399* (6731), 28-29.
45. de Souza, R. F.; Padilha, J. C.; Goncalves, R. S.; Dupont, J., *Electrochem. Commun.* **2003,** *5* (8), 728-731.
46. Susan, M.; Noda, A.; Mitsushima, S.; Watanabe, M., *Chem. Commun. (Cambridge, U. K.)* **2003,** (8), 938-939.
47. Wang, P.; Wenger, B.; Humphry-Baker, R.; Moser, J. E.; Teuscher, J.; Kantlehner, W.; Mezger, J.; Stoyanov, E. V.; Zakeeruddin, S. M.; Gratzel, M., *J. Am. Chem. Soc.* **2005,** *127* (18), 6850-6856.

48. Wang, P.; Zakeeruddin, S. M.; Comte, P.; Exnar, I.; Gratzel, M., *J. Am. Chem. Soc.* **2003,** *125* (5), 1166-1167.
49. Wilkes, J. S., *Green Chem.* **2002,** *4* (2), 73-80.
50. Yoshizawa, M.; Xu, W.; Angell, C. A., *J. Am. Chem. Soc.* **2003,** *125* (50), 15411-15419.
51. He, L.; Tao, G. H.; Parrish, D. A.; Shreeve, J. M., *Chemistry-a European Journal* **2009,** *16* (19), 5736-5743.
52. Akai, N.; Parazs, D.; Kawai, A.; Shibuya, K., *J. Phys. Chem. B* **2009,** *113* (14), 4756-4762.
53. Chambreau, S. D.; Vaghjiani, G. L.; To, A.; Koh, C.; Strasser, D.; Kostko, O.; Leone, S. R., *J. Phys. Chem. B* **2010,** *114* (3), 1361-1367.
54. Gross, J. H., *J. Am. Soc. Mass Spectrom.* **2008,** *19* (9), 1347-1352.
55. Kelkar, M. S.; Maginn, E. J., *J. Phys. Chem. B* **2007,** *111* (32), 9424-9427.
56. Lovelock, K. R. J.; Deyko, A.; Corfield, J. A.; Gooden, P. N.; Licence, P.; Jones, R. G., *ChemPhysChem* **2009,** *10* (2), 337-340.
57. Ludwig, R.; Kragl, U., *Angewandte Chemie-International Edition* **2007,** *46* (35), 6582-6584.
58. Vitorino, J.; Leal, J. P.; Licence, P.; Lovelock, K. R. J.; Gooden, P. N.; da Piedade, M. E. M.; Shimizu, K.; Rebelo, L. P. N.; Lopes, J. N. C., *ChemPhysChem* **2010,** *11* (17), 3673-3677.
59. Koddermann, T.; Ludwig, R.; Paschek, D., *ChemPhysChem* **2008,** *9* (13), 1851-1858.
60. Bhargava, B. L.; Balasubramanian, S., *J. Am. Chem. Soc.* **2006,** *128* (31), 10073-10078.
61. Picalek, J.; Minofar, B.; Kolafa, J.; Jungwirth, P., *Phys. Chem. Chem. Phys.* **2008,** *10* (37), 5765-5775.
62. Fumino, K.; Wulf, A.; Ludwig, R., *Angewandte Chemie-International Edition* **2008,** *47* (20), 3830-3834.
63. Ballone, P.; Pinilla, C.; Kohanoff, J.; Del Popolo, M. G., *J. Phys. Chem. B* **2007,** *111* (18), 4938-4950.
64. Koddermann, T.; Paschek, D.; Ludwig, R., *ChemPhysChem* **2007,** *8* (17), 2464-2470.
65. Gebhardt, C. R.; Rakitzis, T. P.; Samartzis, P. C.; Ladopoulos, V.; Kitsopoulos, T. N., *Rev. Sci. Instrum.* **2001,** *72* (10), 3848-3853.
66. Townsend, D.; Minitti, M. P.; Suits, A. G., *Rev. Sci. Instrum.* **2003,** *74* (4), 2530-2539.
67. Eppink, A.; Parker, D. H., *Rev. Sci. Instrum.* **1997,** *68* (9), 3477-3484.
68. Suits, A. G.; Hepburn, J. W., Ion pair dissociation: Spectroscopy and dynamics. In *Annu. Rev. Phys. Chem.*, Annual Reviews: Palo Alto, 2006; Vol. 57, pp 431-465.
69. Doughty, B.; Haber, L. H.; Hackett, C.; Leone, S. R., *J. Chem. Phys.* **2011,** *134* (9).
70. Haber, L. H.; Doughty, B.; Leone, S. R., *J. Phys. Chem. A* **2009,** *113* (47), 13152-13158.
71. Haber, L. H.; Doughty, B.; Leone, S. R., *Phys. Rev. A* **2009,** *79* (3).
72. Haber, L. H.; Doughty, B.; Leone, S. R., *Mol. Phys.* **2010,** *108* (7-9), 1241-1251.
73. Haber, L. H.; Doughty, B.; Leone, S. R., *Phys. Rev. A* **2011,** *84* (1), 9.
74. Chambreau, S. D.; Boatz, J. A.; Vaghjiani, G. L.; Koh, C.; Kostko, O.; Golan, A.; Leone, S. R., *J. Phys. Chem. A* **2012,** *116* (24), 5867-5876.
75. Kobrak, M. N., The Chemical Environment of Ionic Liquids: Links Between Liquid Structure, Dynamics, and Solvation. In *Adv. Chem. Phys.*, John Wiley & Sons, Inc.: 2008; pp 85-138.
76. Zakeeruddin, S. M.; Gratzel, M., *Adv. Funct. Mater.* **2009,** *19* (14), 2187-2202.
77. Di Noto, V.; Negro, E.; Sanchez, J. Y.; Iojoiu, C., *J. Am. Chem. Soc.* **2010,** *132* (7), 2183-2195.
78. Kim, S. Y.; Kim, S.; Park, M. J., *Nature Communications* **2010,** *1*.

79. Yasuda, T.; Ogawa, A.; Kanno, M.; Mori, K.; Sakakibara, K.; Watanabe, M., *Chem. Lett.* **2009,** *38* (7), 692-693.
80. Gao, H. X.; Joo, Y. H.; Twamley, B.; Zhou, Z. Q.; Shreeve, J. M., *Angewandte Chemie-International Edition* **2009,** *48* (15), 2792-2795.
81. Chambreau, S. D.; Vaghjiani, G. L.; Koh, C. J.; Golan, A.; Leone, S. R., *Journal of Physical Chemistry Letters* **2012,** *3* (19), 2910-2914.
82. Koh, C. J.; Leone, S. R., *Mol. Phys.* **2012,** *110* (15-16), 1705-1712.
83. Paul, A.; Samanta, A., *J. Chem. Sci. (Bangalore, India)* **2006,** *118* (4), 335-340.
84. Jayabharathi, J.; Thanikachalam, V.; Perumal, M. V.; Srinivasan, N., *J. Fluoresc.* **2012,** *22* (1), 409-417.
85. Leal, J. o. P.; da Piedade, M. E. M.; Canongia Lopes, J. N.; Tomaszowska, A. A.; Esperança, J. M. S. S.; Rebelo, L. s. P. N.; Seddon, K. R., *The Journal of Physical Chemistry B* **2009,** *113* (11), 3491-3498.
86. Rebelo, L. P. N.; Canongia Lopes, J. N.; Esperança, J. M. S. S.; Filipe, E., *The Journal of Physical Chemistry B* **2005,** *109* (13), 6040-6043.
87. Zaitsau, D. H.; Verevkin, S. P.; Paulechka, Y. U.; Kabo, G. J.; Sevruk, V. M., *J. Chem. Eng. Data* **2003,** *48*, 1393-1400.
88. Emel'yanenko, V. N.; Verevkin, S. P.; Heintz, A., *J. Am. Chem. Soc.* **2007,** *129* (13), 3930-3937.
89. Paulechka, Y. U.; Kabo, G. J.; Blokhin, A. V.; Vydrov, O. A.; Magee, J. W.; Frenkel, M., *J. Chem. Eng. Data* **2003,** *48*, 457-462.
90. Paulechka, Y. U.; Zaitsau, D. H.; Kabo, G. J.; Strechan, A. A., *Thermochim. Acta* **2005,** *439*, 158-160.
91. Zaitsau, D. H.; Kabo, G. J.; Strechan, A. A.; Paulechka, Y. U.; Tscherisch, A.; Verevkin, S. P.; Heintz, A., *J. Phys. Chem. A* **2006,** *110*, 7303-7306.
92. Dzyuba, S. V.; Bartsch, R. A., *ChemPhysChem* **2002,** *3*, 161-166.
93. Ngo, H. L.; LeCompte, K.; Hargens, L.; McEwen, A. B., *Thermochim. Acta* **2000,** *357-358*, 97-102.
94. Wooster, T. J.; Johanson, K. M.; Fraser, K. J.; MacFarlane, D. R.; Scott, J. L., *Green Chem.* **2006,** *8*, 691-696.
95. Emel'yanenko, V. N.; Verevkin, S. P.; Heintz, A.; Corfield, J.-A.; deyko, A.; Lovelock, K. R. J.; Licence, P.; Jones, R. G., *J. Phys. Chem. B* **2008,** *112*, 11734-11742.
96. de Andrade, J.; Böes, E. S.; Stassen, H., *J. Phys. Chem. B* **2002,** *106*, 13344-13351.
97. Köddermann, T.; Paschek, D.; Ludwig, R., *ChemPhysChem* **2008,** *9*, 549-555.
98. Kroon, M. C.; Buijs, W.; Peters, C. J.; Witkamp, G.-J., *Thermochim. Acta* **2007,** *465*, 40-47.
99. Gross, J. H., *J. Am. Soc. Mass Spectrom.* **2008,** *19*, 1347-1352.
100. Frisch, M. J. T., G. W.; Schlegel, H. B.; Scuseria, G. E.; Robb, M. A.; Cheeseman, J. R.; Scalmani, G.; Barone, V.; Mennucci, B.; Petersson, G. A.; Nakatsuji, H.; Caricato, M.; Li, X.; Hratchian, H. P.; Izmaylov, A. F.; Bloino, J.; Zheng, G.; Sonnenberg, J. L.; Hada, M.; Ehara, M.; Toyota, K.; Fukuda, R.; Hasegawa, J.; Ishida, M.; Nakajima, T.; Honda, Y.; Kitao, O.; Nakai, H.; Vreven, T.; Montgomery, J. A., Jr.; Peralta, J. E.; Ogliaro, F.; Bearpark, M.; Heyd, J. J.; Brothers, E.; Kudin, K. N.; Staroverov, V. N.; Kobayashi, R.; Normand, J.; Raghavachari, K.; Rendell, A.; Burant, J. C.; Iyengar, S. S.; Tomasi, J.; Cossi, M.; Rega, N.; Millam, J. M.; Klene, M.; Knox, J. E.; Cross, J. B.; Bakken, V.; Adamo, C.; Jaramillo, J.; Gomperts, R.; Stratmann, R. E.; Yazyev, O.; Austin, A. J.; Cammi, R.; Pomelli, C.; Ochterski, J. W.; Martin, R. L.; Morokuma, K.;

Zakrzewski, V. G.; Voth, G. A.; Salvador, P.; Dannenberg, J. J.; Dapprich, S.; Daniels, A. D.; Farkas, Ö.; Foresman, J. B.; Ortiz, J. V.; Cioslowski, J.; Fox, D. J. *Gaussian 09*, Wallingford, CT, 2009.

101. Gordon, M. S.; Schmidt, M. W., Advances in Electronic Structure Theory: GAMESS a Decade Later. In *Theory and Applications of Computational Chemistry: the First Forty Years*, Dykstra, C. E.; Frenking, G.; Kim, K. S.; Scuseria, G. E., Eds. Elsevier: Amsterdam, 2005; pp 1167-1189.
102. Schmidt, M. W.; Baldridge, K. K.; Boatz, J. A.; Elbert, S. T.; Gordon, M. S.; Jensen, J. H.; Koseki, S.; Matsunaga, N.; Nguyen, K. A.; Su, S.; Windus, T. L.; Dupuis, M.; Montgomery, J. A., *J. Comput. Chem.* **1993,** *14*, 1347-1363.
103. Kelkar, M. S.; Maginn, E. J., *J. Phys. Chem. B* **2007,** *111*, 9424-9427.
104. Leal, J. P.; Minas da Piedade, M. E.; Canongia Lopes, J. N.; Tomaszowska, A. A.; Esperança, J. M. S. S.; Rebelo, L. P. N.; Seddon, K. R., *J. Phys. Chem. B* **2009,** *113*, 3491-3498.
105. Swiderski, K.; McLean, A.; Gordon, C. M.; Vaughn, D. H., *Chem. Commun.* **2004**, 2178-2179.
106. Fredlake, C. P.; Crosthwaite, J. M.; Hert, D. G.; Aki, S. N. V. K.; Brennecke, J. F., *J. Chem. Eng. Data* **2004,** *49* (4), 954-964.
107. Kim, Y.-K.; Hwang, W.; Weinberger, N. M.; Ali, M. A.; Rudd, M. E., *Journal of Chemical Physics* **1996,** *106* (3), 1026-1033.
108. Probst, M.; Deutsch, H.; Becker, K.; Märk, T. D., *Int. J. Mass. Spectrom.* **2001,** *206*, 13-25.
109. Jagoda-Cwiklik, B.; Wang, X.-B.; Woo, H.-K.; Yang, J.; Wang, G.-J.; Zhou, M.; Jungwirth, P.; Wang, L.-S., *J. Phys. Chem. A* **2007,** *111*, 7719-7725.
110. Paulechka, Y. U.; Kabo, A. G.; Blokhin, A. V., *J. Phys. Chem. B* **2009,** *113* (44), 14742-14746.
111. Paulechka, Y. U.; Kabo, G. J.; Blokhin, A. V.; Shaplov, A. S.; Lozinskaya, E. I.; Vygodskii, Y. S., *J. Chem. Thermodyn.* **2007,** *39* (1), 158-166.
112. Vitorino, J.; Leal, J. P.; Minas da Piedade, M. E.; Canongia Lopes, J. N.; Esperança, J. M. S. S.; Rebelo, L. P. N., *J. Phys. Chem. B* **2010,** *114* (27), 8905-8909.
113. Schröder, D.; Duchackova, L.; Jusinski, I.; Eckert-Maksic, M.; Heyda, J., *Chem. Phys. Lett* **2010,** *490*, 14-18.
114. Chambreau, S. D.; Boatz, J. A.; Vaghjiani, G. L.; Friedman, J. F.; Eyet, N.; Viggiano, A. A., *J. Phys. Chem. Lett.* **2011,** *2*, 874-879.
115. Wang, C.; Luo, H.; Li, H.; Dai, S., *PCCP* **2010,** *12* (26), 7246-7250.
116. Emel'yanenko, V. N.; Zaitsau, D. H.; Verevkin, S. P.; Heintz, A.; Vos, K.; Schultz, A., *J. Phys. Chem. B* **2011,** *115* (40), 11712-11717.
117. Ghosh, D.; Golan, A.; Takahashi, L. K.; Krylov, A. I.; Ahmed, M., *Journal of Physical Chemistry Letters* **2012,** *3* (1), 97-101.
118. Lou, H.; Baker, G. A.; Dai, S., *J. Phys. Chem. B* **2008,** *112*, 10077-10081.
119. Mokrushin, V.; Tsang, W. *ChemRate, version 1.5.8*; National Institute of Standards and Technology: Gaithersburg, MD, 2009.
120. Zhao, Y.; Truhlar, D. G., *Theor. Chem. Account.* **2008,** *120*, 215-241.
121. Liu, J.; Chambreau, S. D.; Vaghjiani, G. L., *J. Phys. Chem. A* **2011,** *115* (28), 8064-8072.
122. Friere, M. G.; Neves, C. M. S. S.; Marrucho, I. M.; Canongia Lopes, J. N.; Rebelo, L. P. N.; Coutinho, J. A. P., *Green Chem.* **2010,** *12* (10), 1715-1718.
123. Giunta, D.; Solinas, M., *Curr. Org. Chem.* **2009,** *13* (13), 1300-1321.
124. Sheldon, R., *Chem. Commun.* **2001,** *23*, 2399-2407.

125. Visser, A. E.; Swatloski, R. P.; Griffin, S. T.; Hartman, D. H.; Rogers, R., *Separation Sci. Technol.* **2001,** *36* (5), 785-804.
126. Nakamoto, H.; Noda, A.; Hayamizu, K.; Hayashi, S.; Hamaguchi, H.-o.; Watanabe, M., *The Journal of Physical Chemistry C* **2007,** *111* (3), 1541-1548.
127. Bermudez, M.-D.; Jimenez, A.-E.; Sanes, J.; Carrion, F.-J., *Molecules* **2009,** *14* (8), 2888-2908.
128. Palacio, M.; Brushan, B., *Tribol. Lett.* **2010,** *40* (2), 247-268.
129. Van Renesselar, J., *Tribol. Lubricat. Technol.* **2010,** *66* (4), 24-31.
130. Baranyai, K. J.; Deacon, G. B.; MacFarlane, D. R.; Pringle, J. M.; Scott, J. L., *Aust J Chem* **2004,** *57*, 145-147.
131. Chan, B. K. M.; Chang, N.-H.; Grimmett, M. R., *Aust J Chem* **1977,** *30*, 2005-13.
132. Chowdhury, A.; Thynell, S. T., *Thermochim. Acta* **2006,** *443* (2), 159-172.
133. Handy, S. T.; Okello, M., *J. Org. Chem.* **2005,** *70*, 1915-1918.
134. Breslow, R., *J. Am. Chem. Soc.* **1957,** *79* (7), 1962-1963.
135. Arduengo, A. J.; Harlow, R. L.; Kline, M., *J. Am. Chem. Soc.* **1991,** *113*, 361-363.
136. Breslow, R., *Chemistry and Industry* **1957,** *26*, 893-894.
137. Wanzlick, H. W.; Schonherr, H. J., *Liebigs Ann. Chem.* **1970,** *731*, 176.
138. Kan, H.-C.; Tseng, M.-C.; Chu, Y.-H., *Tetrahedron* **2007,** *63*, 1644-1653.
139. Holloczki, O.; Gerhard, D.; Massone, K.; Szarvas, L.; Nemeth, B.; Veszpremi, T.; Nyulaszi, L., *New Journal of Chemistry* **2010,** *34*, 3004-3009.
140. Koppel, I. A.; Taft, R. W.; Anvia, F.; Hu, L.-Q.; Sung, K.-S.; DesMarteau, D. D.; Yagupolskii, L. M.; Yagupolskii, Y. L.; Ignat'ev, N. V.; Kondratenko, N. V.; volkonskii, A. Y.; Vlasov, V. M.; Notario, R.; Maria, P.-C., *J. Am. Chem. Soc.* **1994,** *116*, 3047-3057.
141. Frisch, M. J.; Trucks, G. W.; Schlegel, H. B.; Scuseria, G. E.; Robb, M. A.; Cheeseman, J. R.; Scalmani, G.; Barone, V.; Mennucci, B.; Petersson, G. A.; Nakatsuji, H.; Caricato, M.; Li, X.; Hratchian, H. P.; Izmaylov, A. F.; Bloino, J.; Zheng, G.; Sonnenberg, J. L.; Hada, M.; Ehara, M.; Toyota, K.; Fukuda, R.; Hasegawa, J.; Ishida, M.; Nakajima, T.; Honda, Y.; Kitao, O.; Nakai, H.; Vreven, T.; Montgomery, J. A., Jr. ; Peralta, J. E.; Ogliaro, F.; Bearpark, M.; Heyd, J. J.; Brothers, E.; Kudin, K. N.; Staroverov, V. N.; Kobayashi, R.; Normand, J.; Raghavachari, K.; Rendell, A.; Burant, J. C.; Iyengar, S. S.; Tomasi, J.; Cossi, M.; Rega, N.; Millam, J. M.; Klene, M.; Knox, J. E.; Cross, J. B.; Bakken, V.; Adamo, C.; Jaramillo, J.; Gomperts, R.; Stratmann, R. E.; Yazyev, O.; Austin, A. J.; Cammi, R.; Pomelli, C.; Ochterski, J. W.; Martin, R. L.; Morokuma, K.; Zakrzewski, V. G.; Voth, G. A.; Salvador, P.; Dannenberg, J. J.; Dapprich, S.; Daniels, A. D.; Farkas, Ö.; Foresman, J. B.; Ortiz, J. V.; Cioslowski, J.; Fox, D. J. *Gaussian 09, Revision A.02*; Gaussian, Inc.: Wallingford, CT, 2009.
142. Borodin, O.; Smith, G. D.; Kim, H., *J. Phys. Chem. B* **2009,** *113* (14), 4771-4774.
143. Koh, C.; Liu, C.-L.; Harmon, C.; Strasser, D.; Golan, A.; Kostko, O.; Chambreau, S. D.; Vaghjiani, G. L.; Leone, S. R., *J. Phys. Chem. A* **2011,** *115* (18), 4630-4635.
144. Baer, T.; Song, Y.; Liu, J.; Chen, W.; Ng, C. Y., *Faraday Discuss.* **2000,** *115*, 137-145.
145. Locht, R.; Leyh, B.; Dahareng, D.; Hottmann, K.; Jochims, H. W.; Baumgartel, H., *Chem. Phys.* **2006,** *323*, 458-472.
146. Afeefy, H. Y.; Liebman, J. F.; Stein, S. E. Neutral Thermochemical Data. http://webbook.nist.gov (accessed March 15, 2011).
147. Lias, S. G. Ionization Energy Evaluation. http://webbook.nist.gov (accessed March 15, 2011).
148. Yamaoka, H.; Fokkens, R. H.; Nibbering, N. M. M., *Int. J. Mass. Spectrom.* **1999,** *188* (1-2), 1-6.

149. Arellano, I. H. J.; Guarino, J. G.; Paredes, F. U.; Arco, S. D., *J. Therm. Anal. Calorim.* **2011,** *103*, 725-730.
150. Fumino, K.; Wulf, A.; Verevkin, S. P.; Heintz, A.; Ludwig, R., *ChemPhysChem* **2010,** *11* (8), 1623-1626.
151. Bedrov, D.; Hooper, J. B., Molecular Dynamics Determination of DH_{vap} of Imidazolium Bromide Ionic Liquids. Wasach Molecuar, Inc.: private communication, 2011.
152. Kroll, J. H.; Smith, J. D.; Che, D. L.; Kessler, S. H.; Worsnop, D. R.; Wilson, K. R., *Phys. Chem. Chem. Phys.* **2009,** *11* (36), 8005-8014.
153. Schroder, C.; Steinhauser, O., *J. Chem. Phys.* **2008,** *128* (22), 7.
154. Hunt, P. A.; Gould, I. R.; Kirchner, B., *Aust. J. Chem.* **2007,** *60* (1), 9-14.
155. Vekey, K., *J. Mass Spectrom.* **1996,** *31* (5), 445-463.
156. Baer, T.; Johnston, M. V.; Nash, D. G., *Int. J. Mass Spectrom.* **2006,** *258* (1-3), 2-12.
157. DeCarlo, P. F.; Kimmel, J. R.; Trimborn, A.; Northway, M. J.; Jayne, J. T.; Aiken, A. C.; Gonin, M.; Fuhrer, K.; Horvath, T.; Docherty, K. S.; Worsnop, D. R.; Jimenez, J. L., *Anal. Chem.* **2006,** *78* (24), 8281-8289.
158. Farmer, D. K.; Matsunaga, A.; Docherty, K. S.; Surratt, J. D.; Seinfeld, J. H.; Ziemann, P. J.; Jimenez, J. L., *Proc. Natl. Acad. Sci. U. S. A.* **2010,** *107* (15), 6670-6675.
159. Nash, D. G.; Liu, X. F.; Mysak, E. R.; Baer, T., *Int. J. Mass Spectrom.* **2005,** *241* (2-3), 89-97.
160. Fredlake, C. P.; Crosthwaite, J. M.; Hert, D. G.; Aki, S. N. V. K.; Brennecke, J. F., *J. Chem. Eng. Data* **2004,** *49* (4), 954-964.
161. Leone, S. R.; Ahmed, M.; Wilson, K. R., *Phys. Chem. Chem. Phys.* **2010,** *12* (25), 6564-6578.
162. Smith, J. D.; Kroll, J. H.; Cappa, C. D.; Che, D. L.; Liu, C. L.; Ahmed, M.; Leone, S. R.; Worsnop, D. R.; Wilson, K. R., *Atmos. Chem. Phys.* **2009,** *9* (9), 3209-3222.
163. Litzinger, T.; Iyer, S., *Energy Fuels* **2011,** *25*, 72-76.
164. Chingin, K.; Perry, R. H.; Chambreau, S. D.; Vaghjiani, G. L.; Zare, R. N., *Angewandte Chemie-International Edition* **2011,** *50* (37), 8634-8637.
165. Taira, M.; Kanda, Y., *Anal. Chem.* **1993,** *65* (21), 3171-3173.
166. MacMillan, A. C.; McIntire, T. M.; Freites, J. A.; Tobias, D. J.; Nizkorodov, S. A., *J. Phys. Chem. B* **2012,** *116* (36), 11255-11265.